

MEASUREMENT OF THE MICHEL PARAMETER ρ IN MUON DECAY

A Dissertation

by

JAMES RAYMOND MUSSER

Submitted to the Office of Graduate Studies of
Texas A&M University
in partial fulfillment of the requirements for the degree of

DOCTOR OF PHILOSOPHY

December 2005

Major Subject: Physics

MEASUREMENT OF THE MICHEL PARAMETER ρ IN MUON DECAY

A Dissertation

by

JAMES RAYMOND MUSSER

Submitted to the Office of Graduate Studies of
Texas A&M University
in partial fulfillment of the requirements for the degree of

DOCTOR OF PHILOSOPHY

Approved by:

Chair of Committee,	Carl Gagliardi
Committee Members,	Che-Ming Ko
	Robert Tribble
	Sherry Yennello
Head of Department,	Edward Fry

December 2005

Major Subject: Physics

ABSTRACT

Measurement of the Michel Parameter ρ in Muon Decay. (December 2005)

James Raymond Musser, B.S., West Texas State University

Chair of Advisory Committee: Dr. Carl Gagliardi

The TWIST Collaboration has measured the Michel parameter ρ in normal muon decay, $\mu^+ \rightarrow e^+ \nu_e \bar{\nu}_\mu$. In the standard model of particle physics, $\rho = 3/4$. Deviations from this value require mixing of left- and right-handed muon and electron couplings in the muon-decay Lagrangian. We find $\rho = 0.75080 \pm 0.00032(\text{stat.}) \pm 0.00097(\text{syst.}) \pm 0.00023$, where the last uncertainty represents the dependence of ρ on the Michel parameter η . This result sets new limits on the $W_L - W_R$ mixing angle in left-right symmetric models.

ACKNOWLEDGMENTS

Many people have contributed to the success of this measurement and my development as a physicist. I thank the TWIST collaboration, the TRIUMF staff, the undergraduate co-op students assigned to TWIST, my dissertation committee and the physics faculty at Texas A&M University.

Special recognition is due to my advisor, Carl Gagliardi, who has shared both his expertise and his love of physics. In a similar spirit, I have benefited immensely from each of the TWIST leaders, Dave Gill, Nate Rodning and Glen Marshall.

I am especially grateful for my fellow graduate students, Ryan Bayes, Andrei Gaponenko, Blair Jamieson, Rob MacDonald and Farhana Sobratee, who exhibited the best of collaborative efforts, helping each one of us to understand and accomplish much more than we could have separately.

I thank my family for their support and patience. I thank Bob Musser, Donna Musser, Joe Musser and Clay Robinson for encouragement offered with understanding, based on their own experience as graduate students.

Most importantly, I recognize that my contribution to this work was only possible with the love and support of my wife and best friend, Kristen Musser.

Finally, I recognize all those who are committed to education, those who continually pursue a higher level of understanding for themselves and foster the growth of understanding in others. In particular, I recognize my father, Edgar Musser, and my colleague, the late Nate Rodning, as two whose embodiment of this spirit have been a continual source of inspiration to me.

*“It is the glory of God to conceal a matter;
to search out a matter is the glory of kings.”* (Solomon)

TABLE OF CONTENTS

CHAPTER		Page
I	INTRODUCTION: PHYSICS	1
	A. Standard Model	1
	1. Elementary Particles	1
	2. Quantum Chromodynamics	2
	3. Electro-weak Interaction	4
	B. General Description of Normal Muon Decay	6
	C. Non-standard Models	12
	1. Left-right Symmetric Models	12
	2. Non-local Tensor Interactions	15
	3. Massive ν 's	16
	D. Previous Muon Decay Parameter Measurements	17
	1. ρ Measurements	17
	2. $P_\mu\xi$ Measurement	18
	3. $P_\mu\xi\delta/\rho$ Measurement	20
	4. δ Measurement	20
	5. η Measurements	20
	E. TWIST Measurement	21
II	APPARATUS	22
	A. Overview	22
	B. Beam Line	22
	1. Production Target	22
	2. M13	24
	3. M13 Simulation	24
	4. Beam Measurement	26
	5. Beam Tunes	26
	C. Solenoid	31
	1. Field Measurements	31
	2. Field Simulation	31
	3. Field Map Scaling	33
	D. Detector	34
	1. Beam Package	34
	2. Stack	35

CHAPTER	Page
E. Slow Controls	39
F. Data Acquisition	40
1. Hardware	41
2. Software	41
III DATA	42
A. Data-taking Strategy	42
B. Data Sets	42
C. Systematic Sets	43
1. Beam Steering	45
2. Stopping Distribution	45
3. Outside Materials	45
4. Trigger Rate	45
5. High Voltage	45
D. Monte Carlo Verification Sets	46
1. Dense Stack Stops	46
2. Sparse Stack Stops	46
E. Calibration Sets	46
1. 120 MeV/c Pions	47
2. Efficiency Sets	47
3. Gas Degradar Tuning	47
IV ANALYSIS	49
A. Analysis strategy	49
1. Analysis Overview	49
2. Linear Expansion	49
3. Blind Analysis	51
B. Simulation	52
1. Chamber Response (GARFIELD)	52
2. Detector and Event (GEANT)	52
C. Monte Carlo Accuracy	54
1. Positron Energy Loss and Multiple Scattering	56
2. Muon Stopping Distribution	57
3. Event Type Rates	57
D. MOFIA	59
1. Unpacking	61
2. MOFIA Output	62
3. Time Separation	63

CHAPTER	Page
4. Particle Identification	65
5. Event Classification	65
6. Spatial Hit Clustering	75
7. Initial Track Estimate	75
8. Track Fitting	79
E. Root Tree Analysis	80
1. Event Cuts	81
2. Track Cuts	85
3. Track Selection	85
4. Algorithm A	86
5. Algorithm B	87
F. Momentum Calibration	87
V EVALUATION OF SYSTEMATIC UNCERTAINTIES	90
A. Uncertainties in Fits of Correlated Data	92
B. Track Selection Algorithm	92
C. Positron Interactions	92
1. Momentum Resolution	93
2. Multiple Scattering	93
3. Hard Interactions	93
4. Stopping Target Thickness	96
5. Material Outside Detector	96
D. Chamber Response	97
1. DC Efficiencies	97
2. MWPC Efficiencies	98
3. Dead Zone	98
4. Simulation of Drift Times Near Cell Boundaries	99
5. DC High Voltage Variations	99
6. Density Variations	101
7. Cathode Foil Bulges	101
8. Cross Talk	102
9. t_o Variations	102
E. Momentum Calibration	103
1. End Point Fits	103
2. Magnetic Field Reproduction	103
F. Muon Beam Stability	104
1. Stopping Location	104
2. Beam Intensity	105

CHAPTER	Page
3. Channel Magnets	105
G. Spectrometer Alignment	106
1. Translational	106
2. Rotational	106
3. Longitudinal	106
4. Magnetic Field Relative to Axis	107
H. Theoretical Radiative Corrections	107
I. Summary of Systematic Uncertainties	107
VI EXTRACTION OF MICHEL PARAMETERS	109
A. Fiducials	109
1. $ \cos \theta > 0.5$	109
2. $ \cos \theta < 0.84$	109
3. $ \vec{p} < 50 \text{ MeV}/c$	113
4. $p_{\perp} < 38.5 \text{ MeV}/c$	113
5. $ p_z > 13.7 \text{ MeV}/c$	113
6. Sensitivity to Fiducial Cuts	113
B. Quality of Analysis Results	115
1. Michel Parameter Fits	115
2. Fit Residuals	115
C. $d\rho/d\eta$	119
D. Single Fit Parameter Fits of Angle Integrated Spectra . . .	122
E. ρ	122
F. Other Michel Parameters	124
1. Distortion of the Asymmetry	124
2. δ	125
VII CONCLUSIONS	127
A. $P_{\mu\xi}$	127
B. Implications for Left-right Symmetric Models	127
C. Future Measurements	129
D. Summary	129
REFERENCES	130
VITA	133

LIST OF TABLES

TABLE		Page
I	Comparison of the four fundamental forces	2
II	Standard model particles by families	3
III	Electro-weak quantum numbers.	4
IV	Coupling constant limits	7
V	Limits derived from ν mass limits	16
VI	Previous measurements of ρ	18
VII	Measurements of Michel parameters other than ρ	19
VIII	M13 slit settings	25
IX	Slow control variables	40
X	Data sets	43
XI	Systematic sets	44
XII	Time window classifications.	67
XIII	Systematic uncertainties due to foil bulging.	102
XIV	Systematic uncertainties due to magnetic field simulation.	104
XV	Systematic uncertainties summary	108
XVI	Correlation coefficients for 3 and 4 parameter fits	120
XVII	Correlation coefficients for 1 and 2 parameter fits	121
XVIII	$d\rho/d\eta$	123
XIX	ρ by data set	124

TABLE		Page
XX	$P_\mu \xi$ by data set	125
XXI	δ by data set	126

LIST OF FIGURES

FIGURE		Page
1	Michel spectrum as function of momentum and $\cos \theta$	8
2	Michel distribution as a function of momentum.	9
3	Michel spectrum dependence on ρ and η	10
4	Michel asymmetry dependence on δ	11
5	Left-right symmetric model exclusion plot	14
6	Conceptual view of TWIST detector.	23
7	Schematic of M13 beamline	25
8	Beam measurement apparatus	27
9	Beam characterization for Post-Oct23 surface muon beam	28
10	Beam characterization for Pre-Oct23 surface muon beam	29
11	Beam characterization for cloud muon beam	30
12	Measured longitudinal magnetic field	32
13	Scaled field accuracy	33
14	Beam package.	34
15	Side view of TWIST detector	36
16	End view of drift chamber.	37
17	DC efficiency as a function of high voltage	48
18	Isochrones for drift chamber cell	53
19	Beam spot	55

FIGURE		Page
20	Momentum loss in detector	57
21	Momentum loss times $\cos \theta$ vs. momentum	58
22	Scattering in detector	59
23	Muon longitudinal stopping position	60
24	Event classification rates, Monte Carlo vs. data.	61
25	Event display of upstream decay	64
26	Time window schematic	66
27	Downstream decay plus delta	70
28	Upstream fast decay	71
29	Upstream decay	72
30	Downstream decay	73
31	Muon lifetime	74
32	Hit clusters	76
33	Reconstruction efficiency	80
34	Algorithm A event cuts	82
35	Algorithm B event cuts	83
36	Momentum endpoint spectra	89
37	Ratios of momentum histograms	95
38	Number of degrees of freedom vs. drift time cut (ns) for data	100
39	Fiducial cuts	110
40	Yield for fiducial cuts within $0.7 < \cos \theta < 0.84$	111
41	Yield for fiducial cuts within $0.5 < \cos \theta < 0.7$	112

FIGURE	Page
42	Detector-track wavelength match 114
43	Michel parameter fit sensitivity to fiducial cuts 116
44	Michel parameter fit residuals vs. momentum 117
45	Michel parameter fit residuals vs. $\cos \theta$ 118
46	Reconstruction probability and normalized residuals 119
47	Updated left-right symmetric model exclusion plot 128

CHAPTER I

INTRODUCTION: PHYSICS

A. Standard Model

There are four known forces by which elementary particles interact: the strong nuclear force, the electro-magnetic force, the weak nuclear force and the gravitational force. Relative characteristics of the interactions are shown in Table I. It is a goal of particle physicists to develop a model that unifies these forces and the elementary particles into a single coherent description of nature. The Glashow-Weinberg-Salam, or GWS, model and the standard model of particle physics represent two steps towards the goal of a unified theory. The GWS model unifies the electro-magnetic and weak nuclear forces while the standard model combines the GWS model with a description of the strong nuclear force.

1. Elementary Particles

The standard model constituents are point-like “elementary particles” including quarks and leptons and the particles that mediate interactions. The particles include the up (u) and down (d) quarks and the leptons, the electron (e^-) and the electron neutrino (ν_e). Each particle is described by a set of quantum numbers that are derived from characteristics of the particles’ interactions. The up and down quarks carry a baryon number of $1/3$ and a lepton number of 0 . The electron and neutrino carry a baryon number of 0 and a lepton number of 1 . In addition, the up(down) quark carries an electric charge of $+2/3(-1/3)$ while the electron(neutrino) carries an electric charge

The journal model is *Physical Review D: Particles, Fields, Gravitation, and Cosmology*.

Table I. Comparison of the four fundamental forces. [1]

Interaction	Mediator	Relative	Typical	Range
		Strength (α_s)	Lifetime (s)	
Strong Nuclear	g_i (gluons)	1	10^{-23}	1 fm
Electromagnetic	γ (photon)	10^{-2}	$10^{-20} \sim 10^{-16}$	∞
Weak Nuclear	W^+ , W^- and Z^0	10^{-6}	$\geq 10^{-12}$	10^{-3} fm
Gravitational	Graviton	10^{-40}		∞

of $-1(0)$. All four of the particles have intrinsic spin of $\hbar/2$. These four particles are collectively referred to as a family. Second and third families also exist, which differ from the first family only in the mass of the particles, such that second family particles are heavier than their corresponding first family particles (with the exception of the neutrinos, whose masses are unknown). Likewise, particles from the third family are heavier than corresponding second family particles. Furthermore, for each of the particles described above, there exists a spin $\hbar/2$ particle of identical mass but opposite baryon number, lepton number and electric charge. These are designated anti-particles and are denoted with a “bar” (ie. \bar{u} and \bar{e}). Standard model particle families are illustrated in Table II.

2. Quantum Chromodynamics

The standard model description of the strong nuclear force is based on the gauge group $SU(3)_C$. In the model, quarks carry a color charge, R (red), G (green) or B

Table II. Standard model particles by families. The pattern also holds for the anti-particles.

Generation		
1 st	2 nd	3 rd
Quarks		
u (up)	c (charm)	t (top)
d (down)	s (strange)	b (bottom)
Leptons		
e^- (electron)	μ^- (muon)	τ^- (tau)
ν_e (electron neutrino)	ν_μ (muon neutrino)	ν_τ (tau neutrino)

(blue) such that quarks and anti-quarks are represented as

$$\begin{pmatrix} u_{\text{R}} \\ u_{\text{G}} \\ u_{\text{B}} \end{pmatrix}, \quad \begin{pmatrix} \bar{u}_{\text{R}} \\ \bar{u}_{\text{G}} \\ \bar{u}_{\text{B}} \end{pmatrix}, \quad \begin{pmatrix} d_{\text{R}} \\ d_{\text{G}} \\ d_{\text{B}} \end{pmatrix}, \quad \begin{pmatrix} \bar{d}_{\text{R}} \\ \bar{d}_{\text{G}} \\ \bar{d}_{\text{B}} \end{pmatrix}, \dots$$

This description of the strong nuclear force in terms of color is referred to as “Quantum Chromodynamics” (QCD). In addition to the particles delineated above there are gauge bosons of spin $1\hbar$ called gluons, denoted g_i , that mediate the strong nuclear interactions. The gluons carry a combination of color and anti-color and only interact with colored particles, i.e. quarks and other gluons. There are eight varieties of gluons corresponding to the eight possible combinations that carry color: $\text{R}\bar{\text{G}}$, $\text{R}\bar{\text{B}}$, $\text{G}\bar{\text{R}}$, $\text{G}\bar{\text{B}}$, $\text{B}\bar{\text{R}}$, $\text{B}\bar{\text{G}}$, $\sqrt{1/2}(\text{R}\bar{\text{R}} - \text{G}\bar{\text{G}})$, $\sqrt{1/6}(\text{R}\bar{\text{R}} + \text{G}\bar{\text{G}} - 2\text{B}\bar{\text{B}})$. [1] (A ninth possible combination, $\sqrt{1/3}(\text{R}\bar{\text{R}} + \text{G}\bar{\text{G}} + \text{B}\bar{\text{B}})$, carries no color and cannot mediate an interaction between color charges.) Note that the leptons do not carry color and thus do not participate

Table III. Electro-weak quantum numbers.

Quark	T	T^3	Y	$q (T^3 + \frac{Y}{2})$	Lepton	T	T^3	Y	$q (T^3 + \frac{Y}{2})$
u_L	$\frac{1}{2}$	$\frac{1}{2}$	$\frac{1}{3}$	$\frac{2}{3}$	ν_e	$\frac{1}{2}$	$\frac{1}{2}$	-1	0
d_L	$\frac{1}{2}$	$-\frac{1}{2}$	$\frac{1}{3}$	$-\frac{1}{3}$	e_L^-	$\frac{1}{2}$	$-\frac{1}{2}$	-1	-1
u_R	0	0	$\frac{4}{3}$	$\frac{2}{3}$	e_R^-	0	0	-2	-1
d_R	0	0	$-\frac{2}{3}$	$-\frac{1}{3}$					

in strong nuclear interactions.

3. Electro-weak Interaction

The GWS model description of the electro-weak interaction, and hence the standard model's, is based on the gauge group $SU(2)_L \times U(1)_Y$. In the GWS model left-handed particles (right-handed antiparticles) transform as doublets under $SU(2)$ while right-handed particles (left-handed antiparticles) are singlets.

$$\begin{pmatrix} u \\ d \end{pmatrix}_L, \quad \begin{pmatrix} \nu_e \\ e^- \end{pmatrix}_L, \quad u_R, \quad d_R, \quad e_R^- \quad (1.1)$$

The explicit left-right asymmetry is introduced to account for observed parity violation. The group $SU(2)_L$ is generated by the weak isospin generators, $T^i = \int \bar{\chi}_L \gamma_0 (\tau_i / 2) \chi_L d^3x$, $i = 1, 2, 3$, where χ_L is the doublet and the τ_i are the Pauli spin matrices. $U(1)_Y$ is generated by the weak hypercharge operator, Y , defined such that $q = T^3 + Y/2$, where q is the observed electromagnetic charge. Electro-weak quantum numbers for the elementary particles are shown in Table III. The electro-weak interaction is

$$-ig\bar{\chi}_L \gamma^\mu \frac{\tau_i}{2} W_\mu^i \chi_L - i\frac{g'}{2} \bar{\psi} \gamma^\mu Y B_\mu \psi$$

The vector fields can be related to the physically observed mass eigenstates, W^\pm (charged weak bosons), Z^0 (neutral weak boson) and A (photon) via

$$\begin{aligned} W_\mu^\pm &= \sqrt{\frac{1}{2}}(W_\mu^1 \mp iW_\mu^2) \\ Z_\mu^0 &= \cos\theta_W W_\mu^3 - \sin\theta_W B_\mu \\ A_\mu &= \sin\theta_W W_\mu^3 + \cos\theta_W B_\mu, \end{aligned} \tag{1.2}$$

where θ_W is the experimentally determined Weinberg angle ($\sin\theta_W \approx 0.23$) [2]. Furthermore, the couplings g and g' can be expressed in terms of the electromagnetic coupling, e , and the Weinberg angle,

$$g = \frac{e}{\sin\theta_W} \quad \text{and} \quad g' = \frac{e}{\cos\theta_W} \tag{1.3}$$

Note that in the GWS model the charged weak bosons couple only to left-handed particles (right-handed antiparticles). Left- and right-handed particles are obtained by applying the appropriate projection operator:

$$\psi_L = \frac{1}{2}(1 - \gamma^5)\psi \quad \psi_R = \frac{1}{2}(1 + \gamma^5)\psi \tag{1.4}$$

Thus the charge changing weak interaction contains equal contributions of vector, γ^μ , and axial-vector terms, $\gamma^\mu\gamma^5$, and is therefore considered a pure V-A interaction.

In Eq. (1.1) the particles were labeled as if the weak eigenstates were the mass eigenstates. In general, the weak and mass eigenstates could be related by a rotation matrix so the mass eigenstates d , s and b in Eq. (1.1) should be replaced by the weak eigenstates d' , s' and b' , respectively. The rotation matrix for the quarks is known as

the Cabibbo-Kobayashi-Maskawa (CKM) matrix;

$$\begin{pmatrix} d' \\ s' \\ b' \end{pmatrix} = \begin{pmatrix} V_{ud} & V_{us} & V_{ub} \\ V_{cd} & V_{cs} & V_{cb} \\ V_{td} & V_{ts} & V_{tb} \end{pmatrix} \begin{pmatrix} d \\ s \\ b \end{pmatrix}. \quad (1.5)$$

The first two diagonal elements are $|V_{ud}| = 0.9738 \pm 0.0005$ and $|V_{cs}| = 0.996 \pm 0.013$ and the 90% confidence interval for the third, $|V_{tb}|$, is $(0.9990, 0.9992)$ [2]. The comparable matrix for the leptons is not yet well determined and is the subject of much study in the particle physics community. Recent results show that, unlike the CKM matrix, the neutrino mixing matrix is far from diagonal. For a detailed summary of neutrino mixing see [3].

B. General Description of Normal Muon Decay

The “weakness” of the weak interaction relative to the strong and electromagnetic interactions (see Table I) implies that the weak force is not generally observed. The weak interaction is best studied in systems that cannot interact or decay via the stronger forces. Normal muon decay, $\mu^+ \rightarrow e^+ \nu_e \bar{\nu}_\mu$, is such an interaction. As a purely leptonic process it is not subject to strong nuclear interactions. Consider a general description of the weak interaction using muon decay as the example. The most general local, derivative-free interaction describing muon decay can be expressed in terms of the matrix element [4, 5]

$$M = 4 \frac{G_F}{\sqrt{2}} \sum_{\substack{\gamma=S,V,T \\ \epsilon,\mu=R,L}} g_{\epsilon\mu}^\gamma \langle \bar{e}_\epsilon | \Gamma^\gamma | \nu_e \rangle \langle \bar{\nu}_\mu | \Gamma_\gamma | \mu_\mu \rangle. \quad (1.6)$$

G_F is the Fermi coupling constant; γ is the type of interaction ($\Gamma^S \equiv$ scalar, $\Gamma^V \equiv$ vector, $\Gamma^T \equiv$ tensor) and ϵ and μ indicate the chirality of the positron (ϵ) and muon

Table IV. Coupling constant limits. [2]

$ g_{RR}^S < 0.066$	$ g_{RR}^V < 0.033$	$ g_{RR}^T \equiv 0$
$ g_{RL}^S < 0.424$	$ g_{RL}^V < 0.110$	$ g_{RL}^T < 0.122$
$ g_{LR}^S < 0.125$	$ g_{LR}^V < 0.060$	$ g_{LR}^T < 0.036$
$ g_{LL}^S < 0.550$	$ g_{LL}^V > 0.960$	$ g_{LL}^T \equiv 0$

(μ). In this description G_F contains the strength of the interaction while the coupling constants, $g_{e\mu}^\gamma$, characterize the form of the interaction. There are ten such complex coupling constants related by an overall normalization

$$\begin{aligned} \frac{1}{4} & \left[|g_{RR}^S|^2 + |g_{RL}^S|^2 + |g_{LR}^S|^2 + |g_{LL}^S|^2 \right] \\ & + |g_{RR}^V|^2 + |g_{RL}^V|^2 + |g_{LR}^V|^2 + |g_{LL}^V|^2 \\ & + 3 \left[|g_{RL}^T|^2 + |g_{LR}^T|^2 \right] = 1 \end{aligned} \quad (1.7)$$

and a common phase, yielding eighteen independent parameters from the coupling constants.

This formulation neglects the non-local corrections to the standard model Lagrangian that arise due to the finite W -boson mass. These terms are $O(m_\mu^2/m_W^2) \sim 10^{-6}$ and, thus are small compared to the effects studied here.

In the standard model $g_{LL}^V \equiv 1$ and all other coupling constants are zero. The standard model muon decay spectrum is shown in Fig. 1 as a function of momentum and $\cos \theta$, where θ is the angle between the polarization of the muon and the momentum of the decay positron ($\cos \theta = \vec{P}_\mu \cdot \vec{p}_e / \left[\left| \vec{P}_\mu \right| \cdot \left| \vec{p}_e \right| \right]$). Current ninety-percent confidence level limits for the coupling constants are shown in Table IV.

It is convenient for experimental measurements to describe muon decay in terms

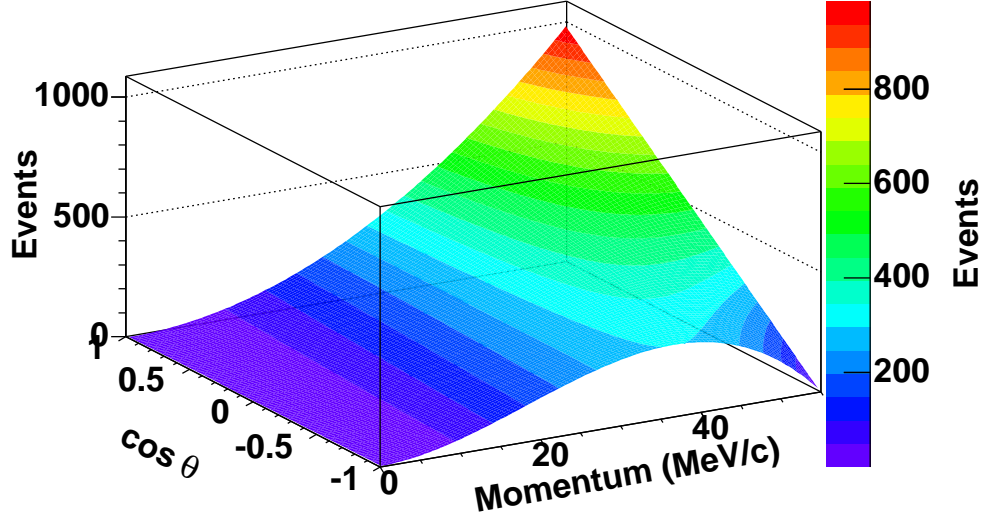


Fig. 1. Michel spectrum as function of momentum and $\cos \theta$.
 $\cos \theta = \vec{P}_\mu \cdot \vec{p}_e / \left[\left| \vec{P}_\mu \right| \cdot \left| \vec{p}_e \right| \right]$.

of bilinear combinations of the coupling constants commonly referred to as the Michel parameters [6, 7, 8, 9]. In this parameterization, the decay spectrum can be written as

$$\frac{d^2\Gamma}{dx d\cos\theta} = \frac{m_\mu}{4\pi^3} W_{e\mu}^4 G_F^2 \sqrt{x^2 - x_o^2} \times [F_{IS}(x, \rho, \eta) + \cos\theta P_\mu F_{AS}(x, \delta, \xi)] \quad (1.8)$$

Where $W_{e\mu} \equiv (m_\mu^2 + m_e^2) / 2m_\mu$, the maximum positron energy; $x_o \equiv m_e / W_{e\mu}$, the minimum positron energy; $x = E_e / W_{e\mu}$, the reduced energy; θ is the angle between the polarization of the muon and the direction of the decay positron; P_μ is the polarization of the muon and ρ, η, ξ and δ are the Michel parameters. The Michel momentum spectrum is shown in Fig. 2. Ignoring radiative corrections the isotropic term is

$$F_{IS} = x(1-x) + \frac{2}{9}\rho(4x^2 - 3x - x_o^2) + \eta x_o(1-x) \quad (1.9)$$

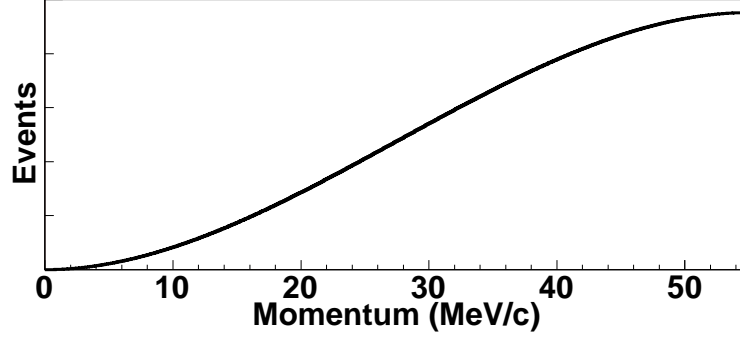


Fig. 2. Michel distribution as a function of momentum.

and the anisotropic term is

$$P_\mu F_{AS} = \frac{1}{3} \sqrt{x^2 - x_o^2} \left[P_\mu \xi (1 - x) + \frac{2}{3} P_\mu \xi \delta (4x - 4 + \sqrt{1 - x_o^2}) \right]. \quad (1.10)$$

Radiative corrections are discussed in detail in [10, 11, 12, 13].

The Michel parameters expressed in terms of coupling constants are [14]

$$\begin{aligned} \rho &= \frac{3}{4} - \frac{3}{4} [|g_{RL}^V|^2 + |g_{LR}^V|^2 + 2 |g_{RL}^T|^2 + 2 |g_{LR}^T|^2 \\ &\quad + \text{Re} (g_{RL}^S g_{RL}^{T*} + g_{LR}^S g_{LR}^{T*})] \\ \eta &= \frac{1}{2} \text{Re} [g_{RR}^V g_{LL}^{S*} + g_{LL}^V g_{RR}^{S*} + g_{RL}^V (g_{LR}^{S*} + 6g_{LR}^{T*}) + g_{LR}^V (g_{RL}^{S*} + 6g_{RL}^{T*})] \\ \xi &= 1 - \frac{1}{2} |g_{LR}^S|^2 - \frac{1}{2} |g_{RR}^S|^2 - 4 |g_{RL}^V|^2 + 2 |g_{LR}^V|^2 - 2 |g_{RR}^V|^2 \\ &\quad + 2 |g_{LR}^T|^2 - 8 |g_{RL}^T|^2 + 4 \text{Re} (g_{LR}^S g_{LR}^{T*} - g_{RL}^S g_{RL}^{T*}) \\ \xi \delta &= \frac{3}{4} - \frac{3}{8} |g_{RR}^S|^2 - \frac{3}{8} |g_{LR}^S|^2 - \frac{3}{2} |g_{RR}^V|^2 - \frac{3}{4} |g_{RL}^V|^2 - \frac{3}{4} |g_{LR}^V|^2 \\ &\quad - \frac{3}{2} |g_{RL}^T|^2 - 3 |g_{LR}^T|^2 + \frac{3}{4} \text{Re} (g_{LR}^S g_{LR}^{T*} - g_{RL}^S g_{RL}^{T*}) \end{aligned} \quad (1.11)$$

It is straightforward to show that in the standard model $\rho = 3/4$, $\eta = 0$, $\xi = 1$ and $\xi \delta = 3/4$.

Several extensions to the standard model predict differences in the parameters which would distort the Michel spectrum. Spectrum shape differences due to non-

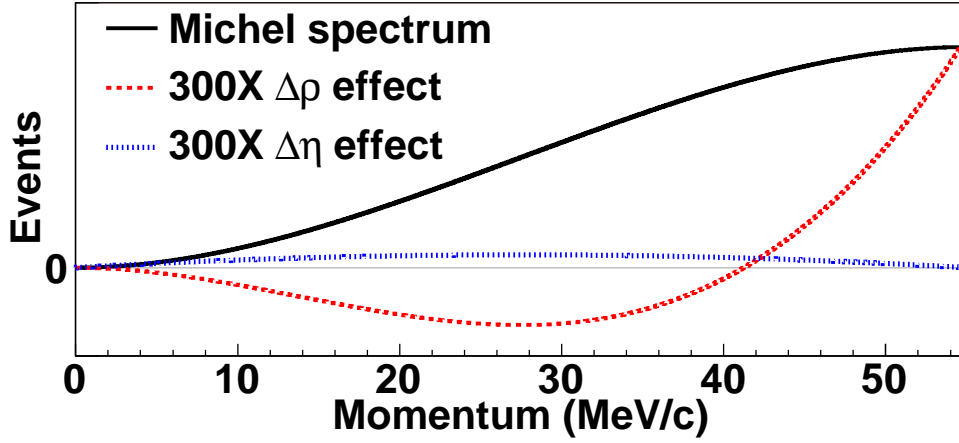


Fig. 3. Michel spectrum dependence on ρ and η . Effects shown for differences in ρ and η at the world limits ($\Delta\rho = 0.0026$ and $\Delta\eta = 0.013$).

standard model values of ρ and η are illustrated in Fig. 3. Differences in the momentum dependence of the asymmetry due to a non-standard model value of δ are illustrated in Fig. 4.

Another convenient combination of coupling constants is a parameterization by Fetscher *et al.* [4]:

$$\begin{aligned}
 Q_{RR} &\equiv \frac{1}{4} |g_{RR}^S|^2 + |g_{RR}^V|^2 \\
 Q_{LR} &\equiv \frac{1}{4} |g_{LR}^S|^2 + |g_{LR}^V|^2 + 3 |g_{LR}^T|^2 \\
 Q_{RL} &\equiv \frac{1}{4} |g_{RL}^S|^2 + |g_{RL}^V|^2 + 3 |g_{RL}^T|^2 \\
 Q_{LL} &\equiv \frac{1}{4} |g_{LL}^S|^2 + |g_{LL}^V|^2 \\
 B_{LR} &\equiv \frac{1}{16} |g_{LR}^S + 6g_{LR}^T|^2 + |g_{LR}^V|^2 \\
 B_{RL} &\equiv \frac{1}{16} |g_{RL}^S + 6g_{RL}^T|^2 + |g_{RL}^V|^2 \\
 I_\alpha &\equiv \frac{1}{4} g_{LR}^V (g_{RL}^S + 6g_{RL}^T)^* + \frac{1}{4} g_{RL}^{V*} (g_{LR}^S + 6g_{LR}^T) \\
 I_\beta &\equiv \frac{1}{2} g_{LL}^V g_{RR}^{S*} + \frac{1}{2} g_{RR}^{V*} g_{LL}^S
 \end{aligned} \tag{1.12}$$

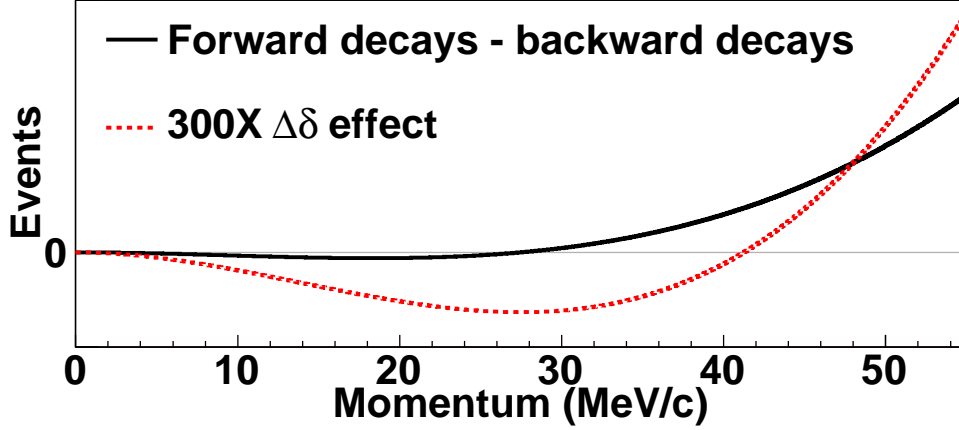


Fig. 4. Michel asymmetry dependence on δ . Effect shown is for a difference in δ at the world limit ($\Delta\delta = 0.0038$).

The authors [4] point out that the advantage of these equations is “... that they contain the maximum possible number of positive semidefinite quadratic forms of the coupling constants, which are determined (as linear combinations) by the observables.” $Q_{\epsilon\mu}$ is interpreted as the relative probability of a μ -handed muon decaying into an ϵ -handed electron. The $Q_{\epsilon\mu}$ obey $0 \leq Q_{\epsilon\mu} \leq 1$ and $\sum Q_{\epsilon\mu} = 1$ as expected by probabilities. In addition, the $B_{\epsilon\mu}$ obey $0 \leq B_{\epsilon\mu} \leq Q_{\epsilon\mu}$, $|I_\alpha|^2 \leq B_{LR}B_{RL}$, and $|I_\beta|^2 \leq Q_{LL}Q_{RR}$.

In this parameterization, the probability of a right-handed muon decaying into either a left- or right-handed electron, Q_R^μ , can be simply expressed in terms of Michel parameters,

$$Q_R^\mu \equiv Q_{LR} + Q_{RR} = \frac{1}{2} \left[1 + \frac{1}{3}\xi - \frac{16}{9}\xi\delta \right]. \quad (1.13)$$

Thus measuring the Michel parameters, ξ and δ , leads to simultaneous limits on the coupling constants, g_{RR}^S , g_{RR}^V , g_{LR}^S , g_{LR}^V and g_{LR}^T .

In a similar fashion a measurement of ρ , ξ and δ leads to limits on g_{RR}^S and g_{RR}^V

via the combination,

$$\rho - \xi\delta = \frac{3}{8} |g_{RR}^S|^2 + \frac{3}{2} |g_{RR}^V|^2 + \frac{3}{8} |g_{LR}^S - 2g_{LR}^T|^2. \quad (1.14)$$

C. Non-standard Models

The standard model is extremely successful, explaining previously observed phenomena, predicting subsequently observed particles and offering a unified theory of three of the four fundamental forces. However, it falls short of providing answers to some basic questions:

- Why are there multiple families of particles?
- Why is there a left-right asymmetry in the weak interaction?
- What produces the significant mass differences between the elementary particles?
- How is gravity related to the other fundamental interactions?

In an attempt to answer these questions, many physicists are considering extensions to the standard model.

1. Left-right Symmetric Models

One class of standard model extensions is referred to as “Left-right Symmetric Models” [15, 16]. Left-right symmetric models are based on the gauge group $SU(2)_L \times SU(2)_R \times U(1)_Y$. In these models the right-handed fermions transform as doublets in the same manner as the left-handed fermions.

$$\begin{pmatrix} u \\ d' \end{pmatrix}_L, \quad \begin{pmatrix} \nu_e' \\ e^- \end{pmatrix}_L, \quad \begin{pmatrix} u \\ d'' \end{pmatrix}_R, \quad \begin{pmatrix} \nu_e'' \\ e^- \end{pmatrix}_R$$

Double primes have been used in labeling right-handed particles because the left- and right-handed mixing matrices are independent of each other and are likely to differ from one another. Additionally, there exists another set of gauge bosons, W_R^\pm and Z_R^o , that couple to the right-handed particles. In left-right symmetric models the W_L and W_R are linear combinations of the mass eigenstates, W_1 and W_2 .

$$W_L = W_1 \cos \zeta - W_2 \sin \zeta \quad (1.15)$$

$$W_R = e^{i\omega} W_1 \sin \zeta + e^{i\omega} W_2 \cos \zeta \quad (1.16)$$

In these theories parity is a symmetry that is spontaneously broken at low energies. Left-right models are characterized by the mass-squared ratio, $\epsilon = M_{W_1}^2/M_{W_2}^2$, the mixing angle, ζ , and a CP violating phase, ω . The ζ and ϵ of the left-right symmetric models can be expressed in terms of the Michel parameters ρ and ξ as

$$\zeta = \sqrt{\frac{1}{2} - \frac{2}{3}\rho} \quad (1.17)$$

$$\epsilon = \sqrt{\frac{2}{3}\rho - \frac{1}{2}\xi} \quad (1.18)$$

Figure 5 shows 90% confidence limits for ζ and the mass of W_R . Two curves are derived from $P_\mu \xi \delta / \rho$ and the relations;

$$\zeta = \pm \sqrt{\frac{1}{2}(1 - P_\mu \xi \delta / \rho) - \epsilon^2} \quad [\text{small } V_{ud}^R] \quad (1.19)$$

and

$$\zeta = -\epsilon \pm \sqrt{\frac{1}{2}(1 - P_\mu \xi \delta / \rho) - \epsilon^2} \quad [V_{ud}^R \sim V_{ud}^L]. \quad (1.20)$$

Additional limits on ϵ and ζ are derived from collider experiments [17, 18] and nuclear beta decay [19], respectively. For a more complete discussion of left-right symmetric models and their implications for muon decay see [20, 21].

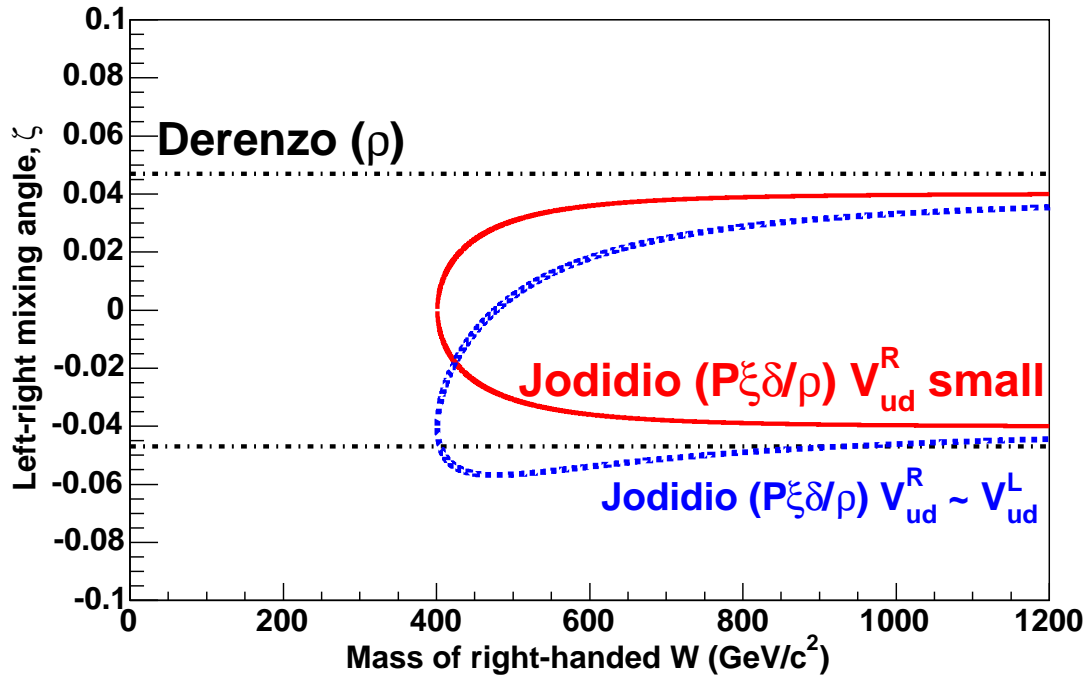


Fig. 5. Left-right symmetric model exclusion plot. Limits from muon decay on ζ and M_{W_R} of left-right symmetric models. All limits shown are for 90% confidence levels. Derenzo's fit [32] and Jodidio's measurement [40] are described in Sec. D. The two curves derived from $P_\mu \xi \delta / \rho$ come from different assumptions about V_{ud}^R as labeled.

2. Non-local Tensor Interactions

Chizhov has proposed a non-local tensor component of the weak interaction where $g_{RR}^T \neq 0$ and $g_{LL}^T \neq 0$ [22]. A non-zero value of g_{RR}^T signals an interaction involving left-handed ν 's. Such an interaction could interfere with standard model normal muon decay. This interaction introduces a term in the muon decay Lagrangian of

$$\mathcal{L}_T = -g_{RR}^T \sqrt{2} G_F (\bar{\mu}_R \sigma_{\alpha\lambda} \nu) \frac{4q_\alpha q_\beta}{q^2} (\bar{\nu}_e \sigma_{\beta\lambda} e_R) + h.c. \quad (1.21)$$

The resulting decay spectrum is described by including additional terms in F_{IS} (Eq. (1.9)) and $P_\mu F_{AS}$ (Eq. (1.10)) ,

$$F_{IS} = x(1-x) + \frac{2}{9}\rho(4x^2 - 3x - x_o^2) + \eta x_o(1-x) + \kappa x_o \quad (1.22)$$

and

$$P_\mu F_{AS} = \frac{1}{3} \sqrt{x^2 - x_o^2} \left[P_\mu \xi(1-x) + \frac{2}{3} P_\mu \xi \delta(4x - 4 + \sqrt{1-x_o^2}) \right] + P_\mu \kappa x_o(2-x), \quad (1.23)$$

where

$$\kappa = \frac{g_{RR}^T}{1 + 3|g_{RR}^T|^2} \quad (1.24)$$

represents a new muon decay parameter. The contribution to the Michel parameters due to the non-local tensor interaction is given by

$$\Delta\rho_\kappa \approx -\frac{3}{2}\kappa^2; \quad (1.25)$$

$$\Delta\xi_\kappa \approx 2\kappa^2; \quad (1.26)$$

$$\Delta\delta_\kappa \approx -\frac{9}{2}\kappa^2. \quad (1.27)$$

Chizhov derives a value for this interaction, $g_{RR}^T \approx 0.013$ [23], based on results from the PIBETA experiment [24].

Table V. Limits derived from ν mass limits. [28]

Coupling constant	Order of magnitude upper limit
g_{RL}^S	10^{-2}
g_{LR}^S	10^{-4}
g_{RL}^V	10^{-2}
g_{LR}^V	10^{-4}
g_{RL}^T	10^{-2}
g_{LR}^T	10^{-4}
Michel parameter	Order of magnitude upper limit
$\rho - \frac{3}{4}$	10^{-3}
$\delta - \frac{3}{4}$	10^{-2}

3. Massive ν 's

The original formulation of the standard model treated ν 's as massless particles. Observations at Super-Kamiokande [25] and SNO [26, 27] give convincing evidence that ν 's are massive particles. To date, attempts to determine the mass of the ν 's have yielded only mass differences between varieties and upper limits. Recent theoretical work by Pr ezeau *et al.* proposes that non-standard model interactions would contribute to ν mass [28]. Leading logarithmic contributions have been calculated and combined with current ν mass limits to derive order of magnitude limits on some of the Michel parameters and the associated coupling constants. Limits are shown in Table V.

D. Previous Muon Decay Parameter Measurements

1. ρ Measurements

The world average for ρ comes from a series of measurements made in the 1960's of the positron momentum spectrum from unpolarized muon decay. Peoples in '66, Sherwood in '67, Fryberger in '68 and Derenzo in '69 made fits to ρ while constraining $\eta = 0$ [29, 30, 31, 32]. In 1969, Derenzo utilized data from all three measurements in a two parameter fit to ρ and η [32]. Results are shown in Table VI.

Derenzo's result is dominated by Peoples' data. The Peoples measurement was performed at the Columbia University Nevis synchrocyclotron. Pions from the synchrocyclotron were stopped in a scintillator that served as both stopping target and trigger. Muons from the pion decays that stopped within the scintillator subsequently decayed yielding Michel positrons. The positrons were tracked using a set of four sonic spark chambers in a homogeneous magnetic field.

The Sherwood measurement at the University of Chicago used a spectrometer similar to Peoples' in concept but utilizing digitized spark chambers instead of sonic spark chambers. Two measurements of ρ were made by fitting the momentum spectrum within the reduced energy ranges, $0.52 \leq x \leq 0.76$ and $0.70 \leq x \leq 0.92$, respectively. In addition, Sherwood discussed the $\rho - \eta$ correlation and observed, "An experiment in which the *entire* spectrum ($0 \leq x \leq 1$) is determined is statistically far more advantageous; then the $\rho - \eta$ correlation is much reduced, because the difference in the ρ - and η -associated functional forms emerge clearly." ([30], p. 1477)

Fryberger modified the spectrometer used by Sherwood for his measurement. Significant changes were made to the detector entrance and trigger. The trigger scintillator was replaced by a "stops telescope". The stops telescope consisted of a

Table VI. Previous measurements of ρ . *Derenzo's two parameter fit is the world average including data from Peoples, Sherwood and Fryberger.

Reference	Year	ρ value	Comment
Peoples[29]	1966	0.7503 ± 0.0026	constrained $\eta \equiv 0$
Sherwood[30]	1967	0.760 ± 0.009	constrained $\eta \equiv 0$
Fryberger[31]	1968	0.762 ± 0.008	constrained $\eta \equiv 0$
Derenzo*[32]	1969	0.7518 ± 0.0026	two parameter fit to ρ and η

pair of scintillators before and after a stopping target. Both lithium and graphite stopping targets were used.

Derenzo measured the momentum spectrum below 6.8 MeV/c in an effort focused on determining η . A subset of the data was analyzed for ρ within the reduced energy range, $0.05 \leq x \leq 0.90$. The measurement was performed using the 10-liter University of Chicago hydrogen bubble chamber. Pions and muons from the Chicago synchrocyclotron stopped in the chamber. The pions decayed to muons and the muon decay produced Michel positrons. 4240 frames of ~ 5 muon decays each were analyzed for the ρ measurement.

Two additional experiments, MEGA and the Los Alamos TPC measurement, have attempted to measure ρ but have not improved upon the world average [33, 34].

Measurements for other Michel parameters are shown in Table VII.

2. $P_\mu\xi$ Measurement

The Michel distribution, ignoring radiative corrections, is a function of the combination $P_\mu\xi$ rather than ξ , independently, as seen in Eq. 1.10. Thus, experiments generally measure $P_\mu\xi$ and it is this combination that is reported by the Particle

Table VII. Measurements of Michel parameters other than ρ . Particle Data Group value for η includes data from Burkard and Derenzo.

Parameter	Reference	Year	Value
η	Burkard[35]	1985	-0.007 ± 0.013
η	Derenzo[32]	1969	-0.12 ± 0.21
η	Danneburg[36]	2005	$0.071 \pm 0.037(\text{stat}) \pm 0.005(\text{syst})$
δ	Balke[37]	1988	$0.7486 \pm 0.0026(\text{stat}) \pm 0.0028(\text{syst})$
$P_\mu\xi$	Beltrami[38]	1987	$1.0027 \pm 0.0079(\text{stat}) \pm 0.0030(\text{syst})$
$P_\mu\xi$	Imazato[39]	1992	$1.0013 \pm 0.0030(\text{stat}) \pm 0.0053(\text{syst})$
$\frac{P_\mu\xi\delta}{\rho}$	Jodidio[40]	1986	> 0.99682

Data Group (PDG) [2].

$P_\mu\xi$ was determined by Beltrami *et al.* in a muon spin resonance (μ SR) experiment at the Schweizerisches Institut für Nuclearforschung (SIN), now called the Paul Scherrer Institut (PSI) [38]. Muons from pion decay in flight were stopped in a Be target. The muon spin precessed in a 30 G transverse magnetic field. The decay positrons were counted in a positron telescope. The resulting spectrum was fit over a $3\tau_\mu$ period yielding the asymmetry parameter, $P_\mu\xi$.

A complementary μ SR measurement was performed at the National Laboratory for High Energy Physics (KEK) in Japan. The experiment utilized muons produced from decays of kaons at rest in a thin platinum target. The resulting muon beam was stopped in an aluminum target within a 105 G transverse magnetic field. Decay positrons were detected in either of two sets of drift chambers. The value from the subsequent fit of the spectrum is reported separately from the Beltrami value by the PDG to allow for differences in the initial muon polarization due to differences in

pion and kaon decay [2].

3. $P_\mu \xi \delta / \rho$ Measurement

$P_\mu \xi \delta / \rho$ is determined by measuring the momentum endpoint in the direction anti-parallel to P_μ . Jodidio *et al.* measured the parameter in an experiment at TRIUMF [40]. Muons were stopped in various metal foils (Ag, Al, Au and Cu) or liquid He. The muon spin was held by a magnetic field oriented parallel to the spin. Decay positrons with momentum approximately anti-parallel to the spin were focused into a series of drift chambers located upstream and downstream of a region with a transverse field.

4. δ Measurement

Balke *et al.* measured δ utilizing μ SR techniques [37]. The experiment used the same setup as the Jodidio experiment with the exception of the change to a transverse field in the stopping target. A fit of the resulting spectrum yielded the amplitude of the oscillation from which δ is determined.

5. η Measurements

The PDG value for η comes from both the Derenzo measurement noted above [32] and a measurement by Burkard *et al.* at SIN [35]. Burkard measured the transverse components of the decay positron polarization. Muons from pion decay were stopped in a graphite target located within a field oriented transverse to the muon spin and parallel to the average selected positron momentum. The positrons passed through a magnetized foil where a fraction annihilated with electrons. The resulting γ intensity distribution was measured in a set of four NaI detectors. Measuring the transverse components of the polarization determines η . Burkard found $\eta = 0.011 \pm 0.085$ where the error is affected by correlations with another muon decay parameter, η'' . Burkard

reduced the error by performing a global fit yielding $\eta = -0.007 \pm 0.013$.

A recent publication by Danneburg *et al.* at PSI has announced a new measurement of η [36]. The detector is schematically similar to the one from the previous experiment. However, all of the major components have been replaced by equipment with improved designs. The muons stop in a Be target and the γ intensity distribution is measured in an array of 127 $\text{Bi}_4\text{Ge}_3\text{O}_{12}$ scintillators. η is determined along with three other parameters, η'' , α'/A and β'/A [9], from a fit to a sum of Monte Carlo produced distributions. The fit obtained $\eta = 0.071 \pm 0.037(\text{stat}) \pm 0.005(\text{syst})$. A global fit has not yet been performed in an attempt to reduce the errors. Instead, η has been evaluated in the context of models where the only addition to the standard model couplings is a non-zero g_{RR}^S . Within this class of models, Danneburg finds $\eta = -0.0021 \pm 0.0070(\text{stat}) \pm 0.0010(\text{syst})$.

E. TWIST Measurement

The TRIUMF Weak Interaction Symmetry Test (TWIST) collaboration is attempting to measure ρ , δ and $P_\mu\xi$ with a precision of a few parts in 10^4 . The collaboration is the first to measure the Michel parameters with a blind analysis. TWIST reconstructs the decay positron spectrum as a function of momentum and angle relative to the muon polarization. The Michel parameters are extracted by fitting the spectrum to spectra generated by analyses of Monte Carlo simulations.

The experiment is subdivided into multiple phases, the first of which entails a measurement of ρ and δ with a precision of approximately a part in 10^3 . This measurement represents an improvement in precision of a factor of $\sim 3/2$ for ρ and ~ 3 for δ . This first ρ measurement is the subject of this dissertation.

CHAPTER II

APPARATUS

A. Overview

The TWIST measurements are performed at the Tri-University Meson Facility (TRIUMF) located on the campus of the University of British Columbia in Vancouver, B.C., Canada. The primary beam is a proton beam from the TRIUMF 500 MeV cyclotron. TWIST uses a secondary beam line, M13, located in the Meson Hall. M13 transports a mixed beam of muons, positrons and pions to the TWIST detector housed within a 2 T magnetic field aligned parallel to the beam. The muons are stopped in the center of a stack of thin planar drift chambers and multi-wire proportional chambers oriented perpendicular to the beam. The subsequent decay positrons spiral through one half of the detector stack. Particles passing through the chambers produce signals indicating the position and time of passing. The signals are collected and recorded by the data acquisition system for subsequent analysis. A conceptual view of the detector in the magnet is shown in Fig. 6.

B. Beam Line

1. Production Target

M13 is located at the T1 production target. T1 was a Be target encased in a stainless steel water jacket for the 2002 running. Pions produced in T1 decay with a lifetime of 26 ns. Pion decay to a muon and a neutrino yields a well defined muon momentum (29.79 MeV/c) and muon spin (anti-parallel to the muon momentum) in the rest frame of the pion. TWIST utilizes two distinct beam line settings for data taking, designated “surface” and “cloud” muon beams. The surface muon beam tune selects

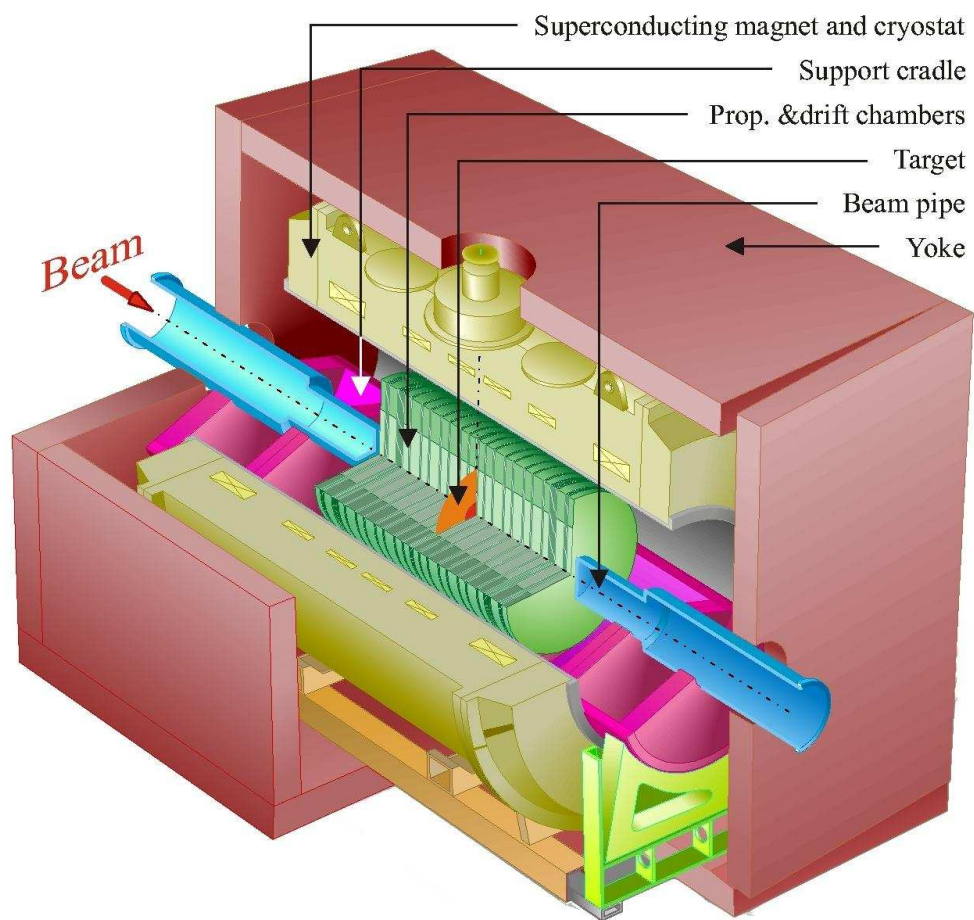


Fig. 6. Conceptual view of TWIST detector.

muons of momentum 29.6 MeV/c with $\sim 1\%$ momentum bite. Surface muons are so called because they come from pions decaying at rest on the surface of the production target. The TWIST surface muon beam has a high negative polarization in the TWIST coordinate system. The cloud muon tune selects muons of momentum 32.8 MeV/c. Cloud muons come from pions that decay in flight. The cloud beam is a mixture of forward decaying muons from pions with ~ 3.0 MeV/c momentum and backward decaying muons from pions with ~ 62.6 MeV/c momentum. The momentum-spin correlation and the pion momentum spectrum combine such that the TWIST cloud beam has a net positive polarization of $\sim 1/4$.

2. M13

M13 consists of two dipole magnets (B1 and B2), three vertically focusing quadrupole magnets (Q1, Q4 and Q7) and four horizontally focusing quadrupole magnets (Q2, Q3, Q5 and Q6) arranged symmetrically about the midpoint of the beam line as illustrated in Fig. 7. The beam rate is controlled with a set of vertical jaws (F0VJ) and horizontal slits (F0HS) located between Q2 and B1. The muon rate was typically 3 kHz for surface beams and 600 Hz for cloud beams. M13 has two foci, F1 and F2, between the dipole magnets, each of which has a set of horizontal slits, F1HS and F2HS, respectively. F1HS provides the momentum selection with a 1% acceptance. The slit settings were unchanged between surface and cloud beams and are shown in Table VIII.

3. M13 Simulation

The M13 beamline has been simulated with GEANT3 and ZGOUBI to study beam tune optimization as a function of muon rate, muon depolarization and beam divergence and size at the entrance to the solenoidal field. Though extensive efforts have

Table VIII. M13 slit settings. Slit settings yielding 1% momentum acceptance and emittance of $\pi \times 5\text{mm} \times 16\text{mr}$.

Jaws or Slits	Position	Width
FOVJ	NA	9 mm
FOHS	0 mm	41 mm
F1HS	0 mm	10 mm
F2HS	0 mm	20 mm

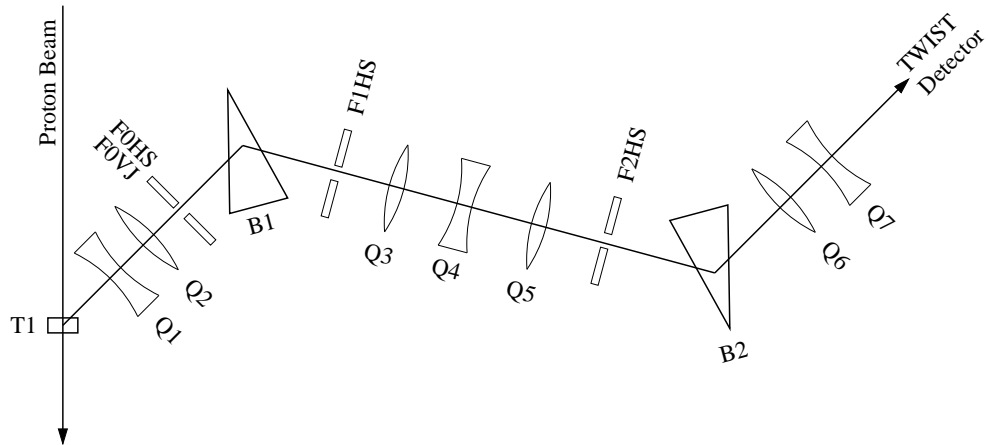


Fig. 7. Schematic of M13 beamline. T1 is beryllium production target. B1 and B2 are dipole magnets. Q1, Q4 and Q7 are vertically focusing quadrupole magnets. Q2, Q3, Q5 and Q6 are horizontally focusing quadrupole magnets. FOHS, F1HS and F2HS are horizontal slits and FOVJ are a set of vertical jaws. F1HS in combination with B1 provides the momentum selection. It is 10.33 m from T1 to the TWIST trigger scintillator.

been spent in these endeavors, most of the energy has been devoted to understanding and minimizing depolarization which is not critical for a measurement of ρ . However, the beam characteristics reported earlier are the result of using a beam tune derived from these studies.

4. Beam Measurement

Measurements of the beam shape position and divergence were made with a specialized apparatus placed between Q7 and the detector 154 cm upstream of the central stopping target. These measurements test the M13 beamline simulations and provide input parameters for the beam used in the Monte Carlo event simulation. The apparatus consists of a movable slit, a pair of wire chambers and a pair of scintillators as illustrated in Fig. 8. The slit is a 2 mm wide gap that can be oriented horizontally or vertically. The slit can be moved vertically when oriented horizontally and vice versa. One wire chamber is oriented to measure the horizontal position and the other measures the vertical position. The scintillators reside downstream of the wire chambers. The first is a thin plastic scintillator providing a muon trigger. The second is a plastic scintillator providing a veto for beam positrons. In combination with the slit the chambers can be used to measure the horizontal and vertical divergences. Without the slit, the chambers measure the beam spot in both horizontal and vertical dimensions simultaneously.

5. Beam Tunes

TWIST ran with a total of six distinct beam tunes in the 2002 run, three of which contributed to the data used in fitting Michel parameters. Two of these three are surface muon tunes. The third is a cloud muon tune selecting muons with momentum of 32.8 MeV/c, well above the 29.79 MeV/c momentum limit of surface muons.

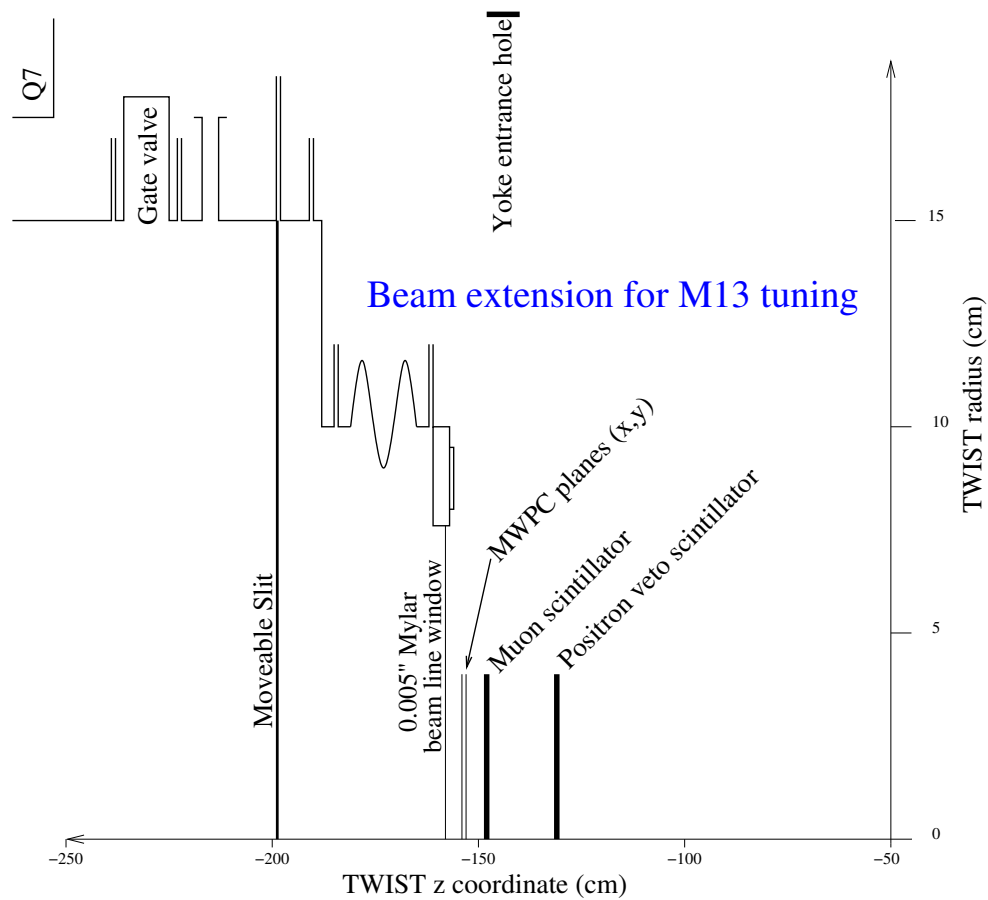


Fig. 8. Beam measurement apparatus. Muon scintillator provides trigger. Beam characteristics measured in multi-wire proportional chambers (MWPC's) after passing through slit. Position of positron veto scintillator not shown precisely.

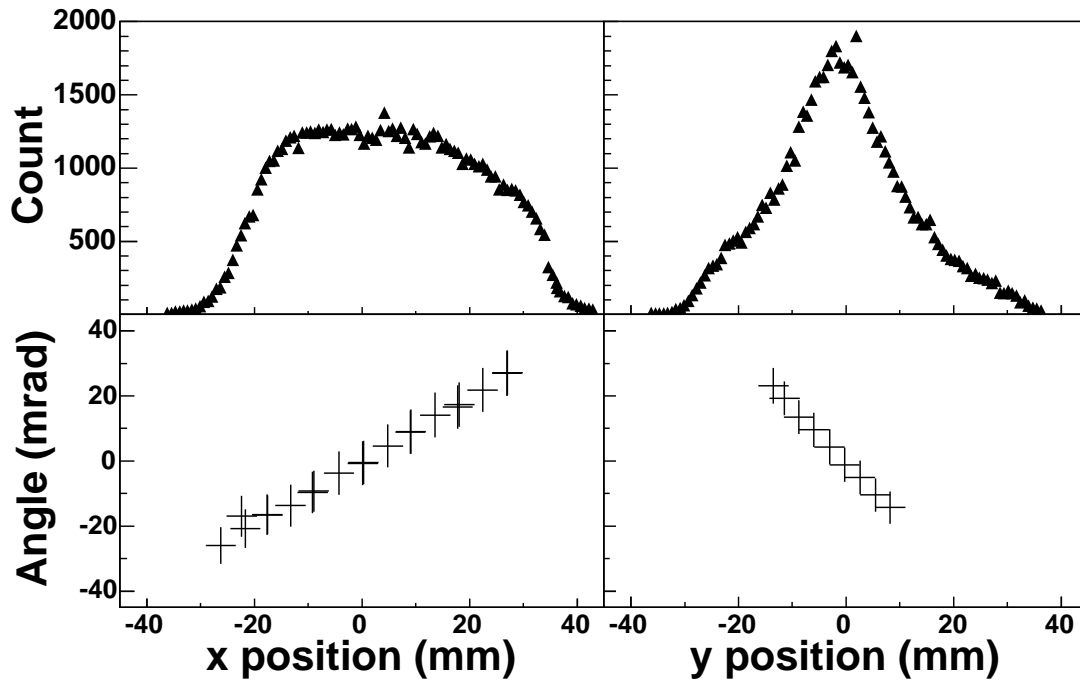


Fig. 9. Beam characterization for Post-Oct23 surface muon beam. Top left - horizontal profile. Top right - vertical profile. Bottom left - horizontal divergence vs. x . Bottom right - vertical divergence vs. y .

The method of setting and monitoring the M13 quadrupole magnets was updated during the fall of 2002. It was subsequently discovered that the assumed relationship between the two magnet settings was incorrect. This resulted in the two surface muon tunes. The two tunes are referred to as the “Pre-Oct23” and “Post-Oct23” tunes in reference to the date of the implementation of the new method. Note that there was no change in the setting of the dipole magnets and hence no change in the momentum selection. Figures 9, 10 and 11 show the position, shape and divergence of the Post-Oct23, Pre-Oct23 and Cloud beams.

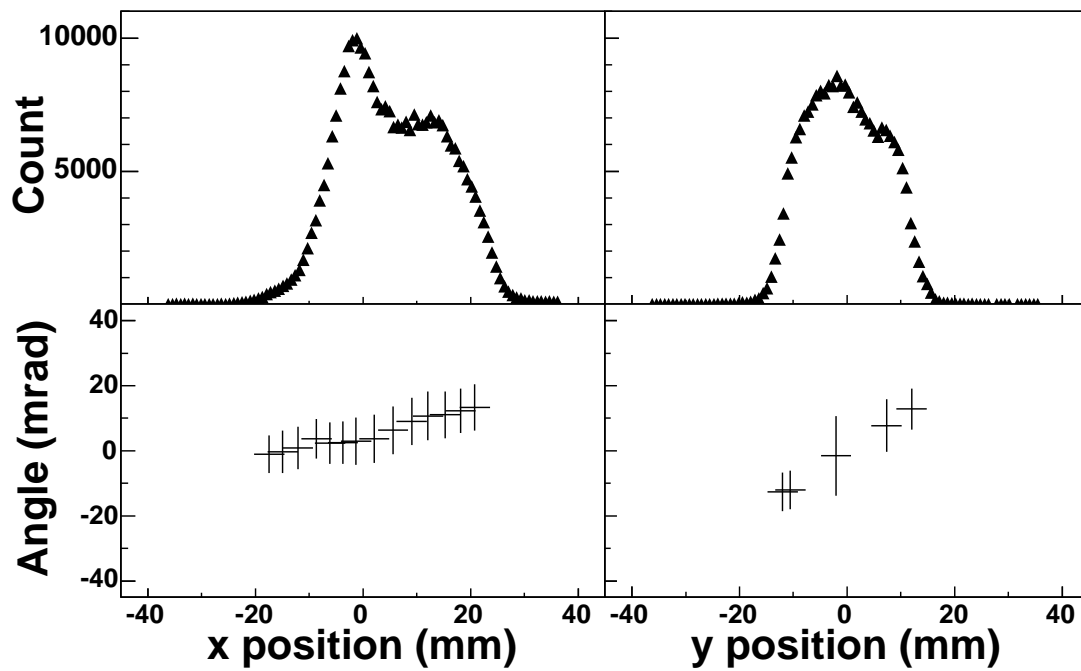


Fig. 10. Beam characterization for Pre-Oct23 surface muon beam. Top left - horizontal profile. Top right - vertical profile. Bottom left - horizontal divergence vs. x. Bottom right - vertical divergence vs. y.

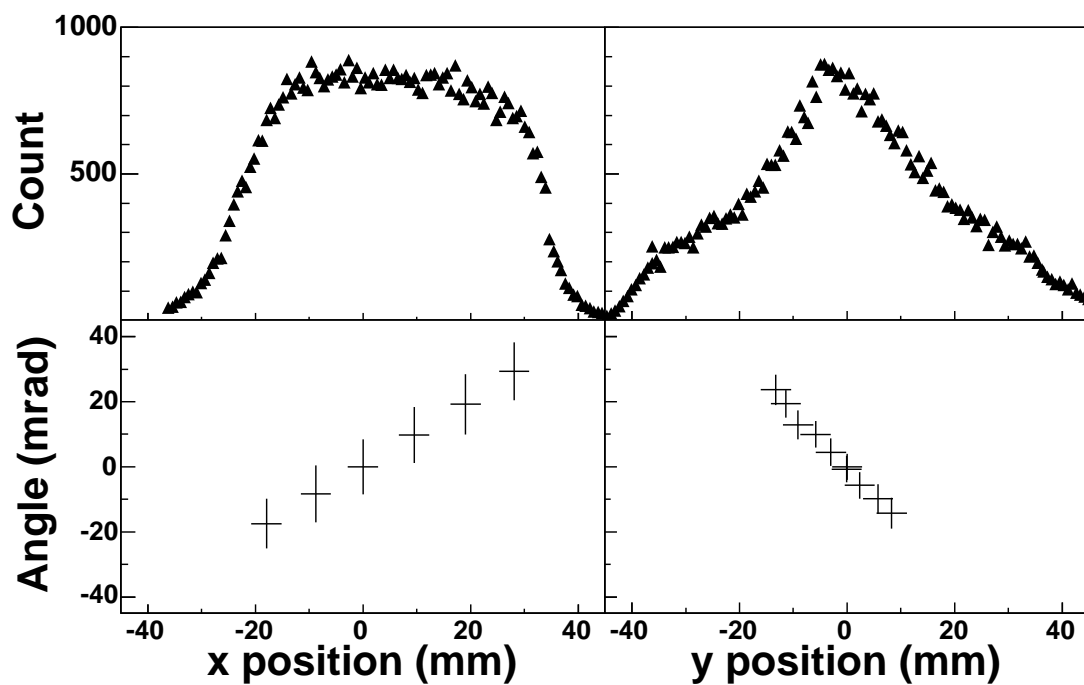


Fig. 11. Beam characterization for cloud muon beam. Top left - horizontal profile. Top right - vertical profile. Bottom left - horizontal divergence vs. x. Bottom right - vertical divergence vs. y.

C. Solenoid

The solenoidal field is provided by a super-conducting MRI magnet located within a large steel yoke. The yoke effects both the uniformity of the field in the tracking volume and the shape of the field at the extremes. The standard 2 T central field is uniform to 0.4% and known to ± 1 G within the tracking volume. The field is stable over time, decaying by 0.2 G over the 2002 run (3 1/2 months). The shape of the field as seen by an incoming muon is critical for measurements of P_μ , but not ρ , and is not discussed here in detail.

1. Field Measurements

A field mapper was designed and built to measure the field in both the tracking volume and in the region about the entrance to the magnetic yoke. The mapper measures the longitudinal component of the field throughout the tracking volume at increments of 5 cm in the longitudinal direction, 4.13 cm in the radial direction and 15° in the azimuthal direction. The measured field is shown in Fig. 12.

2. Field Simulation

Track simulation and reconstruction requires knowledge of the magnetic field at all locations within the tracking volume. The map provided by the field mapper provides the longitudinal component of the field at discrete positions. A magnetic field simulation is run to generate a full three component field map. The simulation provides a much finer grid than the measured field map and effectively smooths over the roughness due to measurement errors. The final interpolation is performed between points on the grid as needed during event simulation and reconstruction. OPERA 3D is used to produce the field simulation. The OPERA map is within ± 2 G of the

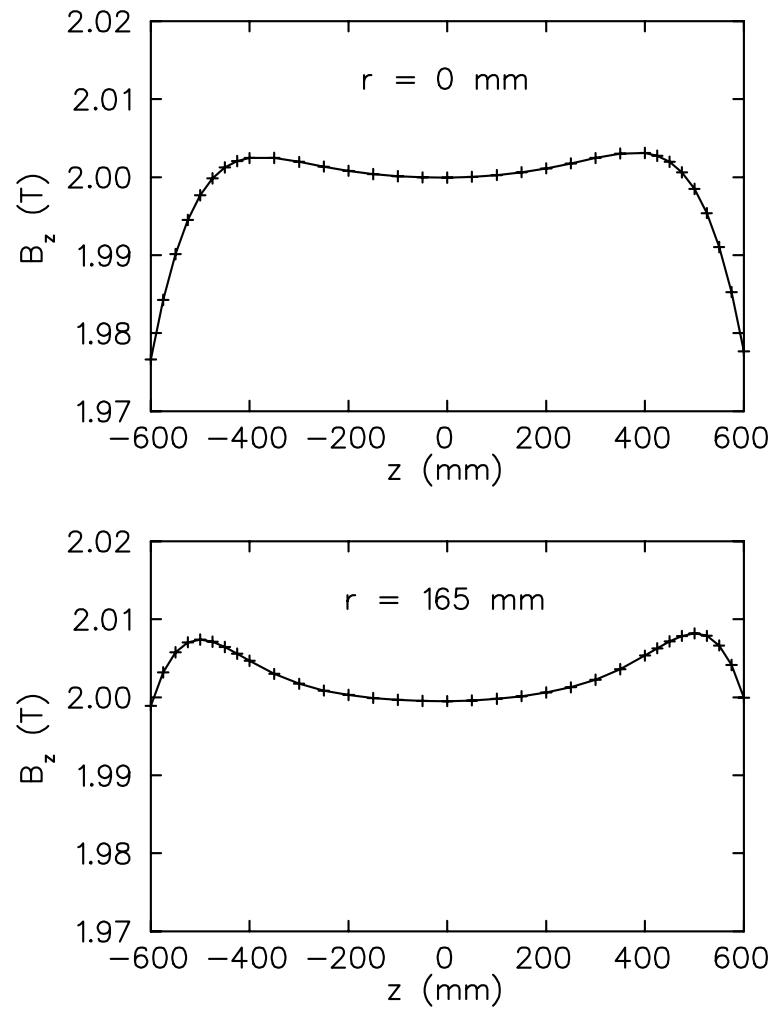


Fig. 12. Measured longitudinal magnetic field. Top - measured along the z axis. Bottom - measured 16.5 cm from the z axis.

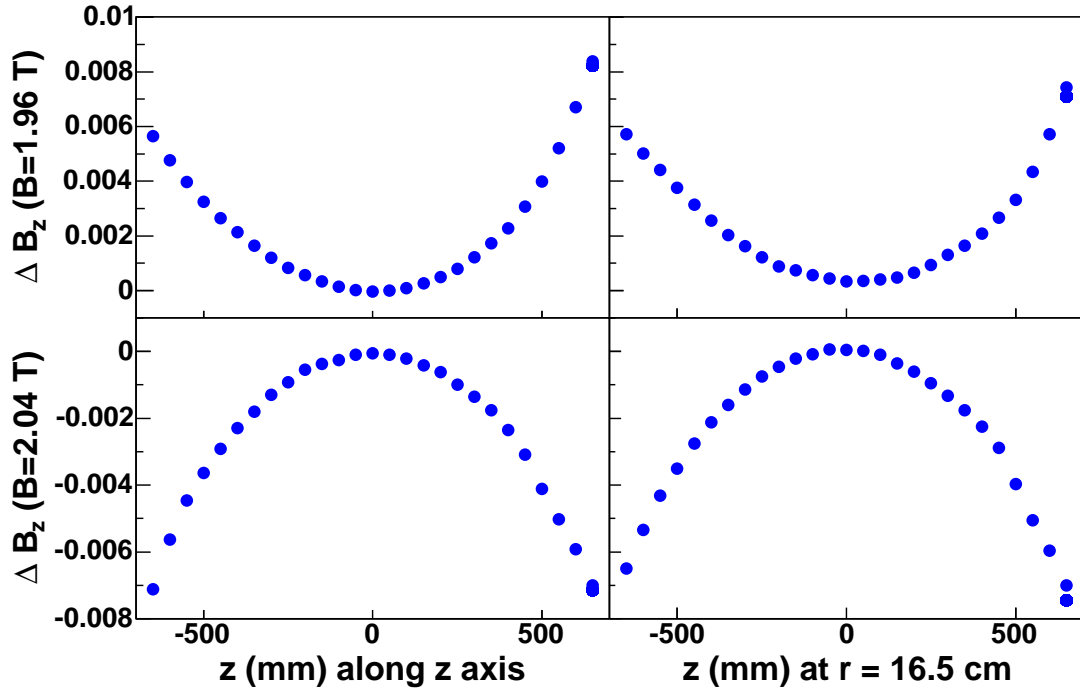


Fig. 13. Scaled field accuracy. Difference between scaled OPERA produced fields and the 1.96 T and 2.04 T fields: Top plots show $B_z[1.96\text{T}] - B_z[\text{Scaled}]$ vs. z , Bottom plots show $B_z[2.04\text{T}] - B_z[\text{Scaled}]$ vs. z ; Left plots are calculated along the z axis, Right plots are calculated 16.5 cm from the z axis.

measured 2 T field for all points within the tracking volume.

3. Field Map Scaling

Additional field maps are needed for the 1.96 T and 2.04 T fields. Maps for these two fields were generated by scaling the OPERA produced 2 T map such that the field at the origin matched the measured value for each of the two settings. Figure 13 shows the difference between the scaled version of the OPERA field and the measured field for both the 1.96 T and 2.04 T fields. In each case, the differences at the extremes of the tracking volume are ~ 4 G.

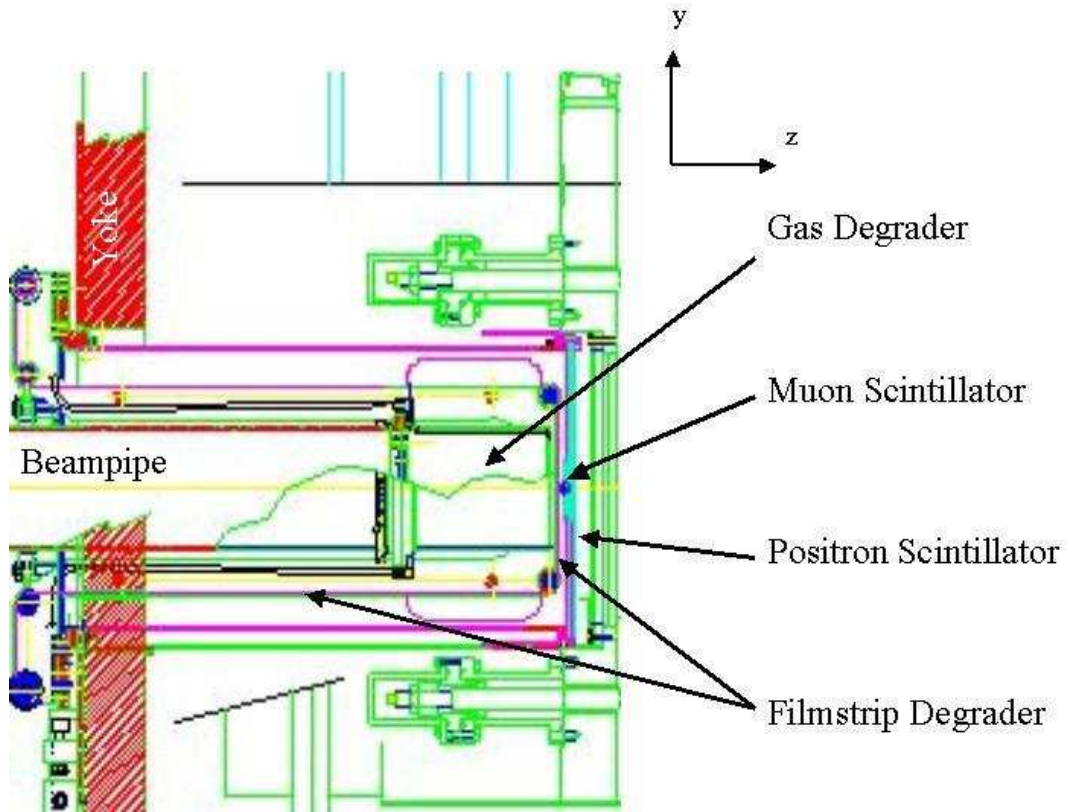


Fig. 14. Beam package.

D. Detector

The TWIST detector is described in detail in [41].

1. Beam Package

The components between the end of M13 and the detector are designated the “beam package”. The beam package consists of a gas degrader, a muon scintillator, two positron scintillators and a filmstrip degrader (see Fig. 14).

The gas degrader is a 21.67 cm long chamber containing a mixture of He and CO₂ that can be tuned to stop muons in the stopping target. The nominal setting

for the 2002 running was 95% He and 5% CO₂ at atmospheric pressure.

The muon scintillator provides the trigger. The scintillator is a 195 μm thick plastic disk (Bicron BC408) of radius 3 cm located 80 cm upstream of the central stopping target. The light guide is a strip of Plexiglas, the ends of which are attached to a pair of photo-multiplier tubes, designated M1 and M2. The output of M1 and M2 are used individually and as a linear sum, denoted M12. The nominal trigger is a coincidence of M1, M2 and M12.

The positron scintillators are plastic disks (Bicron BC408) with a cylindrical hole through the center to accommodate the muon scintillator. Each positron scintillator has an inner radius of 3 cm, an outer radius of 18.5 cm and a thickness of 6.35 mm. These scintillators are located just downstream of the muon scintillator. A Bicron fiber (BCF99-AA) wrapped around the circumference of each scintillator serves as a light guide. Each end of each fiber is attached to a photo-multiplier tube, yielding four positron scintillator signals.

The filmstrip degrader is a strip of Mylar containing several sites with various thicknesses of degrader material, including a site with no degrader (a hole), one of which is inserted into the path of the incoming muon beam. The nominal setting placed the hole in the beam resulting in no additional degrader material. Other settings that were used are discussed in the context of specific data sets. The filmstrip degrader is located 2.5 mm upstream of the muon scintillator.

2. Stack

The detector stack consists of 44 drift chambers (DC's) and 12 multi-wire proportional chambers (MWPC's) arranged symmetrically about a central stopping target as shown in Fig. 15. The stack is ~ 120 cm in length. The tracking region is defined by the DC's and constitutes the interior of a cylinder 1 m in length and with a radius

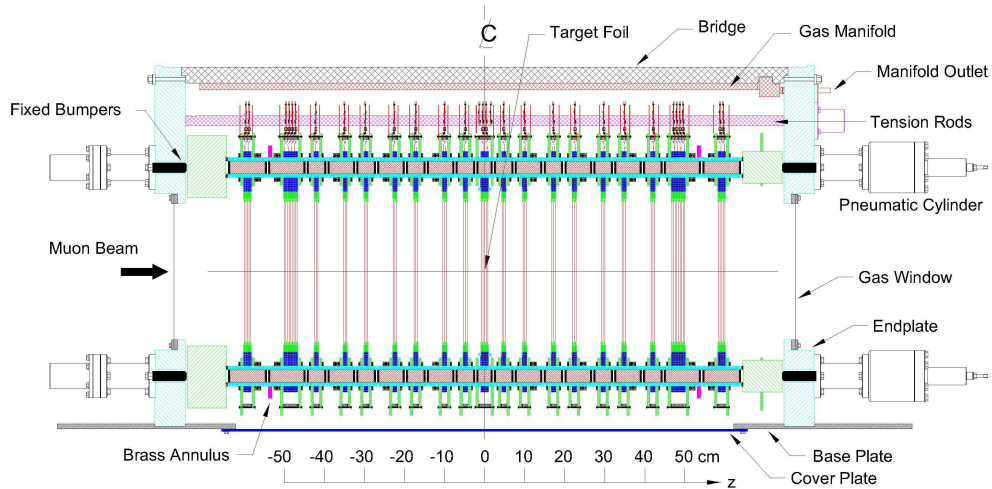


Fig. 15. Side view of TWIST detector. Muon beam goes from left to right.

of 16 cm. The entire stack is contained within a helium volume. 3% nitrogen is added to the helium to prevent sparking between electronic components within the helium volume.

The DC's are made with 80 sense wires with 4 mm spacing within a plane. Figure 16 shows an end view of a drift chamber in the detector. A pair of doubly aluminized Mylar cathode foils are located 2 mm on either side of the wire plane. The central 28 chambers (14 upstream and 14 downstream of the target) are fabricated in pairs such that they share the cathode foil between them. Each pair contains one wire plane rotated 45° and another rotated -45° from the horizontal, providing a two-dimensional orthogonal coordinate system. These central DC pairs are separated by alternating helium gaps of ~ 44 mm and ~ 64 mm, forming upstream and downstream “sparse stacks”. The outer 16 chambers are fabricated in two “dense stacks” of 8 chambers each, one upstream and one downstream. All internal cathode foils in a dense stack are shared between two chambers. The dense stack wire planes are rotated

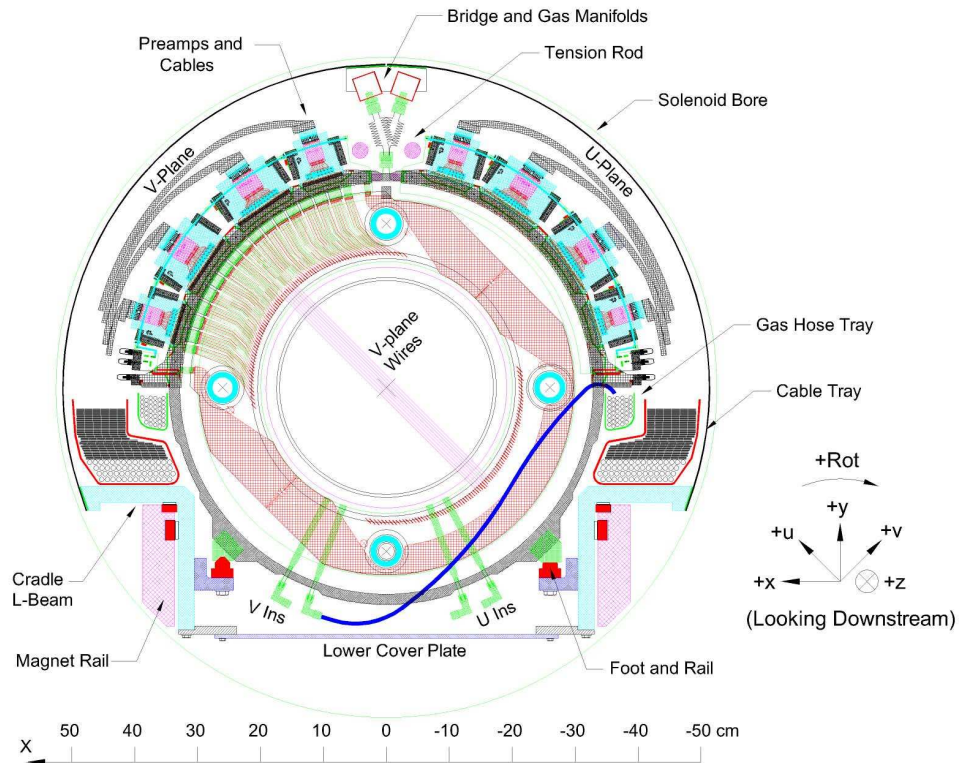


Fig. 16. End view of drift chamber.

such that each chamber is adjacent to at least one chamber with the orthogonal orientation. In order, the rotations are -45° , $+45^\circ$, -45° , $+45^\circ$, $+45^\circ$, -45° , $+45^\circ$ and -45° . The 6 most upstream and 6 most downstream chambers had only the central 48 wires instrumented during the 2002 data collection due to a shortage of available time-to-digital converters. The primary purpose of the DC's is to provide position information for the track reconstruction. To meet the requirement of good position resolution, the chambers contain dimethylether gas.

The MWPC's are constructed similar to the DC's differing only in the number and spacing of wires, the drift gas and the arrangement of chambers. Each MWPC contains 160 sense wires with 2 mm spacing. The outer 8 MWPC's are manufactured

in two modules of 4 chambers each, one upstream of all DC's and one downstream of all DC's. Like the DC dense stacks, these outer MWPC's share internal foils. The central 32 wires of each of the outer MWPC's are read individually. The outer 128 wires of the outer MWPC's are connected in groups of 4 consecutive wires. Each connected group is read as if it were a single wire. The central 4 MWPC's and the stopping target constitute the target module. The stopping target serves as the central cathode foil for this module. The other two internal cathodes are the standard doubly aluminized Mylar foils. MWPC's in the target module have only the central 48 wires instrumented. All MWPC's are rotated by $\pm 45^\circ$ in an alternating pattern. The primary purpose of the MWPC's is to provide timing information for particle identification and separation. To this end the MWPC's use CF_4 /isobutane as the drift gas in the ratio 80/20. With CF_4 /isobutane, the MWPC's have a time resolution of a few ns.

The entire stack is supported on four sets of high precision ceramic spacers. The ceramic spacers provide for precise longitudinal positioning of detector components as well as position stability over time. The longitudinal positioning was tested by comparing a measurement of the total length to the calculated length. The difference from the nominal length (~ 1084 mm) was found to be $23 \mu\text{m} \pm 25 \mu\text{m}$. The ceramic spacers and the length test are described in more detail in [41].

The stopping target for 2002 was a $125 \mu\text{m}$ thick Mylar foil coated with a $10 \mu\text{m}$ layer of graphite paint on each side. The graphite provided the conducting layer necessary for it's use as a cathode foil.

The TWIST coordinate system is defined relative to the detector with the origin at the center of the steel yoke (the location of the central stopping target). The z -axis is parallel to the longitudinal axis of the detector such that the beam particles have $p_z > 0$ and the z component of the magnetic field is positive. The y -axis is

vertical with positive y up. The x -axis is horizontal such that (x,y,z) forms a right-handed Cartesian coordinate system (positive x to the left when looking downstream). TWIST also uses a coordinate system rotated 45° about the z -axis labeled (u,v,z) that corresponds to the orientation of the DC's and MWPC's and hence the quantities they measure (see Fig. 16). θ is the angle relative to the z -axis and ϕ is the azimuthal angle in the $u - v$ plane measured from the u -axis.

E. Slow Controls

Conditions that have the capability of varying significantly are monitored by a system designated "Slow controls". Four types of parameters are monitored by slow controls:

1. Environmental conditions over which the experimenter has no control,
2. Settings that must be adjusted independent of slow controls,
3. Settings that can be set utilizing the slow controls interface and
4. Settings that can be automatically adjusted by slow controls based on comparison of the monitored values to a pre-determined range.

The M13 dipoles are examples of automatically adjusted devices. Slow control monitors the NMR measurements and adjusts the currents to keep the field within 0.2 G of the set value.

Slow control data is calibrated and written to an on-line database (ODB) at 60 s intervals. Any of the parameters can be instantly plotted as a function of time. A critical subset is automatically plotted and surveyed by the experimenter on shift on a regular basis. In addition, slow control data is written into the experimental data stream in both raw and calibrated forms. These slow control events are recorded at the beginning of each run and whenever a read value differs from the previously

Table IX. Slow control variables. Examples of Slow control monitored variables. Types of measurements: 1 - conditions outside direct control; 2 - parameter adjusted independent of slow controls; 3 - parameter adjusted via slow control interface; 4 - parameter adjusted automatically by slow controls.

Measured quantity	Type	Measured quantity	Type
Proton beam current	1	M13 dipole settings	4
		M13 quadrupole settings	2
Chamber gas flows	2	M13 slit and jaw settings	2
Chamber temperatures	1		
Chamber pressures	2	Solenoid field	2
Atmospheric pressure	1	Solenoid support strains	1
Gas degrader gas ratio	3	Solenoid temperatures	1
DAQ crate voltages	2	Scintillator scalars	1
Chamber high voltages	3	Fastbus scalars	1
Chamber high voltage ramp up	4		

written value by more than a predetermined threshold. A list of some parameters monitored by slow controls is given in Table IX.

F. Data Acquisition

The data acquisition system (DAQ) handles the digitization of signals, grouping of data into events and writing of data to tape. The DAQ can process 5000 events per second. Typical event size is 1500 B.

1. Hardware

The signals from the DC's and MWPC's are amplified within the detector by VTX pre-amplifiers. The resulting signals are carried along micro-coaxial cables to the post-amplifier discriminators. The post-amplifier discriminators provide a gain of 20 and use a time over threshold discriminator circuit to digitize the signals. The signals are then carried along twisted pair ribbon cables to the time-to-digital converters (TDC's) in two fastbus crates. The TDC's are Lecroy Fastbus TDC's, models 1877 and 1877s. The TDC's have 96 channels, a 16 μ s range and 0.5 ns per count. A VxWorks Power PC located in each Fastbus crate controls the Fastbus. Data is written out on 160 GB SuperDLT tapes.

2. Software

The data is organized into events and written to tape by DAQ. The system used is the Maximum Integrated Data Acquisition System (MIDAS) developed at the Paul Scherrer Institute and at TRIUMF. MIDAS runs on a Pentium processor running Linux. In addition to event writing, MIDAS provides log files and the user interface with DAQ. Various other machines contain the slow control processes, the on-line database, the on-line analysis, the chamber high voltage connections and the M13 controls. However, all of these are easily accessible either through the MIDAS interface or through other programs running on the main MIDAS machine, so that this machine is the central point of contact for the experimenter on shift.

CHAPTER III

DATA

A. Data-taking Strategy

Five data sets and eight distinct systematic sets were collected during the fall of 2002. Each set had approximately 3×10^8 triggers, sufficient to achieve a statistical precision for ρ of ~ 0.0007 . Typical sets were collected in less than forty-eight hours. The cloud set, described below, was the biggest exception, taking a few weeks due to the low rate. Several additional sets of various sizes were taken, providing data for calibrations and Monte Carlo verification studies. Data taking began on August 23, 2002 and ended on December 9, 2002.

B. Data Sets

Each of the five data sets were taken with most conditions optimized for the measurement of ρ and δ . Two parameters, magnitude of the magnetic field and beam polarization, were purposely varied between sets. The choice of magnetic field in combination with the detector design determines the geometrical acceptance. Rather than optimize the magnetic field strength, TWIST took measurements at three different magnitudes of magnetic field to confirm that there were no strong field dependencies in the measurements. Each of the three field settings was appropriate to include approximately half of the phase space. Three data sets had a central field of 2 T, one had a central field of 1.96 T and one had a central field of 2.04 T. Four of the data sets were taken with a surface muon beam. The fifth set, one of the sets with a central field of 2 T, was taken with a cloud muon beam. The low and high field sets provide a test of the assumption that the observed Michel parameters are independent of the

Table X. Data sets. Data sets used in the extraction of the Michel parameter ρ . Polarization is the average polarization at the time of decay.

Data Set	Central Field	Polarization (P_μ)	Triggers	Events in Fiducial
Nominal A	2.00 T	-0.895	1.34×10^8	7.82×10^6
Nominal B	2.00 T	-0.898	2.80×10^8	1.58×10^7
Low Field	1.96 T	-0.889	2.86×10^8	1.64×10^7
High Field	2.04 T	-0.893	2.23×10^8	1.28×10^7
Cloud	2.00 T	+0.217	5.99×10^8	1.23×10^7

precise field. Likewise, the cloud set tests whether the observed ρ is independent of the muon polarization.

The two surface muon sets taken with a central field of 2 T were taken with two different quadrupole settings due to the change in settings noted in Sec. B. Consequently, the 2 T surface muon sets, Nominal A (Pre-Oct23 tune) and Nominal B (Post-Oct23 tune), use slightly different beam tunes. A summary of data sets is given in Table X.

C. Systematic Sets

The determination of systematic uncertainties is described in detail in Sec. V. The calculations require five types of systematic sets, each taken with a single condition varied from a standard data set. Each of these sets has statistics comparable to a data set. A summary of systematic sets is presented in Table XI.

Table XI. Systematic sets. Data taken for the evaluation of systematic uncertainties.
The lowered HV sets were not used directly in systematic fits.

Systematic Set	Modified Relative to Data Set	Triggers	Events in Fiducial
B2 + 10 G	Nominal A	2.84×10^8	1.53×10^7
Slightly Upstream	Nominal A	2.58×10^8	7.24×10^6
Downstream Al	Nominal B	1.32×10^8	7.62×10^6
High Rate	Nominal A	2.61×10^8	1.40×10^7
Low Rate	Nominal A	2.99×10^8	1.78×10^7
1900 V DC HV	Nominal B	2.88×10^8	NA
1850 V DC HV	Nominal B	2.77×10^8	NA
1950 V MWPC HV	Nominal B	2.58×10^8	NA

1. Beam Steering

The “B2 + 10 G” set is used to evaluate effects due to misalignment of the beam as it enters the magnetic field. For this set the second M13 dipole magnet was offset from the nominal by +10 G.

2. Stopping Distribution

The “Slightly Upstream” set had the gas degrader set to move the center of the muon stopping distribution slightly upstream. This set is used to study errors due to the shape of the stopping distribution in the stopping target.

3. Outside Materials

The “Downstream Al” set was taken to evaluate errors due to extra particles coming from interactions in the beam package components. This set was run with a 0.65 cm thick aluminum plate mounted on a 0.59 cm thick plastic plate placed 80 cm downstream of the central stopping target.

4. Trigger Rate

Errors due to event rates were studied by increasing and decreasing the rate by a factor of two. The trigger rate is adjusted by opening or closing the rate-determining jaws and slits in M13. The “High Rate” and “Low Rate” sets had trigger rates of 4.7 kHz and 1.2 kHz, respectively.

5. High Voltage

Three sets were taken to study the effect of high voltage variations. The “1900 V DC HV” and “1850 V DC HV” sets had the DC high voltage lowered from the nominal

high voltage by 50 and 100 V, respectively. The “1950 V MWPC HV” had the MWPC high voltage lowered from the nominal high voltage by 50 V. These sets were studied to distinguish between effects due to high voltage variations and foil bulging (Sec. 7).

D. Monte Carlo Verification Sets

Two sets were taken for use in Monte Carlo verification studies.

1. Dense Stack Stops

A set of data was taken of surface muons using the 0.020” setting of the filmstrip degrader. This results in a muon stopping distribution centered in the upstream DC dense stack. This set provides a source of positrons that traverse both halves of the detector with a decay positron range of momentum and angle.

2. Sparse Stack Stops

A set of data was taken of surface muons using the 0.010” setting of the filmstrip degrader and a 30% concentration of CO₂ in the gas degrader. This results in a muon stopping distribution centered in the upstream DC sparse stack. This set provides detector sensitivity to the shape of the muon stopping distribution by spreading the distribution over active DC’s rather than condensing it in the central stopping target.

E. Calibration Sets

Various sets were taken to provide data for calibrations and tuning.

1. 120 MeV/c Pions

Multiple sets were taken of 120 MeV/c pions passing through the TWIST detector with the solenoid field off. The M13 quadrupoles were tuned to produce a divergent beam for these sets and the second dipole magnet, B2, was varied between sets to provide a distribution of tracks that covered the entire detector. The trigger for these sets was provided by additional scintillators placed just outside of the downstream yoke plate. The 120 MeV/c pion sets were used for the calculation of alignment corrections and t_o calibrations. They were taken at the beginning of the fall run and repeated at the end of the run. The tracks were fit to straight lines to determine the transverse offsets of the centers of the chambers from the z -axis and the rotations of the chambers from their nominal u and v directions. The translational offsets were determined to 5 μm , and the rotational orientations were determined to 0.01° . In addition, the zero times of the wires were determined to a few ns.

2. Efficiency Sets

A series of sets were taken to evaluate DC and MWPC efficiencies. For each of these sets, a portion of the DC's or MWPC's would be operated with high voltage lowered from the nominal setting. The chambers being tested were alternated such that the efficiency of every DC and MWPC was calculated. Figure 17 shows the average efficiency of the DC's as a function of high voltage.

3. Gas Degradation Tuning

A series of sets were taken with incremental changes in the gas degrader settings. These sets were used to tune the gas degrader setting to center the muon stopping distribution in the central stopping target.

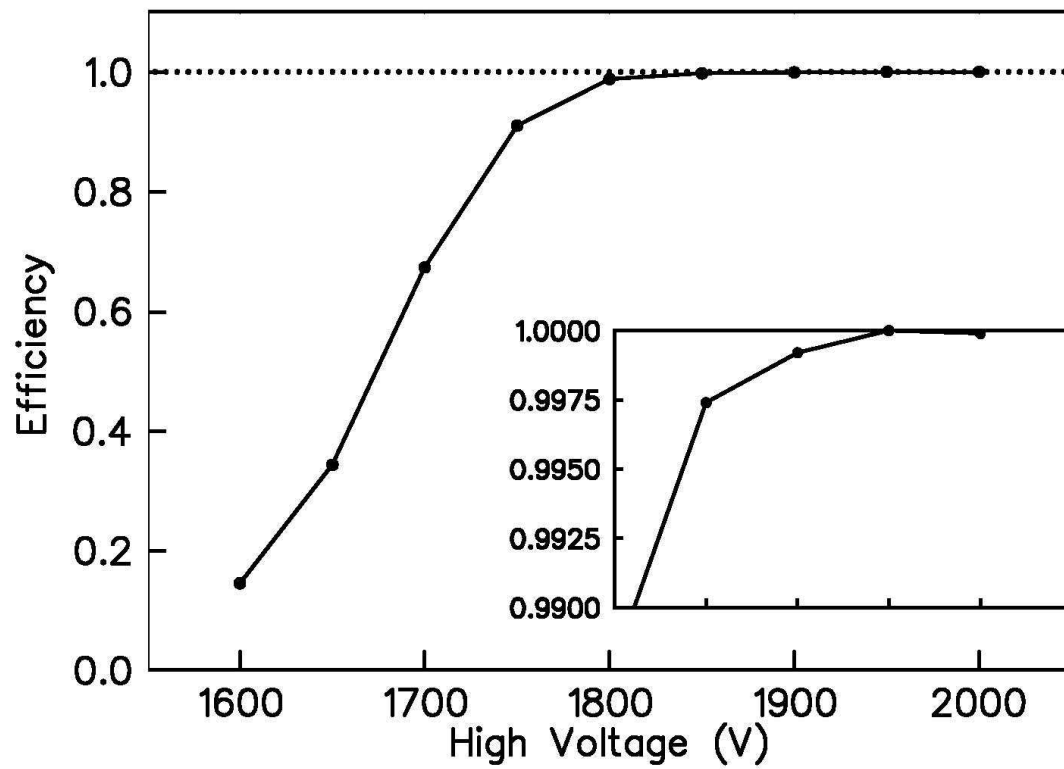


Fig. 17. DC efficiency as a function of high voltage. Inset shows close up of efficiency in the range near 100%.

CHAPTER IV

ANALYSIS

A. Analysis strategy

1. Analysis Overview

Michel parameters are determined from a fit of a decay spectrum derived from data to decay spectra derived from Monte Carlo. The key elements of the analysis are the computer simulations; the decay positron track reconstruction; the spectra generation and the Michel parameter fitting.

2. Linear Expansion

The TWIST analysis strategy exploits the linearity of the decay spectrum in the Michel parameterization. The spectrum is expanded about a point in parameter space, $\lambda_o = (\rho_o, \eta_o, (P_\mu\xi)_o, (P_\mu\xi\delta)_o)$, yielding

$$\begin{aligned}
\left[\frac{d^2\Gamma}{dx d(\cos\theta)} \right]^{(Data)} &= \left[\frac{d^2\Gamma}{dx d(\cos\theta)} \right]_{\lambda_o}^{(MC)} \\
&+ \frac{\partial}{\partial\rho} \left[\frac{d^2\Gamma}{dx d(\cos\theta)} \right]_{\lambda_o}^{(MC)} \Delta\rho \\
&+ \frac{\partial}{\partial\eta} \left[\frac{d^2\Gamma}{dx d(\cos\theta)} \right]_{\lambda_o}^{(MC)} \Delta\eta \\
&+ \frac{\partial}{\partial(P_\mu\xi)} \left[\frac{d^2\Gamma}{dx d(\cos\theta)} \right]_{\lambda_o}^{(MC)} \Delta(P_\mu\xi) \\
&+ \frac{\partial}{\partial(P_\mu\xi\delta)} \left[\frac{d^2\Gamma}{dx d(\cos\theta)} \right]_{\lambda_o}^{(MC)} \Delta(P_\mu\xi\delta) \quad (4.1)
\end{aligned}$$

The linearity of the Michel parameterization guarantees that this expansion is mathematically exact. This fitting procedure requires six spectra, or more precisely, six 2-dimensional histograms of yield as a function of x and $\cos\theta$; a data spectrum, a

Monte Carlo “base” spectrum generated with Michel parameters, ρ_o , η_o , $(P_\mu\xi)_o$ and $(P_\mu\xi\delta)_o$, and four “derivative” spectra. The fit of each data set required a corresponding Monte Carlo set generated with conditions matching the data set. The calculation of some systematic uncertainties requires a fit of one data set to another or one Monte Carlo set to another. Such data to data and Monte Carlo to Monte Carlo fits also use the four standard Monte Carlo derivative sets. The derivatives are:

$$\begin{aligned} \frac{\partial}{\partial\rho} \left[\frac{d^2\Gamma}{dx d(\cos\theta)} \right] &= k(x) \frac{2}{9} (4x^2 - 3x - x_o^2) \\ \frac{\partial}{\partial\eta} \left[\frac{d^2\Gamma}{dx d(\cos\theta)} \right] &= k(x) x_o (1 - x) \\ \frac{\partial}{\partial(P_\mu\xi)} \left[\frac{d^2\Gamma}{dx d(\cos\theta)} \right] &= k(x) \frac{1}{3} \cos\theta \sqrt{x^2 - x_o^2} (1 - x) + \text{R.C.} \\ \frac{\partial}{\partial(P_\mu\xi\delta)} \left[\frac{d^2\Gamma}{dx d(\cos\theta)} \right] &= k(x) \frac{2}{9} \sqrt{x^2 - x_o^2} (4x - 4 + \sqrt{1 - x_o}) \end{aligned}$$

where $k(x) = (m_\mu/4\pi^3) W_{\epsilon\mu}^4 G_F^2 \sqrt{x^2 - x_o^2}$ and R.C. refers to the radiative corrections detailed in [11, 12, 13]. The fit values $\Delta\rho$, $\Delta\eta$, $\Delta(P_\mu\xi)$ and $\Delta(P_\mu\xi\delta)$ from Eq. 4.1 yield offsets from the four inputs to the Monte Carlo base set. Thus the measured Michel parameters are

$$\begin{aligned} \rho &= \rho_o + \Delta\rho, \\ \eta &= \eta_o + \Delta\eta, \\ P_\mu\xi &= (P_\mu\xi)_o + \Delta(P_\mu\xi) \text{ and} \\ P_\mu\xi\delta &= (P_\mu\xi\delta)_o + \Delta(P_\mu\xi\delta) \end{aligned} \tag{4.2}$$

The spectrum fit (Eq. 4.1) requires an estimation of the relative normalizations between the data spectrum, base spectrum and derivative spectra. The spectra are normalized by dividing the counts in the histogram by the total number of decay events in the fiducial. The uncertainty in histogram bin value due to the normalization is small compared to the uncertainty due to the count for all bins.

3. Blind Analysis

The entire analysis procedure, including evaluation of systematic uncertainties, can be completed while blinded to the values of the Monte Carlo input Michel parameters, ρ_o , η_o , $(P_\mu\xi)_o$ and $(P_\mu\xi\delta)_o$. The calculation of systematic uncertainties discussed in Sec. V depends on $\Delta\rho$ rather than ρ .

The TWIST Monte Carlo decay spectrum is generated by a separate program called “decay-gen”. Decay-gen randomly selects Michel parameters within an adjustable range centered about the current world averages. The allowed values for the 2002 analysis were:

$$\begin{aligned}
 |\rho_{PDG} - \rho_o| &\leq 0.02 \\
 |\eta_{PDG} - \eta_o| &\leq 0.10 \\
 |\delta_{PDG} - \delta_o| &\leq 0.03 \\
 |\xi_{PDG} - \xi_o| &\leq 0.02
 \end{aligned}
 \tag{4.3}$$

Decay-gen also requires the adopted values of ρ_o , η_o , ξ_o , δ_o to fall within the allowed ranges; e.g., $Q_R^\mu \geq 0$, and $\xi\delta/\rho \leq 1$.

The selected Michel parameters could only be extracted by a combination of two encryption keys. One of these encryption keys was written to two disks and otherwise deleted. The disks were retained in a secure location known only to a TRIUMF administrator not connected with TWIST.

B. Simulation

1. Chamber Response (GARFIELD)

Drift distance versus time tables are calculated with GARFIELD 7.08 simulations of the interactions in the drift chambers. GARFIELD inputs include gas type, temperature, pressure and chamber geometry. GARFIELD simulates ionization due to the positron, electron drift in the presence of electric and magnetic fields, charge collection at the sense wire and front end electronics (pre-amplifiers and discriminators). Signal timing and width are determined from the linear sum as a function of time of the charge arriving at the wire. The isochrones about a single drift chamber sense wire as calculated are shown in Fig. 18.

2. Detector and Event (GEANT)

As noted above in the analysis overview, event simulation is a critical component in the fitting of Michel parameters. Events in the TWIST detector are simulated using GEANT3 Monte Carlo. The TWIST Monte Carlo simulates the hardware, gases, particles, particle interactions and electronics in the TWIST detector.

Beam studies measurements were made without a solenoidal field (See Sec. 4). Using knowledge of the shape, position and divergence of the beam at $z = -154$ cm the beam was projected back to $z = -295$ cm. The resulting beam was input into the Monte Carlo detector and event simulation complete with the solenoidal field. Figure 19 shows the beam spot as measured in the TWIST detector in data and Monte Carlo. The simulated beam contains muons and positrons with rates as measured from M13 by the TWIST detector. Muons from pion decay in the beam are considered in the discussion of cloud muons and are accounted for in the polarization of the beam. Pions, themselves, are not simulated in the beam. An internal study

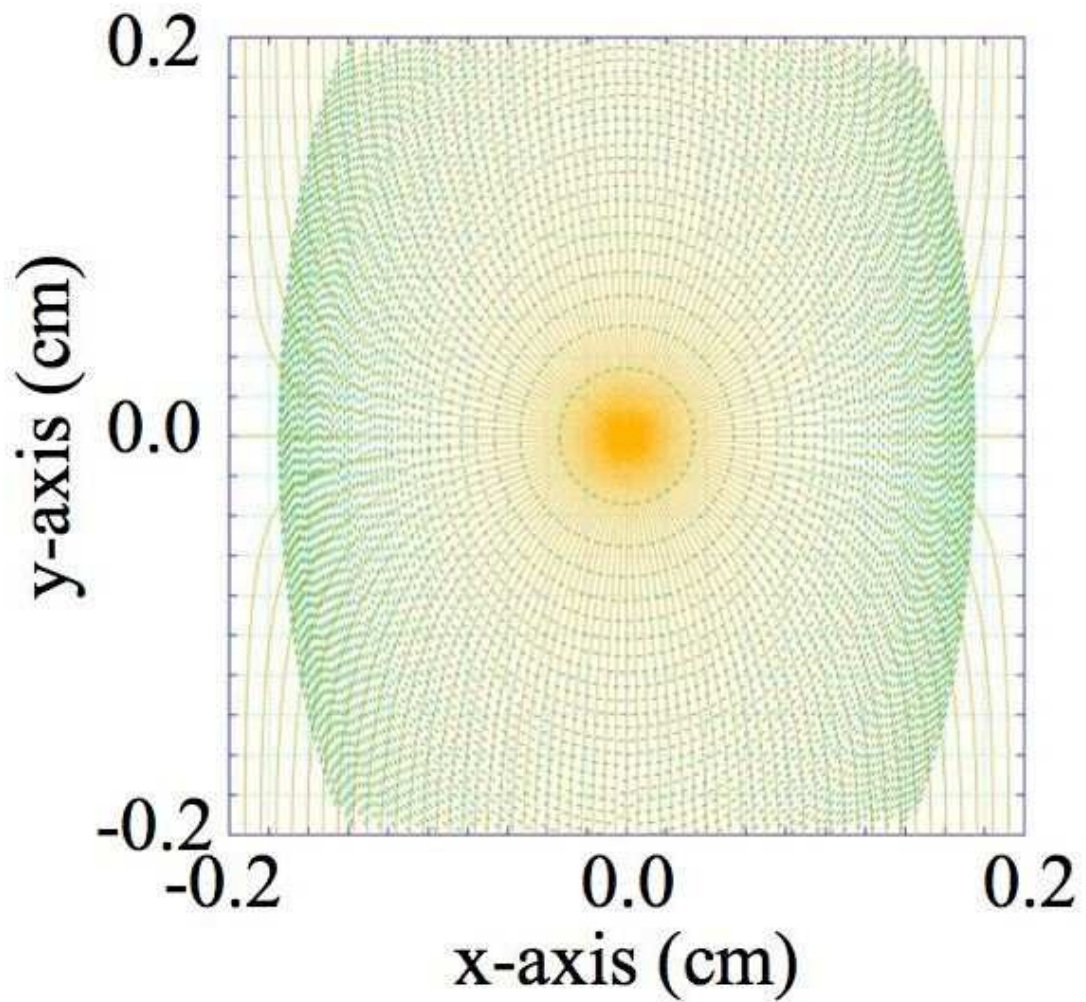


Fig. 18. Isochrones for drift chamber cell. GARFIELD calculated isochrones for DC wire cell in 2 T magnetic field at 297 K. Electron drift lines shown in solid gold. Isochrones shown is dashed green. Isochrone interval is $0.005 \mu\text{s}$.

has shown that the rate of positrons from pion decay within the TWIST detector is $< 10^{-5}$ times the rate from muon decay.

There are five types of Monte Carlo output falling into two broad categories:

1. data that mimics output from TDC's;
 - scintillator signals,
 - MWPC signals and
 - DC signals
2. and additional information that is optionally output;
 - particle kinematics (per hit) and
 - summary histograms (per run).

Simulation of the chamber response includes the effects of finite electron cluster formation along the track. The signals from the DC's simulate the real data in both timing and width. The signals from the MWPC's and scintillators match the real data in timing but have only vaguely realistic widths. The TWIST Monte Carlo does not simulate electronic cross talk.

C. Monte Carlo Accuracy

The TWIST measurements rely on the accuracy of the Monte Carlo simulation. Studies validating the Monte Carlo are used to quantify the accuracy. The results are used in the evaluation of systematic uncertainties that depend on the precision of the simulation. Studies include:

- Secondary particles and back-scattered positrons that subsequently enter the tracking volume,

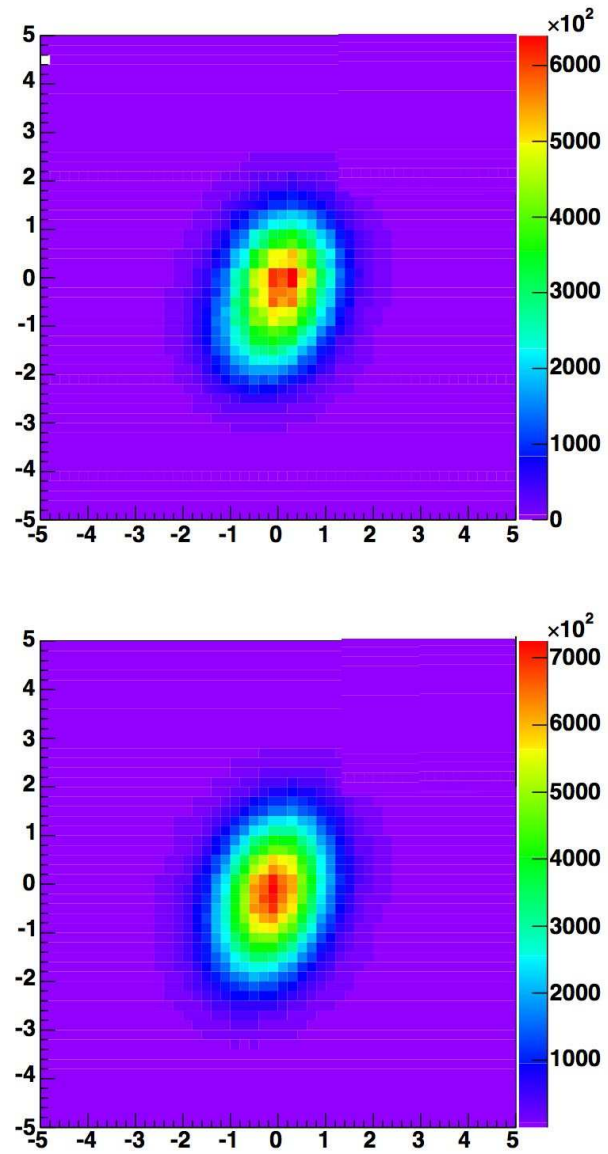


Fig. 19. Beam spot. v vs. u (cm). Top - data. Bottom - Monte Carlo.

- muon stopping distribution (stopping muon energy loss),
- event type rates,
- positron energy loss,
- positron multiple scattering,
- and simulation of long drift times in DC's.

Some of these studies lead directly to estimates of systematic uncertainties and are discussed in detail in Sec. V.

1. Positron Energy Loss and Multiple Scattering

Two studies contribute directly to the accuracy of the decay positron spectrum as a function of momentum and angle. The Monte Carlo simulation of positron energy loss and multiple scattering is validated in an analysis of the Dense Stack Stops set and a corresponding Monte Carlo Dense Stack Stops set. Positron tracks that traverse the entire detector were reconstructed for the upstream and downstream halves separately. The momentum difference between upstream and downstream tracks is a measure of the energy loss in the detector. Figures 20 and 21 show comparisons between data and Monte Carlo energy loss. A careful analysis of the integrated tails for momentum loss > 1 MeV/c (Fig. 20) revealed that the Monte Carlo differed from data by $\sim 14\%$. This difference includes contributions from the uncertainty in the thickness of the graphite layers on the mylar stopping target, in addition to those associated with the Monte Carlo simulation. The angle difference between upstream and downstream tracks is a measure of multiple scattering in the detector. The multiple scattering difference between data and Monte Carlo is of $O(1.5$

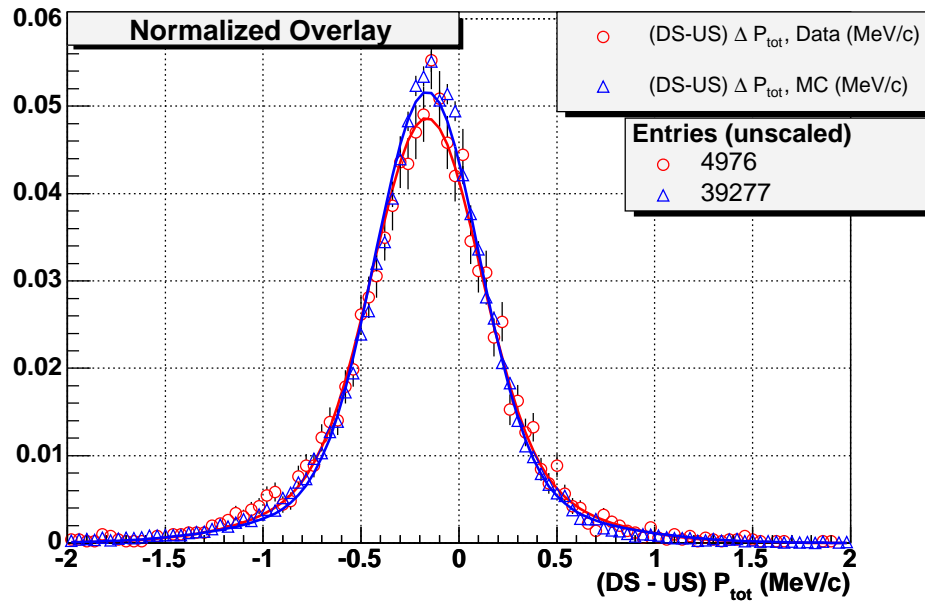


Fig. 20. Momentum loss in detector. Momentum difference (MeV/c) between upstream and downstream reconstruction of positrons. Red circles - data. Blue triangles - Monte Carlo.

mrad). Figure 22 shows comparisons of multiple scattering between data and Monte Carlo.

2. Muon Stopping Distribution

The muon stopping distribution was studied by comparing the Sparse Stack Stops set to a comparable Monte Carlo Sparse Stack Stops set. The comparison is shown in Fig. 23.

3. Event Type Rates

Relative event type rates are shown in Fig. 24 for both data and Monte Carlo.

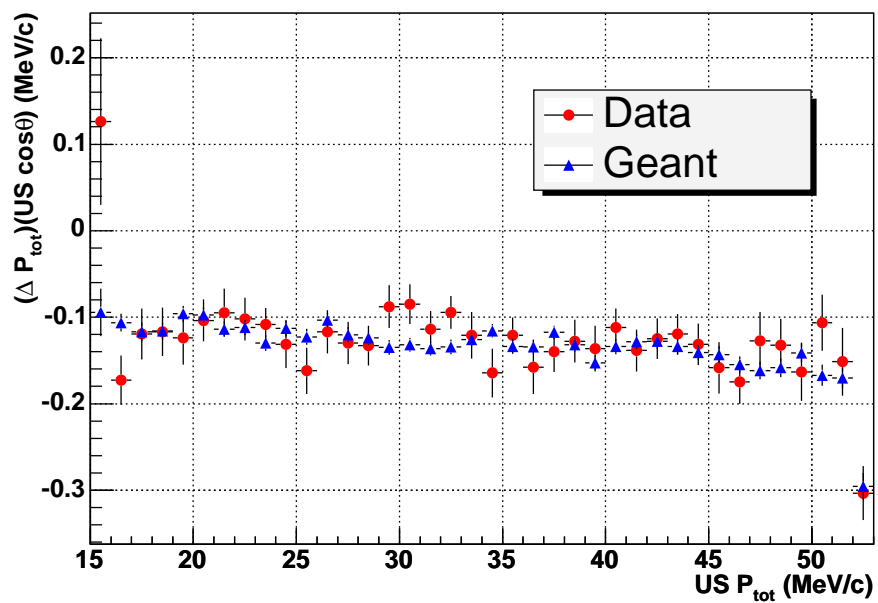


Fig. 21. Momentum loss times $\cos\theta$ vs. momentum. Momentum difference (MeV/c) between upstream and downstream reconstruction of positrons times $\cos\theta$ vs. momentum (MeV/c). Red circles - data. Blue triangles - Monte Carlo.

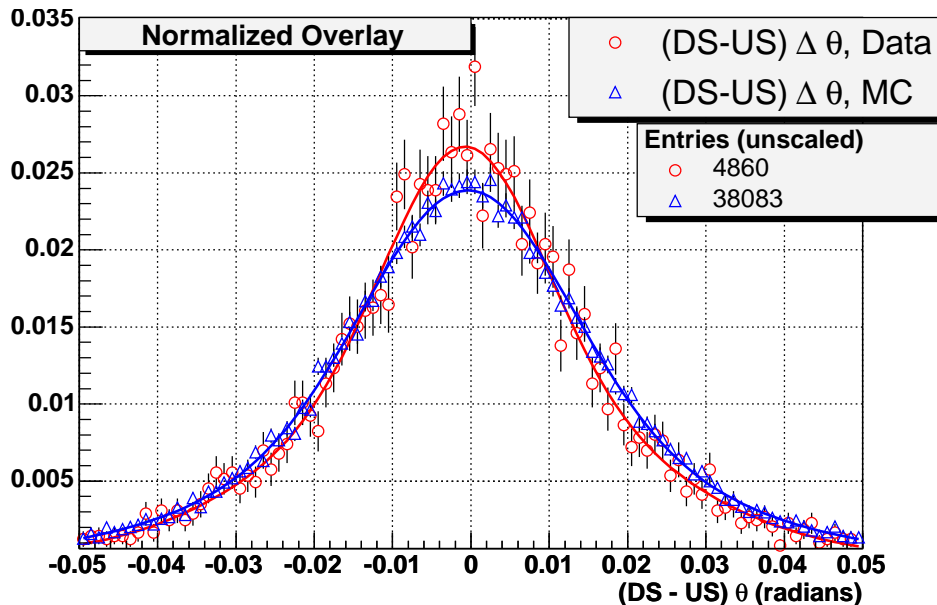


Fig. 22. Scattering in detector. Angle difference (rad) between upstream and downstream reconstruction of positrons. Red circles - data. Blue triangles - Monte Carlo.

D. MOFIA

The decay positron track reconstruction is accomplished by the program, MOFIA. MOFIA is constructed around a core program named KOFIA taken from the Brookhaven National Lab experiment E787 and heavily modified. The original KOFIA code was written in fortran 77, though some routines have been updated to fortran 90. Most of the analysis code, including all of the pattern recognition and fitting routines, has been written specifically for TWIST using fortran 90. The event display, providing a visual representation of each event, and the histogramming routines are written in C++ to accommodate the use of the ROOT graphics package. The analysis of a single event can be described in five steps:

1. temporal separation of hits,

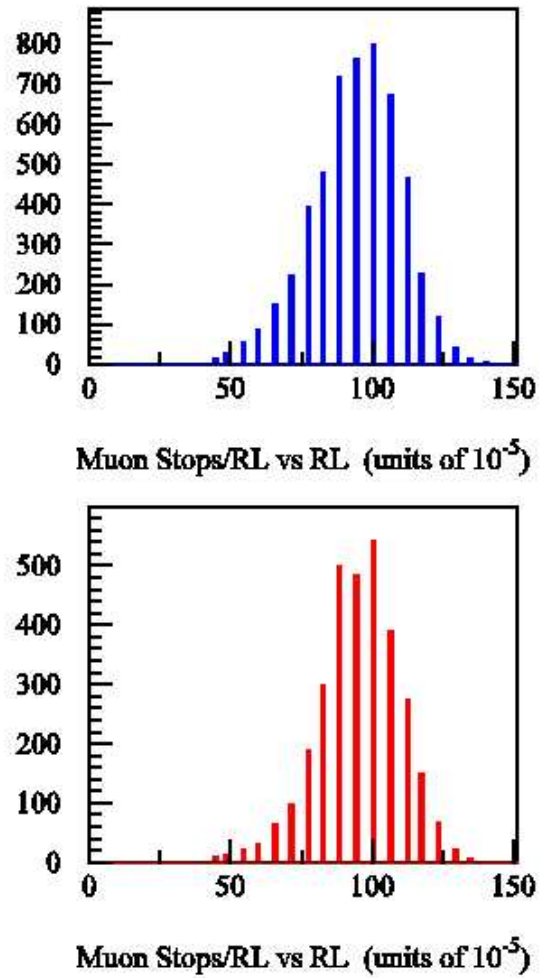


Fig. 23. Muon longitudinal stopping position. Top - data. Bottom - Monte Carlo.

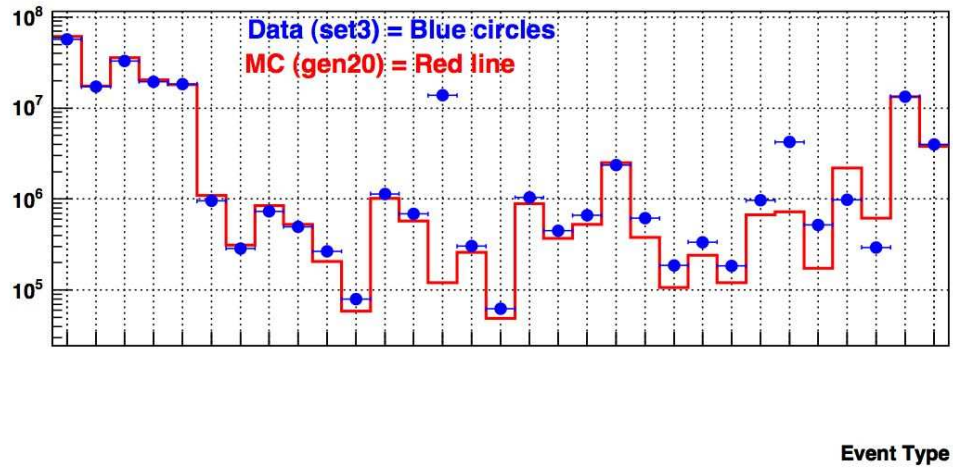


Fig. 24. Event classification rates, Monte Carlo vs. data. Bins are ordered consistent with event classification list described in Sec. 5.

2. particle identification,
3. event classification,
4. initial track estimate and
5. track fitting.

In addition to these analysis steps the unpacking of the data prior to analysis and the writing of the output are also handled by MOFIA and are discussed here.

1. Unpacking

MOFIA unpacking routines read data from the DAQ output files. In particular, signal timing and widths are read for hits from the scintillators, MWPC's and DC's, together with TDC error codes. Signal times are adjusted to account for electronic timing offsets utilizing t_o calibration files. The hit wires are recorded along with

the timing information. The hit wire positions are adjusted according to alignment correction files including translational and rotational corrections.

In addition, MOFIA can be run in a mode that identifies and removes electronic cross-talk hits. A hit is identified as a cross-talk hit if it produces a narrow signal within a short time interval after a good hit on a nearby wire. A good DC hit is defined as at least 50 ns wide and a good MWPC hit as at least 60 ns wide. The time interval searched for cross-talk is (5, 65) ns after a good DC hit and (5, 60) ns after a good MWPC hit. A DC hit is considered narrow if it is shorter than 50 ns and more than 60 ns shorter than the good hit. A MWPC hit is considered narrow if shorter than 40 ns and more than 60 ns shorter than the good hit. A nearby wire is defined as one within 10 wires of the good hit for DC's and within 32 wires of the good hit for MWPC's.

2. MOFIA Output

MOFIA produces four types of output files:

- log files that document all settings used in the analysis, any errors encountered and analysis summary statistics,
- histogram files containing summary histograms of raw data, initial track estimates and track fitting results,
- ROOT tree files that are discussed in significant detail below and
- skim files containing a subset of normal data files selected, based on criteria provided by the user. (The skim files were not produced by default and were only used for specialized studies such as those studying the effectiveness of fitting particular event types.)

In addition, event display routines provided event by event visualization. The event display was used extensively during data taking and code development to gain understanding of event type topologies and rates. A sample display is shown as Fig. 25.

TWIST utilized MOFIA in three ways:

1. as an on-line test of data quality during data collection,
2. for an on-line analysis of 1% of the data and
3. for the offline analysis of all data.

The on-line quality of data (QOD) analysis excluded the fitting of tracks and the subsequent production of the ROOT trees. In their place, the QOD code included routines that compared raw data histograms to a set of nominal histograms utilizing a Kolmogorov test. Significant differences were flagged and the relevant histograms were made available for the experimenter on shift to examine.

3. Time Separation

Hits can be separated temporally using both MWPC's and DC's. The MWPC's with drift times of 10's of ns separate all non-coincident particles on the scale of the muon lifetime ($2.2 \mu\text{s}$). The DC's with drift times of 100's of ns can clearly distinguish particles more than $1 \mu\text{s}$ apart in the detector. Events with particle separations greater than 1050 ns, designated clean events, are fully analyzed. Events with particle separations between 200 ns and 1050 ns, designated overlap events, are excluded from further analysis on the grounds that it is more difficult to correctly assign hits to the particles if they overlap in z . Because the second particle is uncorrelated to the decay positron, this cut is independent of the positron momentum and angle. Events with

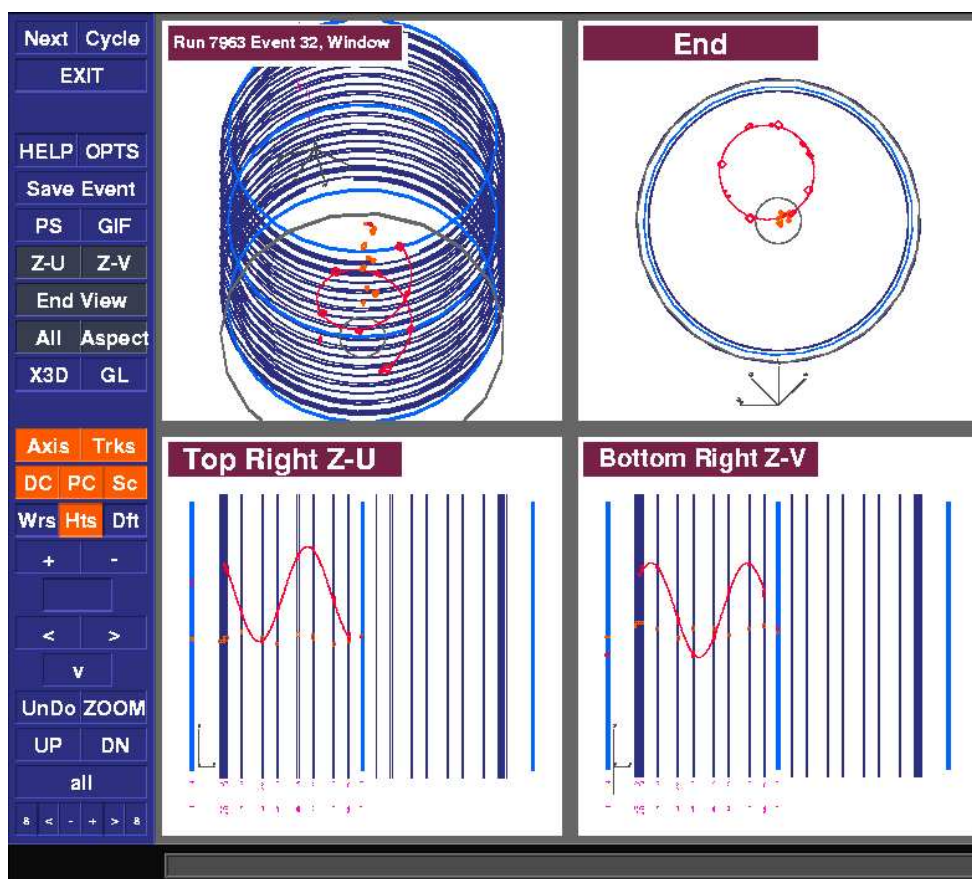


Fig. 25. Event display of upstream decay. Display from Nominal A event. Helix is reconstructed decay positron track. Marks at the bottom of “Z-U” and “Z-V” panels illustrate timing of hits on each plane with later times towards the bottom. Note two distinct lines of marks in each panel. The top line comes from the muon. The bottom line comes from the decay positron.

coincident or nearly coincident particles cannot be distinguished from clean events on the basis of timing and are included in the full analysis. Coincident particles may be correlated with the decay positron and thus it is necessary to fully analyze such events.

Hits are separated into “time windows” by grouping MWPC hits clustered in time. The earliest MWPC hit in a group defines the time limits of the window. The beginning of the window is set to 50 ns prior to the first MWPC hit to allow for the drift time of the MWPC’s. The end of the window is set to 1 μ s after the first MWPC hit to allow for the drift time of the DC’s. Time windows can either be separated in time or overlapping. Some examples are illustrated in Fig. 26.

4. Particle Identification

Once all windows in an event have been created they are classified in chronological order from first to last considering the spatial distribution of both MWPC and DC hits within the window. Window classifications are listed in Table XII.

If two windows overlap there is an interval of time for which DC hits cannot be assigned unambiguously using only timing information. If such a case involves a decay positron window, any hit that could possibly belong to that positron is assigned to that window, where “possibly belonging” means that the hit is within the time limits of the window and occurs in the appropriate half of the detector (see Fig. 26, example 2).

5. Event Classification

An event is classified based on the type and order of windows contained. Event classifications are:

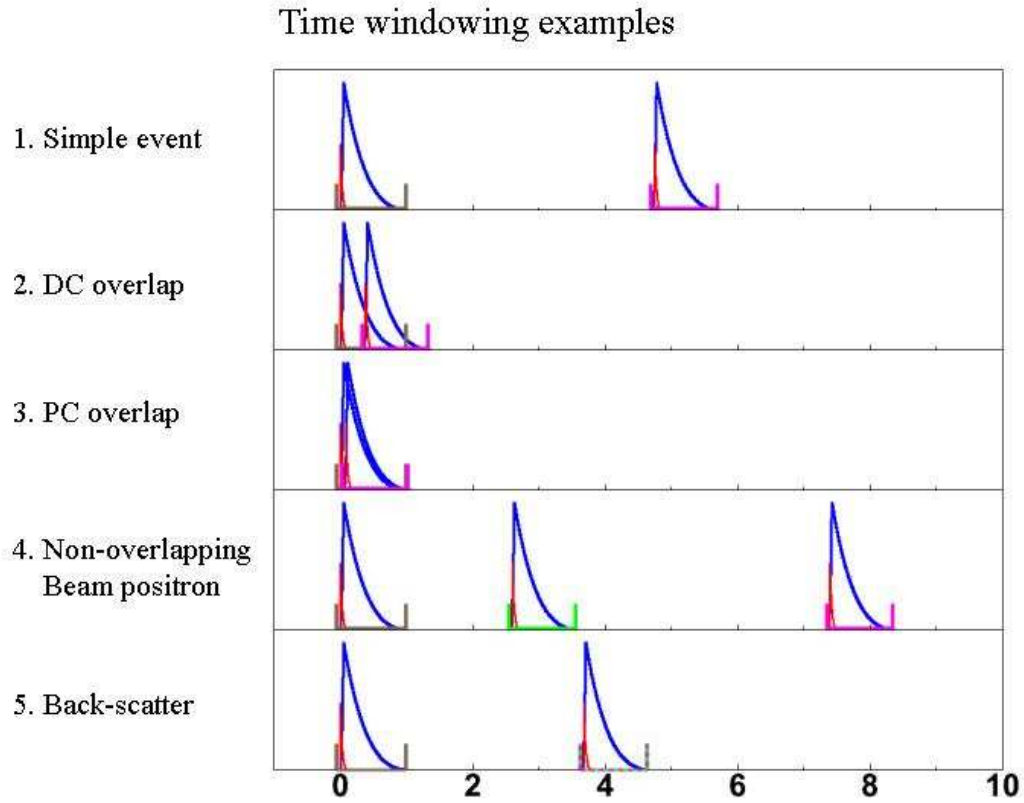


Fig. 26. Time window schematic. Red lines represent MWPC distributions for each particle. Blue lines represent DC distributions. Brackets represent resulting time windows. The back-scattering event contains only two time windows because the positron's initial track and backscattered track are indistinguishable in time. The time difference for the two tracks is small compared to the drift time of the MWPC's.

Table XII. Time window classifications.

Time window classification
1. Muon
2. Upstream decay
3. Downstream decay
4. Beam positron
5. Empty
6. Overlap of non-muons; no previous muon
7. Upstream decay plus delta
8. Downstream decay plus delta
9. Upstream decay plus back-scatter
10. Downstream decay plus back-scatter
11. Muon and fast downstream decay
12. Muon and fast upstream decay
13. Muon plus beam positron
14. Upstream decay plus beam positron
15. Downstream decay plus beam positron
16. Soft track uncorrelated to other particles
17. Cosmic
18. Overlaps beginning of event gate
19. Overlaps end of event gate
20. Decay from muon prior to event gate
21. Pion

1. Muon and decay
2. Muon, decay and beam positron
3. DC overlap of muon & decay
4. DC overlap of muon & decay; non-overlapping beam positron
5. PC overlap of two particles
6. Muon and decay plus delta
7. Muon, decay plus delta and beam positron
8. DC overlap of muon & decay plus delta
9. DC overlap of muon & decay plus delta; non-overlapping beam positron
10. Muon and decay plus back-scatter
11. Muon and decay plus back-scatter; non-overlapping beam positron
12. DC overlap of muon & decay plus back-scatter
13. DC overlap of muon & decay plus back-scatter; non-overlapping beam positron
14. Beam positron trigger
15. Multiple muons and their decays
16. Multiple muons, their decays and beam positron
17. Multiple muons and their decays; at least one DC overlap
18. Multiple muons. their decays and beam positron; at least one DC overlap
19. Multiple muon decays, muon-positron correlations ambiguous

20. Muon without decay
21. Muon and DC overlap of decay and beam positron
22. Muon, beam positron and DC overlap of decay & additional beam positron
23. DC overlaps of muon & decay & beam positron
24. DC overlaps of muon & decay & beam positron; additional beam positron
25. Unknown trigger; no muons or decays
26. Unknown trigger; at least one muon or decay
27. Miscellaneous
- 28., 29. Too few hits
- 30., 31. Decay with too high of angle

A sampling of event types is shown in Figs. 25 and 27-30.

It is important that the event classification correctly distinguish between time overlap and non-overlap events. Likewise, it is critical that non-overlapping events in time are correctly sorted into those that are fully analyzed and those that can be excluded from analysis in an unbiased way.

Monte Carlo studies have been undertaken to evaluate these two issues. For the studies, events were classified twice, once using the standard analysis routines and once using the precise knowledge of the particles internal to the Monte Carlo. The classifications were compared on an event by event basis.

In addition, a calculation of the muon lifetime has been performed based on time window differences for event classifications 1, 6, 10 and 21. The lifetime fit is a test of the particle identification and event classification. The fit was performed for

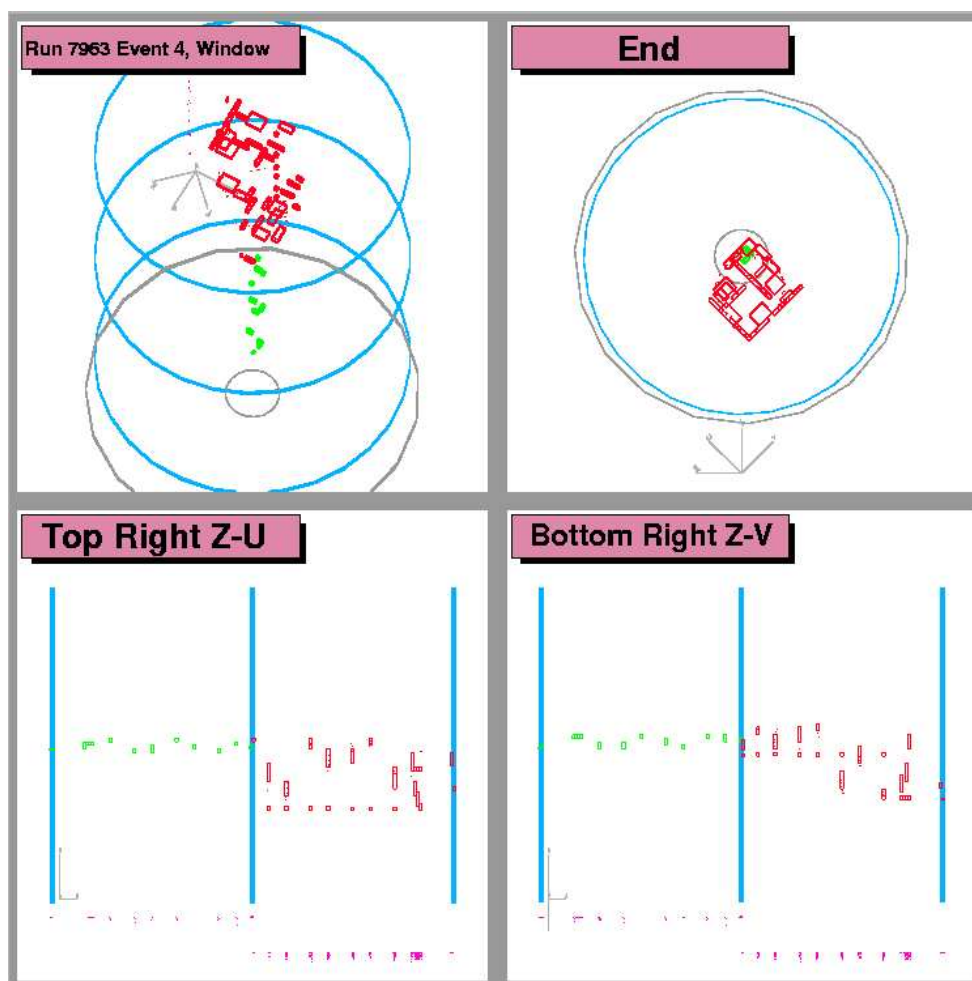


Fig. 27. Downstream decay plus delta. The track was fit successfully, but fit is not shown in this figure.

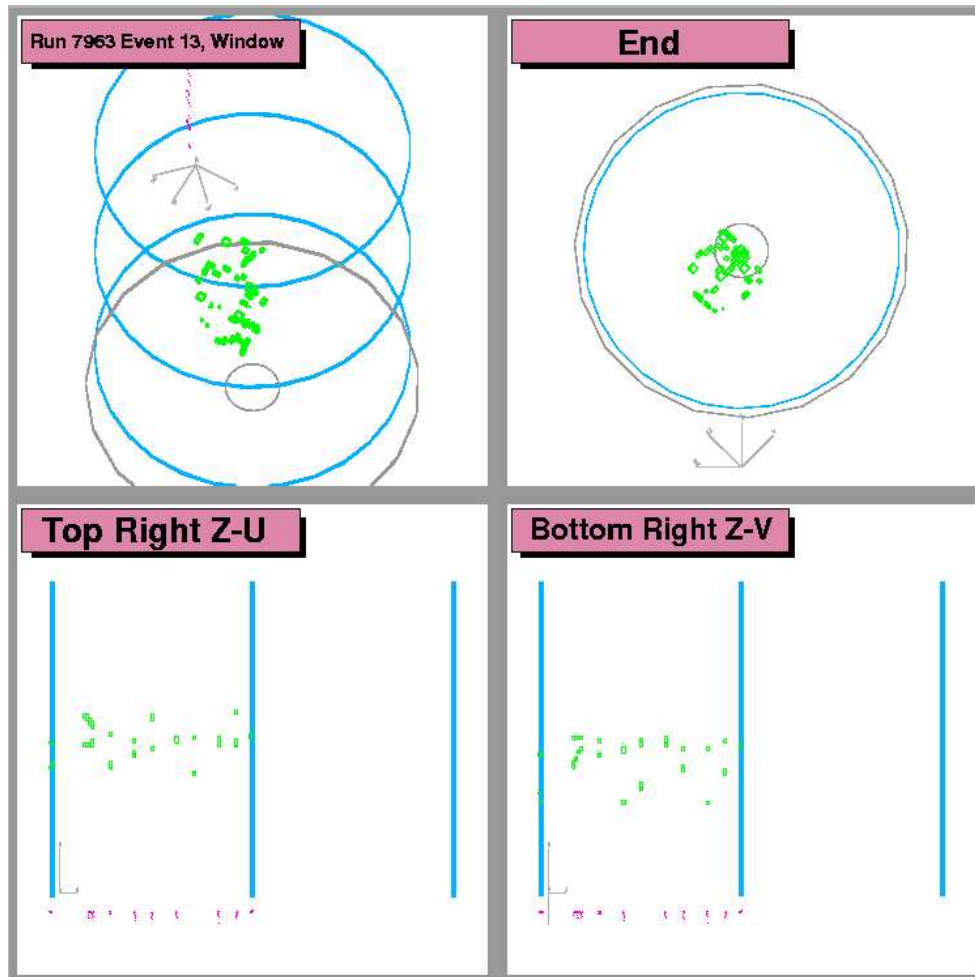


Fig. 28. Upstream fast decay. The track was fit successfully, but fit is not shown in this figure.

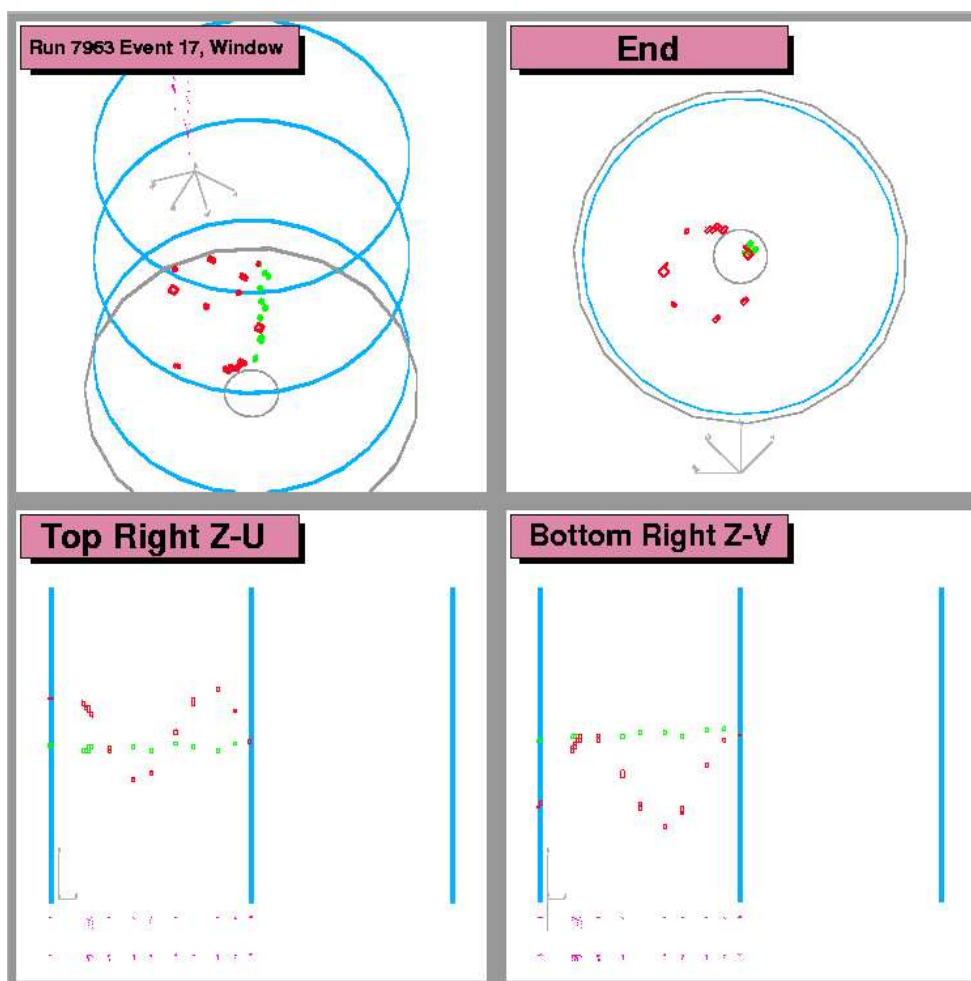


Fig. 29. Upstream decay. The track was fit successfully, but fit is not shown in this figure.

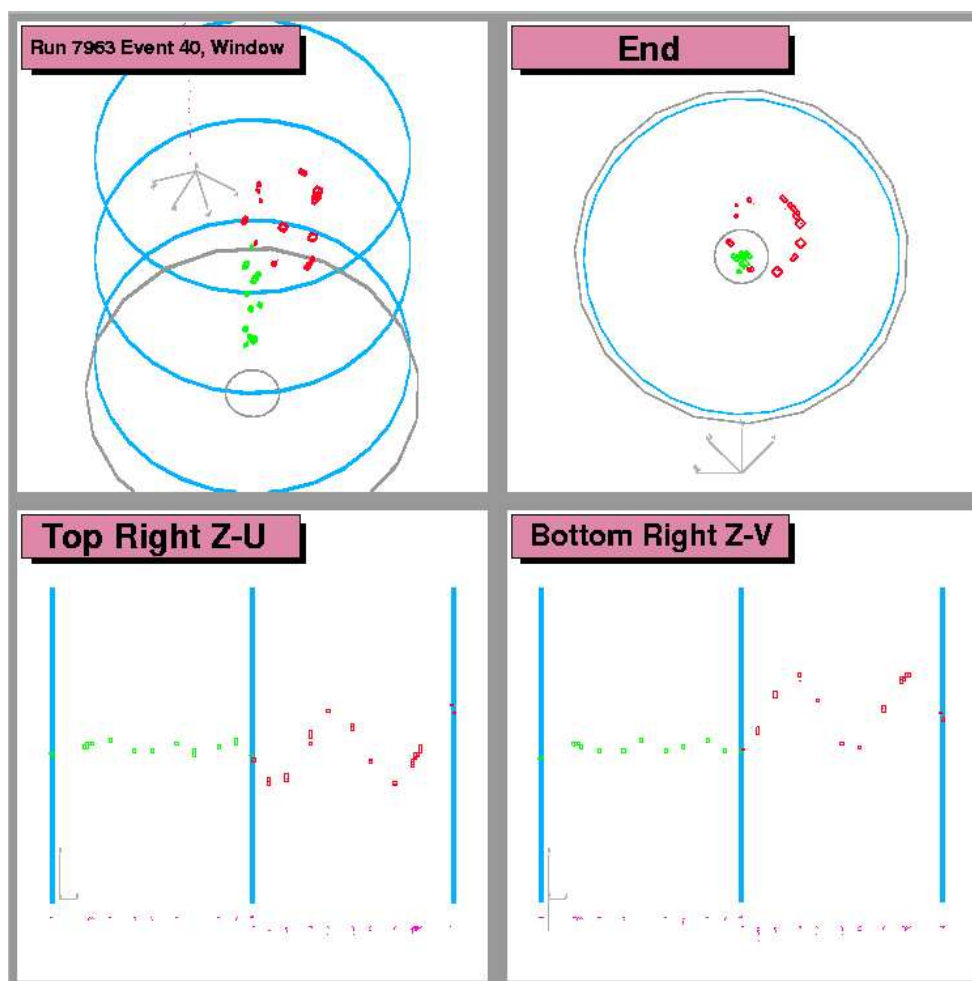


Fig. 30. Downstream decay. The track was fit successfully, but fit is not shown in this figure.

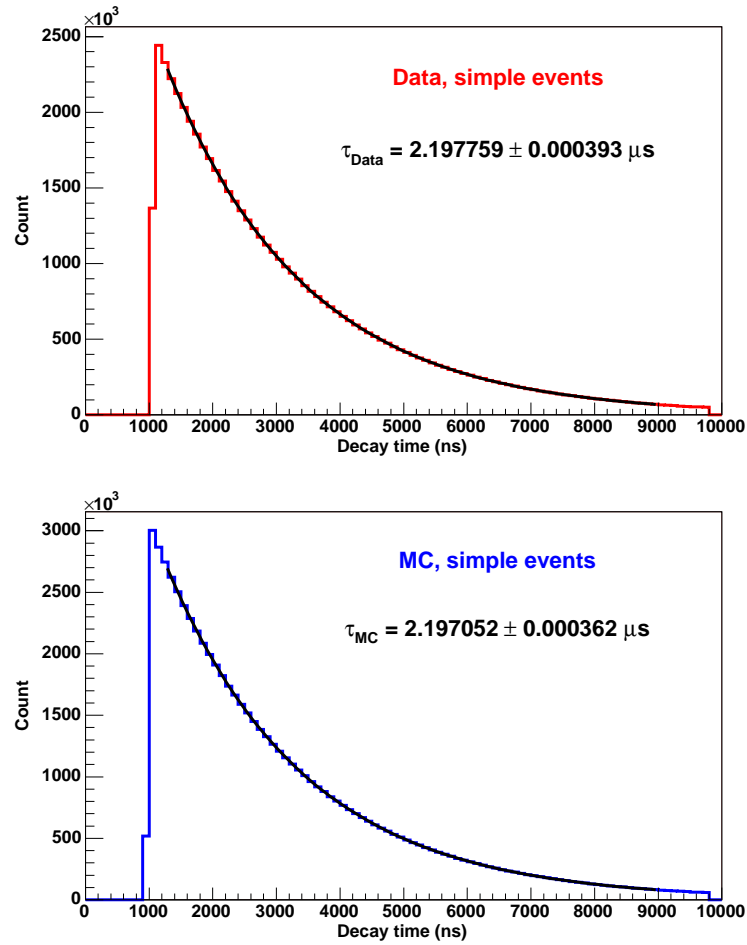


Fig. 31. Muon lifetime. Lifetime calculated from TWIST decay time spectrum for event classifications 1, 6, 10 and 21. Only statistical uncertainties are given.

both data and Monte Carlo providing an additional consistency check of the event simulation. The fits yielding $\tau_{\text{Data}} = 2.1978 \pm 0.0004(\text{stat})$ and $\tau_{\text{Monte Carlo}} = 2.1971 \pm 0.0004(\text{stat})$ are shown in Fig. 31. Systematic uncertainties were not evaluated for the lifetime fit.

6. Spatial Hit Clustering

Particles passing through chambers often produce signals on multiple wires. The number of wires hit is a function of crossing position, angle and energy deposition. For a positron, the transverse position at the z of a chamber is estimated by calculating the average position of all hit wires within the chamber. θ , the angle of a positron track relative to the z -axis, is correlated with the average number of wires hit per chamber. For this reason, it is convenient to create spatial clusters of contiguous hits within each chamber for each time window. Furthermore, clusters from adjacent orthogonal chambers are combined to create clusters in both u and v at the average z of the two chambers. Hit clustering is illustrated in Fig. 32, including the ambiguity resulting from multiple particles overlapping in time.

7. Initial Track Estimate

Providing an initial estimate of a helical particle track is achieved in two steps. The first is to estimate the projection of the helix onto the transverse plane, this projection being a circle. The second is to calculate the phase of the helix as a function of longitudinal position.

The circle estimate is chosen from parameterizations derived from all combinations of three hit clusters. The χ^2 is calculated for each possibility using all hit clusters. The parameterization yielding the smallest χ^2 is selected as the circle estimate.

The phase of the helix can be expressed as

$$\phi_i = \omega(z_i - z_o) + \phi_o \quad (4.4)$$

where ϕ_o is the initial phase at $z = z_o$. ϕ at the z location of a foil between two

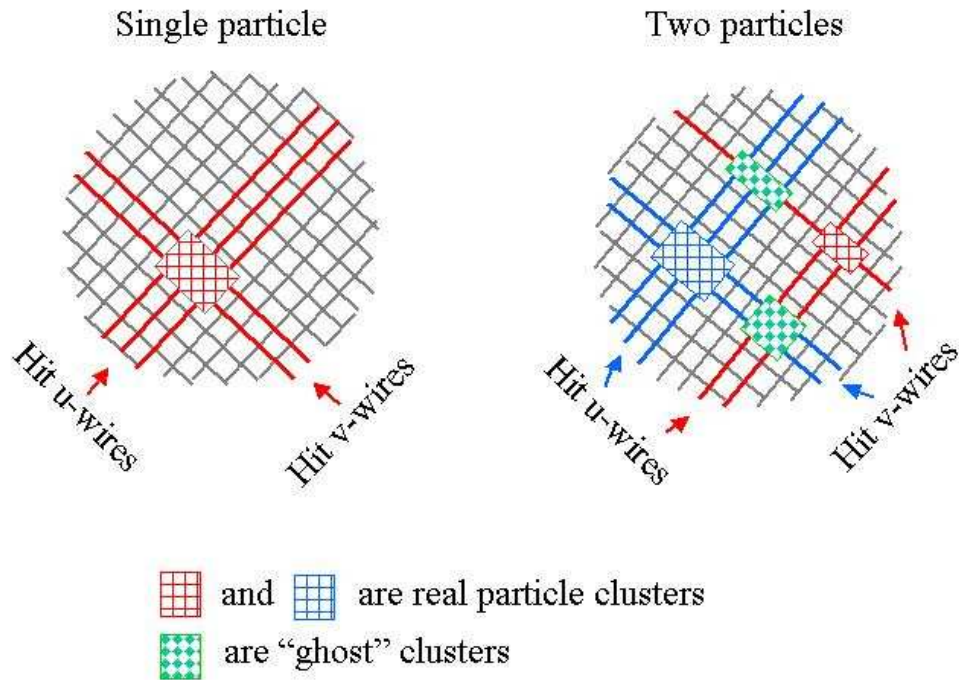


Fig. 32. Hit clusters. Two dimensional clusters created from hit wires within a pair of orthogonal chambers. A cluster is characterized by its location in (u,v) and its size. The image on the right illustrates the ambiguity in clustering resulting from two time coincident particles. Two of the clusters come from combining u hits from one particle with v hits from the other particle. In this configuration two of the clusters opposite of each other are real and two are false combinations, labeled “ghost” clusters.

adjacent orthogonal planes can be estimated by calculating the angle between the u -axis and a ray from (u_c, v_c) through u and v as measured at the two planes.

$$\phi_i^{\text{calc}} = \tan^{-1} \left(\frac{v_i - v_c}{u_i - u_c} \right) \quad (4.5)$$

The phase as a function of $z \bmod 2\pi$ is equivalent to the calculated phase.

$$\phi_i = \phi_i^{\text{calc}} + 2\pi n_i \quad n_i \in \mathbf{I} \quad (4.6)$$

Though, mathematically, there are an infinite number of possible combinations of n_i , there are several restrictions that drastically limit the reasonable combinations:

1. The longitudinal frequency, ω , of the track is correlated with the number of cells hit within a plane.
2. One n_i can be chosen arbitrarily.
3. Once any n_j and n_k , $k \neq j$, have been chosen, all other n_i are limited to at most two possibilities.
4. The vast majority of tracks do not wind through a phase change of 2π between successive pairs in the dense stack.
 - Those that wind more than 2π in the dense stack leave a clear signal in the number of cells hit relative to the radius.
 - Those that wind more than 2π in the dense stack are far from the detector acceptance in θ .

The approach used is a combinatorial approach beginning with the most likely candidate:

1. Fix $\phi_i = \phi_i^{\text{calc}}$ for one specific $i = j$.

2. Fix a second $\phi_i = \phi_i^{\text{calc}} + 2\pi n_i$, for $i = k$, $k \neq j$ and z_k is “far” from z_j (z_k and z_j are near opposite ends of the track) utilizing the relationship between ω and the average number of cells hit per plane.
3. Fix all remaining ϕ_i by minimizing

$$\left| \phi_i - \left[\frac{\phi_k - \phi_j}{z_k - z_j} \right] (z_i - z_j) - \phi_j \right| \quad (4.7)$$

4. Given $z_o = (z_j + z_k)/2$, fit for ω and ϕ_o .
5. Repeat steps 2-4 replacing n_k with the values $-n_k$, $n_k + 1$, $n_k - 1$, $-n_k - 1$, $-n_k + 1$, ..., 50, -50, 1, -1, 0.
6. Repeat steps 1-5 selecting two more combinations of j and k .
7. The process is continued until an acceptable estimate is found or all allowed values have been tried.

Estimate acceptability is determined by evaluating a Chebyshev Norm defined as $\sum \Delta\Phi_i$ where $\Delta\Phi_i$ is the difference between the angle as predicted by the track estimate, ϕ_i^{pred} , and the angle as calculated from the cluster of hit cells, ϕ_i^{calc} , including an accounting for the uncertainty due to the cluster size.

$$\Delta\Phi_i = \begin{cases} 0 & \text{if } \phi_i^{\text{pred}} \in [h_{\text{cl}}^-, h_{\text{cl}}^+] \\ \min [|\phi_i^{\text{pred}} - h_{\text{cl}}^-|, |\phi_i^{\text{pred}} - h_{\text{cl}}^+|] & \text{otherwise} \end{cases}$$

where $h_{\text{cl}}^\pm = \phi_i^{\text{calc}} \pm (\text{cluster width in } \phi)/2$. A track estimate is deemed acceptable if $\sum \Delta\Phi_i = 0$.

8. Track Fitting

Track fitting is accomplished via a succession of two applications of χ^2 minimization routines, once using only drift plane wire positions and once using full drift distance versus time relationships. The fitting parameters include the set from the initial track estimate, u_c , v_c , R , ω and ϕ_o . In addition, the fitter allows for kinks due to multiple scattering. Each kink is parameterized by $\Delta\theta_u$ and $\Delta\theta_v$. A maximum of seven kinks are allowed depending on the location and extent of a given track. Six allowed kink locations are in the DC sparse stack at the z of the central cathode foil of each pair, excluding the pair nearest the stopping target, and one allowed location is in the DC dense stack. There is no explicit limit on the magnitude of a kink. Kink sizes are limited by the ability of the initial track estimation to assign hits in the presence of a scatter. A particle trajectory with an excessively large scatter may be fit as two tracks. Both χ^2 fits minimize

$$\chi^2 = \sum (d_{\text{track}} - d_{\text{hit}})^2 / \sigma_d^2 + \sum \theta_{\text{kink}}^2 / \sigma_{\text{kink}}^2 \quad (4.8)$$

where $d_{\text{track}} = f(\text{fit parameters}, z)$ integrates $\vec{F} = q\vec{v} \times \vec{B}$ using an arc step approximation with variable step size. During the wire center fit any hit more than 3 cm from the track is excluded.

The second χ^2 fit utilizing drift times includes decay time as a fit parameter. The inclusion of drift times introduces an ambiguity in hit position. The distance of each hit from the wire is calculated, but not the direction. The ambiguity is removed when multiple wire cells are hit in a single plane. Ambiguities resulting from planes with a single hit are resolved with an annealing type algorithm. The hit side of the wire is initially chosen to match the track side. Any hits farther from the wire than a given threshold are fixed to their current side. The fit is then re-calculated. After

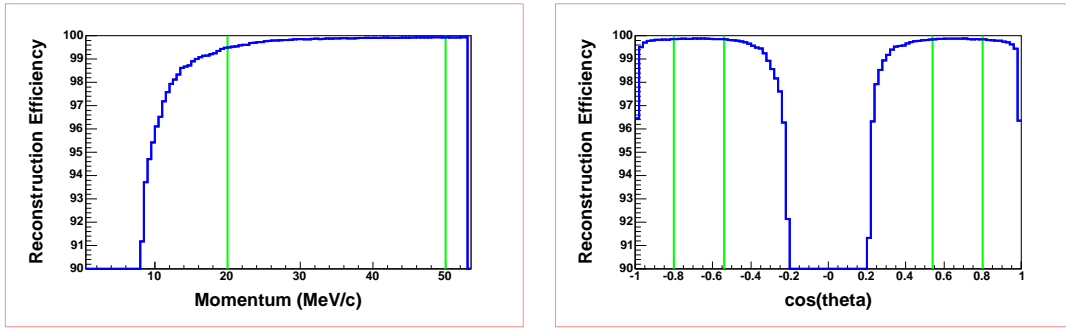


Fig. 33. Reconstruction efficiency. Reconstruction efficiency for positrons well separated in time from other particles as determined from reconstruction of Monte Carlo set. A successful fit is defined as one in which the reconstructed track has momentum within 3 MeV/c and $\cos\theta$ within 0.1 of true values taken directly from the Monte Carlo. Left - as a function of momentum. Right - as a function of $\cos\theta$.

each iteration the threshold is reduced until all ambiguities are resolved.

The time residuals have non-Gaussian tails and the χ^2 fit uses a constant $\sigma_t = 100$ ns, with the result that the χ^2 from the final fitter is not a good estimator of fit quality. This could be addressed by using maximum likelihood fits and by using cell position dependent time uncertainties, but this was not done for this analysis.

The combined success of the initial estimate and the fitter is shown for positrons well separated in time from other particles in Fig. 33. The reconstruction efficiency is above 99% for decay positrons within the fiducial without additional particles.

E. Root Tree Analysis

The ROOT trees output by MOFIA contain variables used for cuts as well as the momentum and decay angle of the decay positrons. The trees are analyzed by ROOT macros written in C++. The purpose of the tree analysis is to produce a spectrum in momentum and $\cos\theta$ from decay positrons passing all non-fiducial cuts, where fiducial cuts are defined relative to the momentum and $\cos\theta$ of the decay positron. The

ROOT tree analysis consists of up to three stages; the application of event cuts, the application of track cuts and the selection of a decay track out of multiple choices. Two separate ROOT tree analysis packages have been used and are designated algorithm \mathbb{A} and algorithm \mathbb{B} . The algorithms differ in the treatment of tracks that scatter in the target or detector materials and in the selection of one track among multiple choices. Cuts that are common to both algorithms may have different designations in the code and in the associated figures. In such cases, both designations are given in the cut description. Figure 34 shows counts of events rejected by each cut for both data and Monte Carlo using algorithm \mathbb{A} . Figure 35 gives the corresponding histograms for algorithm \mathbb{B} .

1. Event Cuts

An event must pass the following six event cuts to have an associated decay positron track considered for inclusion in the fit spectrum.

1. TCAP: The muon time relative to the beam cycle must be in the interval $[-40, -10]$ ns for surface muon sets and $[-41, -31]$ ns for cloud muon sets. This cut avoids the inclusion of pions and selects particular ratios of (surface muons)/(cloud muons) and muons/positrons. This cut is not applied to Monte Carlo sets since the Monte Carlo sets have the (surface muons)/(cloud muons) and muons/positrons ratios tuned to match the data with this cut applied.
2. m12width: The width of the muon trigger signal must be in the interval $[0, 20000]$ ns. The range for this cut was set large to effectively remove the cut, however, a significant fraction of Monte Carlo events were excluded based on this cut. The purpose of the cut is to remove events that triggered on a particle other than a muon. The Monte Carlo events triggered on a muon by definition

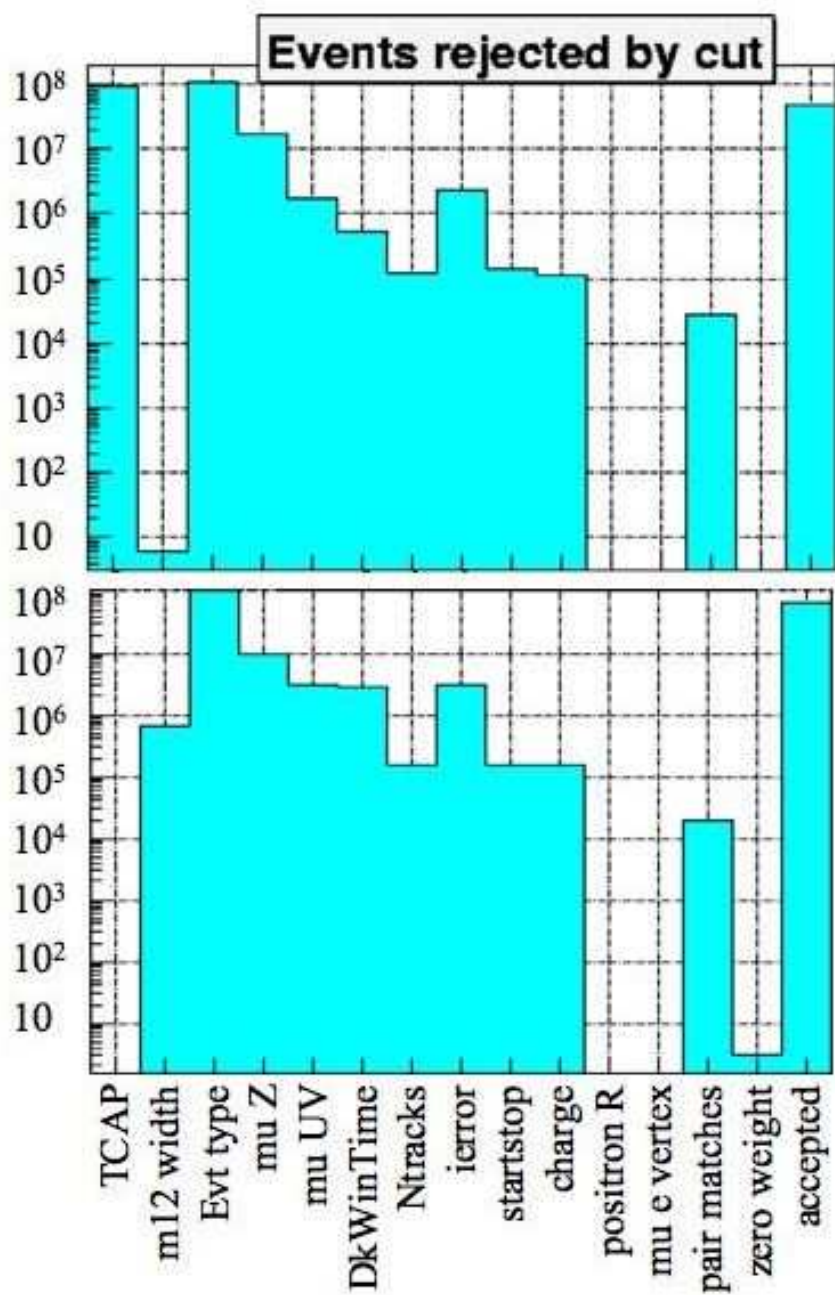


Fig. 34. Algorithm A event cuts. Events rejected by each cut using algorithm A . Top - Applied to Nominal B. Bottom - Applied to Monte Carlo set. (Some cuts were turned off for this analysis and are not discussed in the text.)

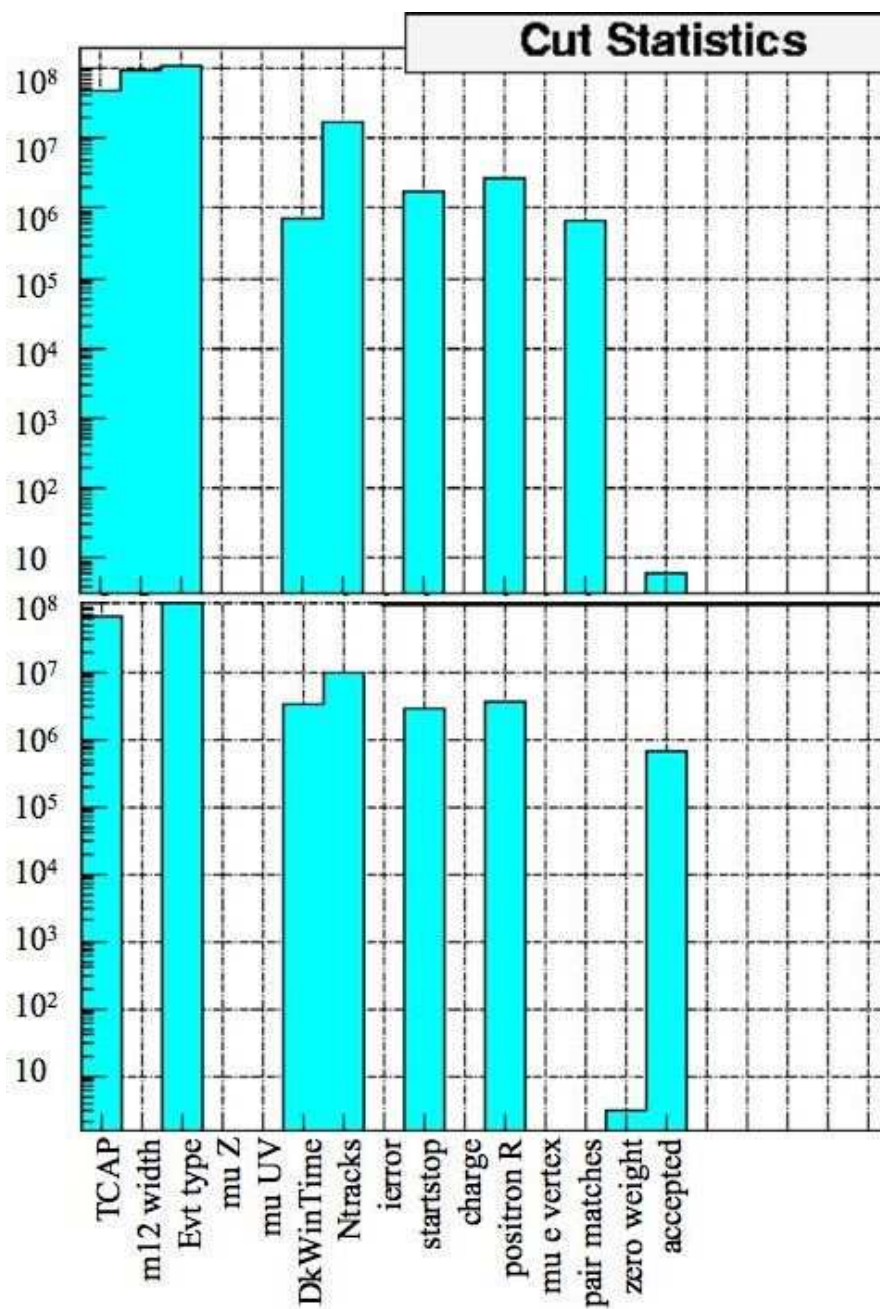


Fig. 35. Algorithm \mathbb{B} event cuts. Events rejected by each cut using algorithm \mathbb{B} . Top - Applied to Nominal B. Bottom - Applied to Monte Carlo set. (Some cuts were turned off for this analysis and are not discussed in the text.)

and the subsequent decay positron spectrum is uncorrelated to the simulation of the muon trigger signal width.

3. Evt type or EvType: The event type according to the event classification must be 1, 2, 6, 7, 10, 11, 21 or 22. This cut excludes event types that have complications uncorrelated with the decay positron or the rates of correlated complications are negligible.
4. mu Z or MuonLastPC6: The farthest downstream hit recorded by the muon must be in the MWPC just upstream of the stopping target. This cuts ensures that the muon stopped either in the stopping target or in the gas of the MWPC just upstream of the stopping target.
5. mu UV or MuonRadius: The muon's transverse stopping position, (u, v) , must be within 2.5 cm of the origin in the center of the stopping target. This cut in combination with a fiducial cut on the transverse momentum of the decay positron avoids the inclusion of positrons that hit the support structure outside of the active tracking region in the radial direction.
6. DkWinTime or DecayTime: The decay time must be in the interval $[1.05, 9.0] \mu\text{s}$. This cut avoids the inclusion of fast decays. Fast decays produce an upstream-downstream asymmetry as fast upstream decay hits are indistinguishable from the muon hits, whereas fast downstream decay hits clearly belong to the positron. In addition, this cut avoids the inclusion of late decays. Decay positron time windows for decay times greater than $9 \mu\text{s}$ overlap the end of the gate during which signals are collected. Long drift time hits for such decays are lost.
7. Zero Weight: This cut rejects a particular type of incomplete Monte Carlo event

that can occur if the last event of a run is a multiple muon event and the Monte Carlo decay sample is exhausted prior to the last decay.

2. Track Cuts

If an event has passed all event cuts then each track within the decay positron time window is subjected to a set of four track cuts. Algorithm \mathbb{B} combines these cuts into a single cut designated “NoFit”. The descriptions of these cuts are labeled below with the algorithm \mathbb{A} designations.

1. Ntracks: There must be at least one track in the decay positron time window.
2. ierror: The track must have passed the track fitting without errors.
3. startstop: The entire track must lie in the appropriate half of the detector according to the event classification.
4. charge: The track helicity must correspond to a positively charged particle moving away from the stopping target.

In addition to these common cuts, algorithm \mathbb{A} requires that the (u, v) position of the decay positron track projected to the stopping target is within 0.5 cm of the muon stopping position.

3. Track Selection

In 2.3% of the events multiple tracks exist within the decay positron time window. Multiple tracks can be the result of multiple particles, either correlated or uncorrelated with the decay positron, or from single particles that produce multiple distinct tracks. Uncorrelated tracks are generally due to beam particles in time coincidence with the decay positron. Correlated particles are due to the production by the decay positron

of secondary particles such as delta rays. Multiple tracks from a single particle can occur when a particle experiences a sufficiently hard scatter such that a single helix will not fit the hits before and after the scatter. In such cases, the analysis routines fit tracks that are hard scatter-free segments of the full particle path. Multiple tracks can also arise when a particle traverses both halves of the detector, as the analysis fits upstream and downstream halves separately creating two tracks.

4. Algorithm A

Algorithm A uses two stages to select among multiple tracks. The first stage identifies multiple tracks from a single particle and removes tracks based on the full particle path. The second stage chooses between multiple tracks that remain.

The first stage labels two tracks as belonging to the same particle if the tracks do not overlap in z and have a closest distance of approach less than 0.5 cm. If two such tracks from a single particle lie in opposite halves of the detector, the previously allowed track is rejected on the grounds that it is either a beam particle, a secondary particle or the back-scattered portion of a decay positron trajectory. (Note that the track from the detector half opposite to the decay has been previously cut, but is used to identify the remaining portion of the trajectory.) If two tracks from a single particle lie in the appropriate detector half, the one farthest from the target is rejected on the grounds that it represents the decay positron trajectory after a hard scatter. If at least one track remains after stage one, the track(s) have passed the “pair matches” cut.

If a single track remains, it is selected for inclusion in the decay positron spectrum. If multiple tracks remain, stage two selects between the tracks by opting for the track with the least distance between a hit DC and the stopping target. In the case that the closest DC hit for each track is in the same DC, the tracks are compared

based on their match to the muon stopping position. The tracks are extrapolated to the stopping target and the track coming closest to the muon stopping position is selected.

5. Algorithm \mathbb{B}

Algorithm \mathbb{B} includes three steps.

If multiple tracks are non-overlapping in z , the track closest to the stopping target is kept and the other non-overlapping tracks are rejected.

If multiple tracks still remain (tracks overlapping in z) and a single track exists in the opposite detector half then an attempt is made to match tracks to the track from the opposite half. Any track that has momentum within 1 MeV/c and θ within 1 mrad of the track from the opposite half is rejected.

If multiple tracks still exist, the track with the highest momentum is selected.

F. Momentum Calibration

The momentum of the decay positron is extracted from the reconstructed helical track. The transverse momentum is $p_{\perp} = |ReB_z|$ and the longitudinal momentum is $|p_z| = (1/2\pi)|\lambda_z eB_z|$, where λ_z is the wavelength of the trajectory. Both of these calculations depend on the dimensions of the detector and the value of the magnetic field. The dependencies can be lessened by scaling the reconstructed momentum using a known calibration point. The only distinctive feature of the Michel momentum spectrum is the end point, the kinematically allowed maximum momentum, $|\vec{p}_{\max}| = 52.83$ MeV/c. The calibration is complicated by the fact that the reconstructed track yields an average momentum over the length of the trajectory in the presence of energy loss. Energy loss in a planar detector is inversely proportional to the cosine of

the track relative to the orientation of the planes. In addition, energy loss varies with the decay vertex depth in the stopping target. A non-centered stopping distribution will yield different energy loss calibration parameters upstream and downstream. The momentum calibration is a fit of β , α_{up} and α_{dn} using

$$E_{\text{up}}^{\text{Reconstructed}} = (1 + \beta) \left[E^{\text{max}} - \frac{\alpha_{\text{up}}}{|\cos \theta|} \right] \quad (4.9)$$

and

$$E_{\text{dn}}^{\text{Reconstructed}} = (1 + \beta) \left[E^{\text{max}} - \frac{\alpha_{\text{dn}}}{|\cos \theta|} \right] \quad (4.10)$$

where $E^{\text{Reconstructed}}$ is the endpoint of the spectrum for a given $\cos \theta$ and E^{max} is the kinematically allowed maximum energy. β is a correction to the overall momentum and α_{up} and α_{dn} are energy loss corrections. Figure 36 shows momentum spectra near the endpoint for surface and cloud muon decays from data and Monte Carlo with forward and backward decays shown separately. Graphically, the difference between the data and Monte Carlo edge positions shows the momentum scale difference that is addressed by the momentum calibration. Differences in the shape are due to momentum resolution differences between data and Monte Carlo.

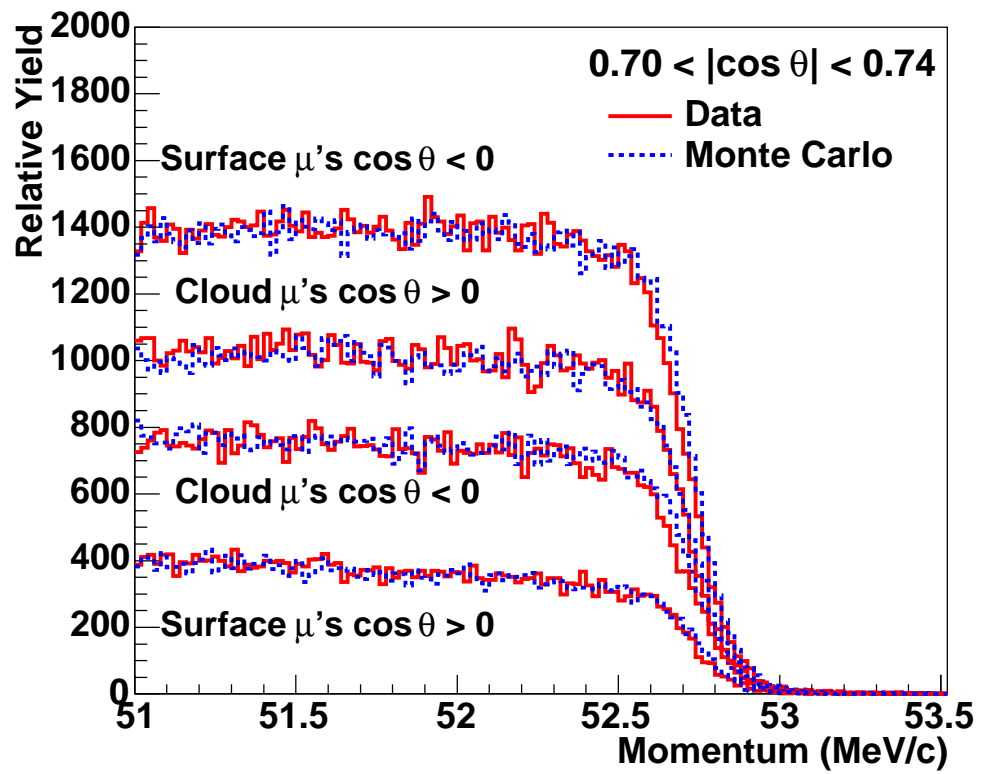


Fig. 36. Momentum endpoint spectra. Spectra are used for momentum calibration. Plots are from uncalibrated data and Monte Carlo sets.

CHAPTER V

EVALUATION OF SYSTEMATIC UNCERTAINTIES

The fitting of Michel parameters relies on a fit of a data-produced spectrum to a sum of simulation-produced spectra, as described in Sec. A. Systematic effects can arise with this approach in two ways. One, there are ways in which the simulation output and data are treated differently. Two, the Monte Carlo does not perfectly simulate the experiment. As for the first type, the TWIST analysis is blind to whether the input is from simulation or data with a few exceptions, timing calibrations (t_o 's), alignments and electronic cross talk removal. For the second type, all possible sources of error imagined were considered. These include a variety of sources that can be grouped into eight categories:

- track selection algorithm,
- chamber response,
- stopping target thickness,
- positron interactions,
- spectrometer alignment,
- momentum calibration,
- theoretical radiative corrections
- and muon beam stability.

The calculation of each systematic uncertainty is presented in the following sections. One particular strategy was employed extensively and warrants special attention.

To summarize, the approach measures the effect on the Michel parameters of an exaggerated source of error and scales by the exaggeration factor. This involves 6 steps.

1. Modify the data taking conditions such that a possible source of error is significantly larger than under standard conditions.
2. Take a complete systematic set under the modified conditions (See Sec. C).
3. Fully analyze the systematic set, producing a decay positron spectrum in momentum and $\cos\theta$.
4. Determine $\Delta\rho$ from a fit of the spectrum from the systematic set to a sum of a spectrum from a data set plus derivative spectra as described in Sec. A.
5. Determine the exaggeration factor, the size of the modified source of error relative to the source of error in the standard set.
6. Divide $\Delta\rho$ by the exaggeration factor to yield the systematic uncertainty.

Alternatively, this strategy can be employed by modifying a source of error in a Monte Carlo set and extracting $\Delta\rho$ from a fit to the standard Monte Carlo produced spectrum plus derivative spectra. 5 such Monte Carlo systematic sets were generated:

1. 30 μm Graphite,
2. B Misalignment,
3. Dead Zone,
4. Density Change
5. and Bulged Foils

These sets are described in the discussions of the relevant systematic uncertainties.

A. Uncertainties in Fits of Correlated Data

In some cases, sources of error can be exaggerated by modifying the analysis of a data or Monte Carlo set. Then it is possible to fit the results of a modified analysis to the results of a standard analysis of the same set. Such a fit between correlated data removes the large uncertainty due to statistics. To properly estimate the uncertainty in a fit of correlated data the σ 's are scaled by a factor of $\sqrt{\chi_{\text{unscaled}}^2/\text{Degrees of freedom}}$.

B. Track Selection Algorithm

Section E describes the two algorithms used in selecting between multiple reconstructed tracks. As noted, these algorithms produced differences in their results.

In the sections that follow, the quantization of most effects is dependent on the algorithm used. In these cases the effects were measured with each algorithm and are reported for algorithms \mathbb{A} and \mathbb{B} separately, denoted $\sigma_{\mathbb{A}}$ and $\sigma_{\mathbb{B}}$. In addition, the two algorithms produce a difference in the value of ρ . Half of this difference is interpreted as a systematic uncertainty due to the track selection algorithm yielding $\sigma = 0.00022/2 = 0.00011$.

C. Positron Interactions

The category labeled “positron interactions” includes four effects:

1. momentum resolution,
2. multiple scattering,
3. hard interactions,
4. and material outside the detector.

Each of these effects concerns positron interactions that are independent of the type of data taken and thus these systematic uncertainties are common to all data sets.

1. Momentum Resolution

The uncertainty in the momentum resolution is dominated by the uncertainty in the transverse momentum. The resolution from Monte Carlo can be made to match data by introducing a 50 KeV/c smearing to the transverse momentum. The uncertainty associated with the resolution difference was calculated by introducing a 200 KeV/c smearing to the transverse momentum in an analysis of a Monte Carlo set. The resulting decay positron spectrum was fit to the spectrum from the standard analysis of the same Monte Carlo set. The systematic uncertainties were found to be $\sigma_{\text{A}} = -0.00002/4 = -0.00001$ and $\sigma_{\text{B}} = -0.00010/4 = -0.00003$.

2. Multiple Scattering

To study the effect of multiple scattering, $\cos\theta$ was artificially smeared in an analysis of a standard Monte Carlo set. The smearing took the form $k/(|\vec{p}|\sqrt{\cos\theta})$. The resulting decay positron spectrum was fit to the unsmeared spectrum from the same Monte Carlo set. The inaccuracy in the Monte Carlo simulation of multiple scattering is $O(1.5\text{mrad})$ as reported in Sec. C. k was chosen so that a typical 30 MeV/c momentum track at 45° had a $\Delta\theta = 30$ mrad. The systematic uncertainties are $\sigma_{\text{A}} = -0.00226/20 = -0.00011$ and $\sigma_{\text{B}} = -0.00446/20 = -0.00022$.

3. Hard Interactions

The calculation of hard interaction effects requires determination of

- the discrepancy between Monte Carlo and data,

- the effect of hard interactions on the yield as a function of momentum and
- the corresponding effect on yield as a function of momentum due to a change in ρ .

In the study described in Sec. C the hard interaction rates were estimated by considering the ratio of counts in the tail of the distribution to total counts. It was found that the rate in Monte Carlo differed from the rate in data by 14% including effects from target thickness uncertainty and the simulation of hard interactions.

The effects of hard interactions on the yield were determined by a Monte Carlo study. A plot was made of yield as a function of reconstructed momentum for particles losing < 1 MeV/c momentum in the detector. A similar plot was made for particles losing > 1 MeV/c momentum in the detector. Additionally, a plot was made of yield as a function of momentum at the time of decay. Ratios of the histograms, reconstructed ($d|\vec{p}| < 1$ MeV/c)/initial and reconstructed ($d|\vec{p}| > 1$ MeV/c)/initial are shown for $0.5 < |\cos \theta| < 0.7$ and $0.7 < |\cos \theta| < 0.84$ in Fig. 37. From the plots, the fractional change due to intermediate ($d|\vec{p}| < 1$ MeV/c) and hard ($d|\vec{p}| > 1$ MeV/c) interactions were calculated over the range [30, 50] MeV/c. The fractional change due to intermediate interactions is 0.0030 and due to hard interactions is 0.0037.

The systematic uncertainty is determined by scaling the fractional change in yield by the inaccuracy of the Monte Carlo simulation of hard interactions and multiplying by the conversion factor, $d\rho/d(\text{yield})$. ($d\rho/d(\text{yield}) = 0.68$, for the range [30, 50] MeV/c.) Applying this method yields: $\sigma = [0.0030 \times 0.05 + 0.037 \times 0.14] \times 0.68 = 0.00045$.

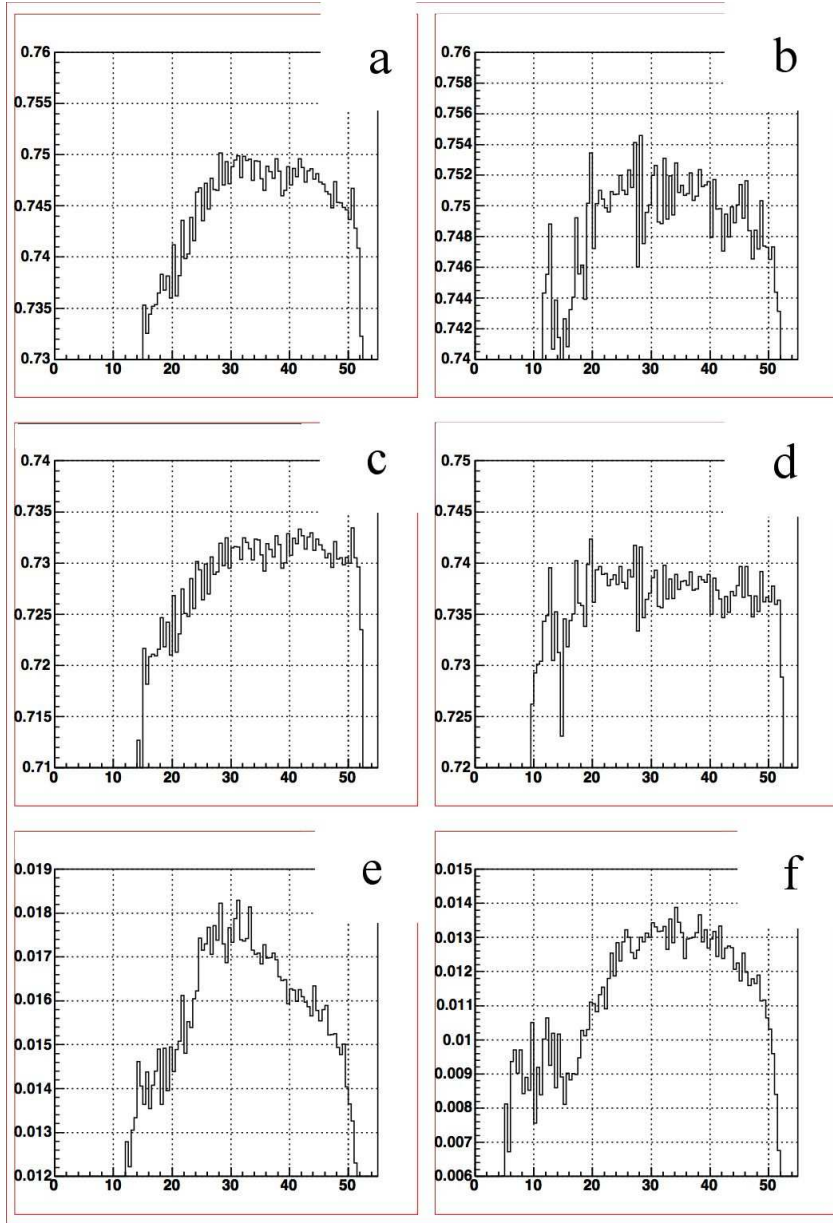


Fig. 37. Ratios of momentum histograms. Histograms are ratios of reconstructed/thrown vs. momentum (MeV/c). Left column (panels a, c and e) is for $0.5 < |\cos \theta| < 0.7$. Right column (b, d and f) is for $0.7 < |\cos \theta| < 0.84$. Top row (a and b) - all decay positrons. Middle row (c and d) - positrons losing less than 1 MeV/c of momentum in the detector. Bottom row (e and f) - positrons losing greater than 1 MeV/c of momentum in the detector. All plots taken from an analysis using algorithm A .

4. Stopping Target Thickness

As noted in Sec. 2 the stopping target was coated on each side with a $10\ \mu\text{m}$ layer of graphite. The uncertainty in the graphite thickness was ${}^{+10}_{-5}\ \mu\text{m}$. The thickness of the layer effects the amount of energy loss the decay positron experiences prior to entering the drift chambers. The systematic effect due to this uncertainty was determined by creating a Monte Carlo set generated with graphite layers of $30\ \mu\text{m}$ on each side of the stopping target. The resulting decay spectrum was fit to a spectrum created with the nominal $10\ \mu\text{m}$ layers of graphite. The effect on ρ is scaled by 2, the factor by which the thickness was modified relative to the uncertainty. The study yields $\sigma_{\text{A}} = 0.00049$ and $\sigma_{\text{B}} = 0.00051$.

5. Material Outside Detector

Materials outside of the tracking volume provided sources of background particles. In particular, components of the beam package were a source of decay particles, deltas and backscattered positrons. The systematic due to such extra particles was calculated by introducing additional material downstream of the detector. The resulting spectrum was fit to a spectrum generated without the extra material. For the test a $0.65\ \text{cm}$ thick aluminum plate was mounted on a $0.59\ \text{cm}$ thick plastic plate $80\ \text{cm}$ downstream of the central stopping target. A full data set was taken with this arrangement. The resulting decay positron spectrum was fit to a spectrum from Nominal B. Monte Carlo simulations of the additional downstream material produced a spectrum that was fit to a spectrum from a nominal Monte Carlo set. The comparison of the two fits yields the difference in ρ due to inaccuracies in the Monte Carlo.

The effect is scaled by the ratio of extra particles due to the aluminum divided

by the difference between data and Monte Carlo in nominal conditions.

$$\text{Exaggeration factor} = \frac{\text{Extra (Aluminum)}}{|\text{Extra (Data)} - \text{Extra (Monte Carlo)}|} = 60 \quad (5.1)$$

The systematic uncertainties are $\sigma_{\text{A}} = 0.00054/60 = 0.00001$ and $\sigma_{\text{B}} = 0.00023/60 < 0.00001$.

D. Chamber Response

Chamber response systematics include:

- DC efficiencies,
- MWPC efficiencies,
- dead zone,
- simulation of drift times near cell boundaries,
- DC high voltage variations,
- temperature and pressure variations,
- cathode foil shape,
- electronic cross talk
- and t_o variations.

1. DC Efficiencies

The efficiencies of the DC's were set to 100% in the Monte Carlo for the sets used in Michel parameter fits. The actual DC efficiencies were $> 99.9\%$. To test the systematic uncertainty due to DC inefficiencies, random wire inefficiencies of 5%

were introduced into an analysis of Nominal B. For each hit wire a random number generator determined if the wire was inefficient. The resulting decision was considered valid for the following 700 ns, insuring that all hits on that wire from that particle adhered to the efficiency decision. The random inefficiency was again calculated for any hits on the same wire more than 700 ns after the previous calculation. All hits that occurred on a so called inefficient wire for the said time interval were removed from the data prior to any analysis. The spectrum from the analysis with the 5% DC wire inefficiencies was fit to a spectrum from a standard analysis of Nominal B. The systematic uncertainties due to not simulating DC inefficiencies are $\sigma_{\text{A}} = 0.00064/50 = 0.00001$ and $\sigma_{\text{B}} = 0.00001/50 < 0.00001$.

2. MWPC Efficiencies

MWPC inefficiencies were tested in the same manner as those for the DC's listed above, with the exception that efficiencies/inefficiencies were valid for only 80 ns in keeping with the drift times of the MWPC's. The results yield systematic uncertainties of $\sigma_{\text{A}} = -0.00010/50 < 0.00001$ and $\sigma_{\text{B}} = -0.00017/50 < 0.00001$.

3. Dead Zone

Muons coming to rest in the detector leave sufficient ionization in a cell to render a region of the cell inefficient for a period of time. Such a region is referred to as a dead zone. A study looking for expected positron hits along wires previously hit by a muon showed that a muon dead zone is typically 0.5 cm in length along the wire and lasts for 3 μs . A Monte Carlo set was generated with dead zone of 5 cm in length that resulted in more than 4 times the usual loss of hits. The resulting decay positron spectrum was fit to the nominal spectrum. Scaling by the relative rates of lost hits, 4, yields systematic uncertainties of $\sigma_{\text{A}} = 0.00054/4 = 0.00014$ and

$$\sigma_{\text{B}} = 0.00016/4 = 0.00004.$$

4. Simulation of Drift Times Near Cell Boundaries

The GARFIELD drift time simulations described in Sec. 1 are less accurate for hits near the cell boundaries. The associated systematic effect was investigated by removing these hits from the analysis. In a Monte Carlo set, all hits with drift times greater than 400 ns were removed from an analysis and the resulting spectrum was fit to a standard analysis of the same Monte Carlo set. Since the long drift times are not simulated accurately an equivalent time cut for data is not necessarily 400 ns. The corresponding time cut for data was determined by investigating the relationship between time cut and number of degrees of freedom in the track fit as illustrated by Fig. 38. Based on the study, all hits with drift times greater than 522 ns were removed from an analysis of Nominal B. The resulting spectrum was fit to a spectrum from a standard analysis of the same data set. The difference between $\Delta\rho$ for the Monte Carlo fit and $\Delta\rho$ for the data fit yields systematic uncertainties of $\sigma_{\text{A}} = 0.00048$ and $\sigma_{\text{B}} = 0.00040$.

5. DC High Voltage Variations

The DC high voltages could vary up to 5 V from their nominal setting of 1950 V. High voltage variations affect the drift time vs. distance relationships within the cell and possibly the signal collection efficiency. The efficiency is accounted for separately. The effect due to changes in the drift time vs. distance relationships are measured by analyzing Nominal B using relationships generated by a GARFIELD simulation with a DC high voltage of 1850 V. The resulting decay positron spectrum is fit to the spectrum from the standard analysis of Nominal B. The systematic uncertainties are found to be $\sigma_{\text{A}} = -0.00070/20 = -0.00004$ and $\sigma_{\text{B}} = -0.00012/20 = -0.00001$.

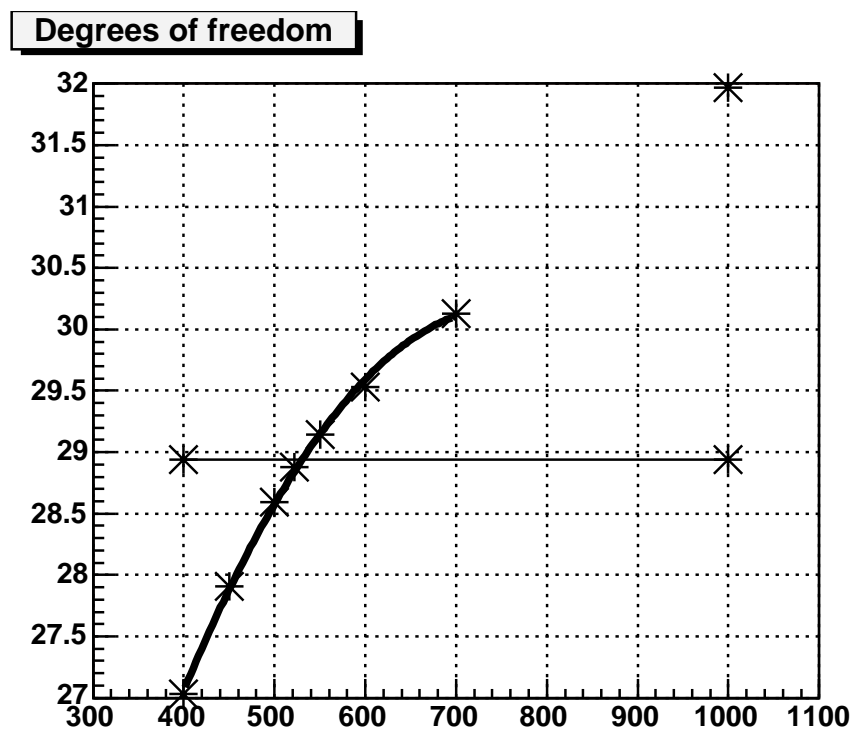


Fig. 38. Number of degrees of freedom vs. drift time cut (ns) for data. Horizontal reference line shows the number of degrees of freedom for Monte Carlo with a 400 ns drift time cut.

6. Density Variations

Density variations can effect the spectrum in two ways. First, a change in density leads to a change in the muon stopping location. This effect is calculated separately under the category, Muon Beam Stability. Second, density affects the drift times within the drift cells. To study this effect, the density of the cells were modified in simulations by changing the temperature in the GARFIELD drift time calculations from the nominal 300 K to 270 K. This resulted in a difference in density from the nominal 20 times as large as the biggest difference in the Low Field set and 10 times the biggest difference in each of the other sets. A full Monte Carlo set was generated with this modified condition and the resulting decay positron spectrum was fit to the nominal Monte Carlo produced spectrum. To avoid double counting, the effect due to a change in the stopping location was subtracted from the net effect. The resulting systematic uncertainties for the Low Field set are $\sigma_{\text{A}} = -0.00003$ and $\sigma_{\text{B}} = -0.00015$. The systematic uncertainties for each of the other sets are $\sigma_{\text{A}} = -0.00005$ and $\sigma_{\text{B}} = -0.00029$.

7. Cathode Foil Bulges

Pressure differentials within the detector caused displacement of the cathode foils separating chambers from the helium volume. The foils are held in position along their circumference so that the foils “bulged” creating a larger or smaller cell width near the axis of the detector while retaining nominal widths near the circumference. The change in cell dimensions modifies the drift distance verses time relationship. A Monte Carlo set was generated with 500 μm bulges on the appropriate cathode foils. The simulation used drift distance vs. time relationships produced by a GARFIELD simulation of the modified cells. The resulting decay positron spectrum was fit to

the standard Monte Carlo produced spectrum yielding $\sigma_{\mathbb{A}} = -0.00005$ and $\sigma_{\mathbb{B}} = -0.00010$. The foil bulging was monitored during data taking and was observed to vary between data sets. The systematic uncertainties taking account of the degree of bulging for each data set are shown in Table XIII.

Table XIII. Systematic uncertainties due to foil bulging.

	Nominal A	Nominal B	Low Field	High Field	Cloud
$\sigma_{\mathbb{A}}$	-0.00002	-0.00001	-0.00002	-0.00001	-0.00001
$\sigma_{\mathbb{B}}$	-0.00005	-0.00003	-0.00005	-0.00003	-0.00003

8. Cross Talk

A significant difference between data and Monte Carlo analysis is in regards to electronic cross talk. As the TWIST Monte Carlo did not simulate cross talk, the cross talk removal code was not run on Monte Carlo sets. The effect due to the combination of cross talk in data and subsequent removal of hits labeled as cross talk was evaluated by analyzing Nominal B without cross talk hits removed. The resulting spectrum was fit to the spectrum from the standard analysis of Nominal B. MOFIA routines removed at least 90% of the electronic cross talk hits successfully. The systematic uncertainties were found to be $\sigma_{\mathbb{A}} = 0.00025/10 = 0.00002$ and $\sigma_{\mathbb{B}} = 0.00016/10 = 0.00002$.

9. t_o Variations

The timing offsets due to electronics (t_o calibrations) were calculated at the beginning and end of the fall 2002 run. The difference between the initial t_o and final t_o was less than a few ns for each channel. To study this, a t_o calibration file was created by

adding 10 times the difference in t_o 's to the initial t_o for each channel. An analysis of Nominal B using this t_o calibration file produced a decay positron spectrum that was fit to the standard spectrum from Nominal B. The systematic uncertainties were found to be $\sigma_{\text{A}} = 0.00023/10 = 0.00002$ and $\sigma_{\text{B}} = 0.00038/10 = 0.00004$.

E. Momentum Calibration

The momentum calibration includes effects from the end point fits and magnetic field reproductions.

1. End Point Fits

The systematic effect due to inaccuracies in the energy calibration was determined by varying each of the fit parameters independently and fitting the resulting decay positron spectra to the spectrum generated with an unaltered energy calibration. The fits for given offsets yield $d\rho/d\beta$, $d\rho/d\alpha_{up}$ and $d\rho/d\alpha_{dn}$. The combined effect is calculated by evaluating the expression $A^T V A$ where $A^T = (d\rho/d\beta \ d\rho/d\alpha_{up} \ d\rho/d\alpha_{dn})$ and V is the 3×3 covariance matrix from the energy calibration fit. The effect is calculated independently for data and Monte Carlo and the result is added in quadrature. The resulting systematic uncertainty is $\sigma = 0.00015$.

2. Magnetic Field Reproduction

Inaccuracies in the magnetic field map lead to inaccuracies in the determination of the decay positron momentum. To quantize this effect, a modified magnetic field map was produced by distorting the standard field simulation. The distortion took the form $\Delta B_z = -(0.006 \text{ G/cm}^2)z^2 - (0.00004 \text{ G/cm}^3)z^3 - (1.25 \text{ G/cm})r$. Nominal B was analyzed using this distorted field map. The resulting decay positron spectrum was

Table XIV. Systematic uncertainties due to magnetic field simulation.

	1.96 T	2.00 T	2.04 T
σ_{A}	-0.00015	0.00006	0.00029
σ_{B}	-0.00006	0.00002	0.00012

fit to the standard analysis of Nominal B. The size of the actual effect is a function of the size of the distortion and the accuracy of the three field maps described in Sec. C. The distorted field map differs from the 2 T field map by up to 40 G at the extremes of the tracking volume. The resulting systematic uncertainties for each field are shown in Table XIV.

F. Muon Beam Stability

There are three effects classified under muon beam stability,

1. stopping location,
2. beam intensity
3. and channel magnets.

1. Stopping Location

The analysis cuts events for which muons are known to stop outside of the stopping target. However, some muons stopping in the gas of the MWPC just upstream of the target (MWPC6) pass the cuts. Positrons from these muons miss the target if decaying upstream and experience energy loss through the entire target if decaying downstream. To determine the impact of this effect the spectrum from the Slightly Upstream systematic set was fit to a spectrum from Nominal A. The exaggeration

factor for this test can be found by exploiting the relationship between energy loss and the stopping position. From Sec. F $\Lambda = (\alpha_{up} - \alpha_{dn}) / (\alpha_{up} + \alpha_{dn})$ is a measure of the asymmetry in the longitudinal stopping position. Defining

$$\begin{aligned}\bar{\Lambda} &\equiv \frac{1}{5} \sum_{\text{Data Sets}} \Lambda, \\ V_{\Lambda} &\equiv \max(\Lambda) - \min(\Lambda) \text{ and} \\ \Delta\Lambda_{\text{Slightly Upstream}} &\equiv \bar{\Lambda} - \Lambda_{\text{Slightly Upstream}}\end{aligned}$$

one can express the exaggeration factor as

$$\frac{\Delta\Lambda_{\text{Slightly Upstream}}}{V_{\Lambda}} = 6.$$

This leads to systematic uncertainties of $\sigma_{\mathbb{A}} = 0.00017/6 = 0.00003$ and $\sigma_{\mathbb{B}} = 0.00094/6 = 0.00016$.

2. Beam Intensity

The effect due to beam intensity variation was determined by fitting a spectrum produced by an analysis of the Low Rate set (1.2 kHz trigger rate) to a spectrum from the High Rate set (5 kHz trigger rate). The difference in trigger rates between these two sets was 6 times the variation in a single data set, yielding $\sigma_{\mathbb{A}} = 0.00016/6 = 0.00003$ for algorithm \mathbb{A} . The systematic uncertainty for algorithm \mathbb{B} is negligible ($\sigma_{\mathbb{B}} < 0.00001/6$).

3. Channel Magnets

Small variations in the settings of the M13 magnets during the run affected the beam steering through the last two quadrupoles and into the TWIST detector. The effect on ρ was determined by analyzing the B2 + 10 G set and fitting the resulting spectrum to the spectrum from the Nominal A set. The 10 G offset in B2 was 50

times the largest variation in B2 for the data sets resulting in systematic uncertainties of $\sigma_{\mathbb{A}} = 0.00084/50 = 0.00002$ and $\sigma_{\mathbb{B}} = 0.00086/50 = 0.00002$.

G. Spectrometer Alignment

Spectrometer alignment includes positioning in three dimensions and position relative to the magnetic field. Alignments were calculated at both the beginning and end of the fall 2002 run and found to be stable within errors. Thus alignment systematic uncertainties are common to all data sets.

1. Translational

The translational alignment systematic effect was investigated by analyzing Nominal B with an alignment file containing random translational offsets 28 times the $5 \mu\text{m}$ precision of the translational alignment corrections. The resulting spectrum fitting yields $\sigma_{\mathbb{A}} = 0.00007/28 < 0.00001$ and $\sigma_{\mathbb{B}} = 0.00030/28 = 0.00001$.

2. Rotational

The rotational alignment systematic was found by analyzing Nominal B with an alignment file containing random rotational offsets 10 times the 0.01° precision of the rotational alignment corrections. The systematic uncertainties were found to be $\sigma_{\mathbb{A}} = -0.00056/10 = -0.00006$ and $\sigma_{\mathbb{B}} = 0.00111/10 = 0.00011$.

3. Longitudinal

The longitudinal alignment systematic was determined by introducing random offsets in the position of the drift chambers. The variation used is 10 times the $30 \mu\text{m}$ precision of the physical measurements of the detector stack made during and after

construction. The random offsets are introduced to the analysis of a standard Monte Carlo set. The resulting spectrum is fit to a spectrum generated without any position offsets. The systematic uncertainties are $\sigma_{\text{A}} = 0.00044/10 = 0.00004$ and $\sigma_{\text{B}} = 0.00101/10 = 0.00010$.

4. Magnetic Field Relative to Axis

A Monte Carlo set was generated with the magnetic field rotated relative to the axis of the detector by 0.25° . An offset of 0.25° is 7.2 times the uncertainty in the magnetic field alignment. The decay positron spectrum produced by analyzing this set was fit to the standard Monte Carlo produced spectrum yielding systematic uncertainties of $\sigma_{\text{A}} = -0.00149/7.2 = -0.00021$ and $\sigma_{\text{B}} = -0.00156/7.2 = -0.00022$.

H. Theoretical Radiative Corrections

The systematic uncertainty due to theoretical radiative corrections has been calculated for TWIST by Arbuzov and found to be $\sigma = 0.00020$ [11, 12, 13].

I. Summary of Systematic Uncertainties

A summary of systematic uncertainties is given in Table XV. Average values are given for the set dependent uncertainties. Effects that vary in time lead to systematic uncertainties that are set dependent, as is the case for chamber response, momentum calibration and beam stability.

Table XV. Systematic uncertainties summary. Weighted averages are given for set dependent uncertainties.

Effect	Uncertainty	
	Algorithm A	Algorithm B
Chamber response (ave)	± 0.00051	± 0.00048
Stopping target thickness	± 0.00049	± 0.00052
Positron interactions	± 0.00046	± 0.00047
Spectrometer alignments	± 0.00022	± 0.00026
Momentum calibration (ave)	± 0.00020	± 0.00016
Theoretical radiative corrections	± 0.00020	± 0.00020
Muon beam stability (ave)	± 0.00004	± 0.00016

CHAPTER VI

EXTRACTION OF MICHEL PARAMETERS

A. Fiducials

Fiducial cuts have been chosen to include a significant range in momentum and $\cos \theta$ while avoiding known reconstruction limitations. Cuts were chosen prior to the fitting of Michel parameters. The cuts were selected to be conservative rather than optimal. Fiducial cuts are graphically illustrated in Fig. 39. The yield before and after fiducial cuts are shown for the two angular ranges, $0.7 < |\cos \theta| < 0.84$ and $0.5 < |\cos \theta| < 0.7$, in Figs. 40 and 41, respectively.

1. $|\cos \theta| > 0.5$

Decay positrons with $|\cos \theta| < 0.5$ were excluded from the fits. High angle tracks produce signals on many wires in each plane and have significant transverse displacements between adjacent orthogonal planes. The initial track estimates depend critically on the transverse position determined from pairs of adjacent planes and thus the reconstruction efficiency is lower for high angle tracks. The influence of positron energy loss and multiple scattering is also increased for high angle tracks.

2. $|\cos \theta| < 0.84$

Decay positrons with $|\cos \theta| > 0.84$ were excluded from the fits. Small angle tracks include tracks with small radii. Reconstruction efficiency decreases as the transverse dimensions of the track approach the size of the uncertainty in the hit position for the initial track estimation. In addition, the momentum calibration procedure revealed structure in the momentum distribution for $|\cos \theta| > 0.9$.

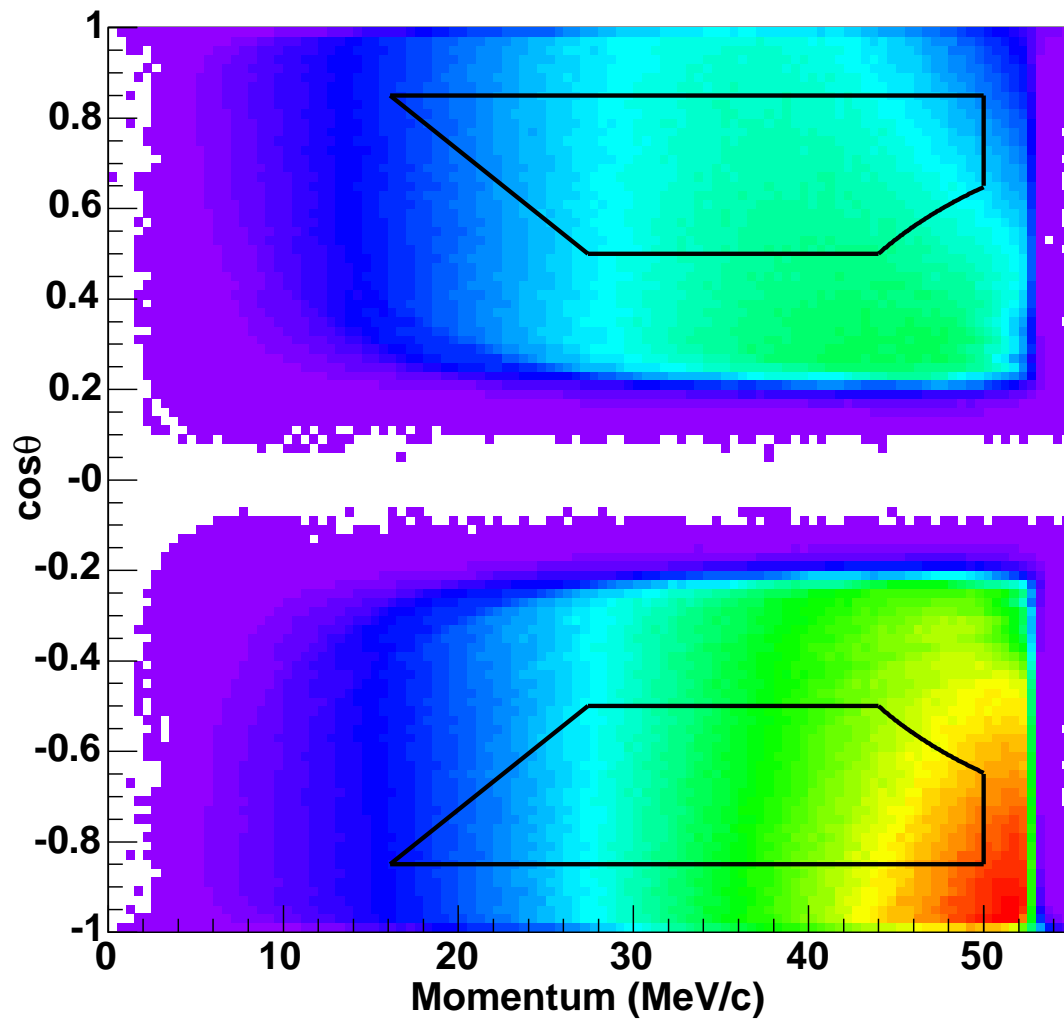


Fig. 39. Fiducial cuts. $0.5 < |\cos \theta| < 0.84$, $|p_z| > 13.7$ MeV/c, $p_\perp < 38.5$ MeV/c and $|\vec{p}| < 50$ MeV/c.

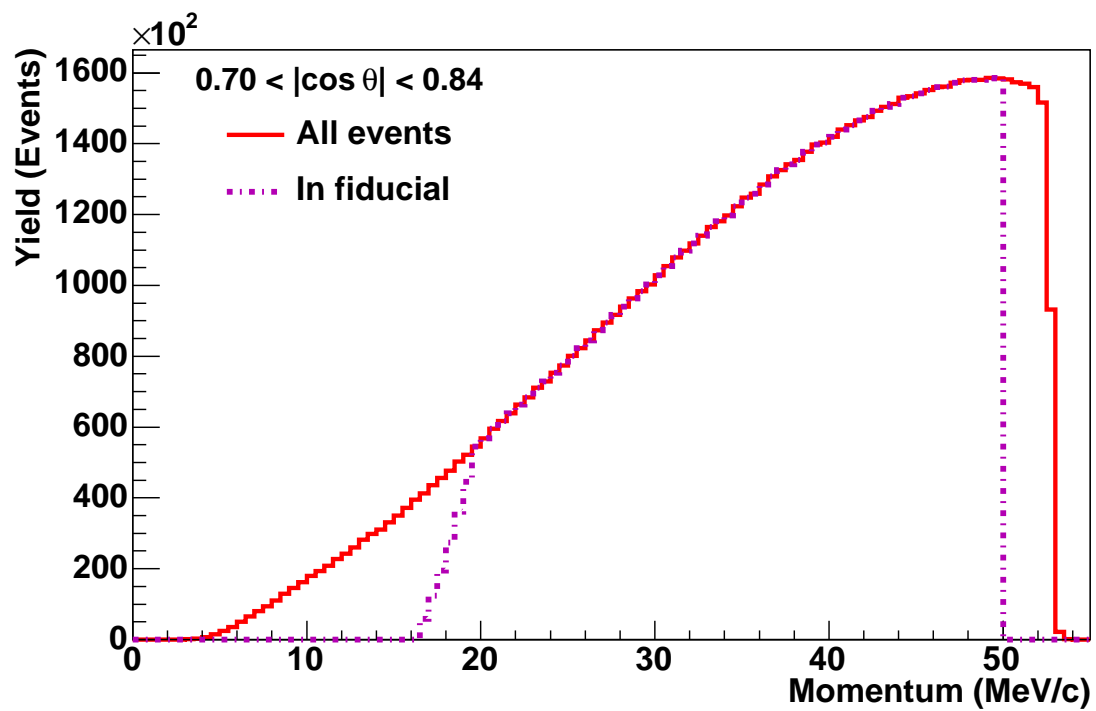


Fig. 40. Yield for fiducial cuts within $0.7 < |\cos \theta| < 0.84$. Yield as a function of momentum with and without fiducial cuts.

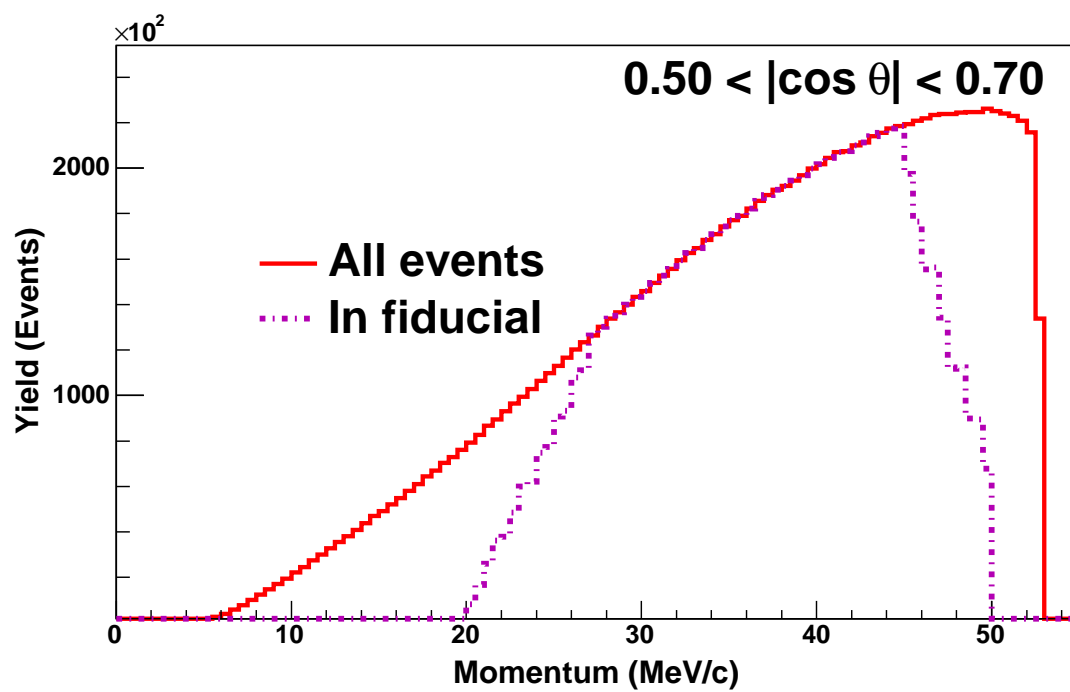


Fig. 41. Yield for fiducial cuts within $0.5 < |\cos \theta| < 0.7$. Yield as a function of momentum with and without fiducial cuts.

$$3. \quad |\vec{p}| < 50 \text{ MeV}/c$$

Decay positrons with momentum greater than 50 MeV/c were excluded from the fits. The spectrum edge is used for the energy calibration. The region is avoided to ensure that the energy calibration is independent of Michel parameter fits.

$$4. \quad p_{\perp} < 38.5 \text{ MeV}/c$$

Decay positrons with transverse momentum greater than 38.5 MeV/c were excluded from the fits. A positron track originating near the edge of the beam spot with a large radius can intersect the support structures for the DC's and MWPC's outside of the active tracking region. Including such tracks could introduce an angle dependent difference between data and Monte Carlo due to differences in the muon beam.

$$5. \quad |p_z| > 13.7 \text{ MeV}/c$$

Decay positrons with momentum less than 13.7 MeV/c were excluded from the fits. Positrons with longitudinal momentum ~ 12 MeV/c produced a series of hits in the sparse stack of DC's that projected onto two positions in the $u - v$ plane. The dense stack DC's broke the ambiguity, but without the degree of over determination and hence without the accuracy of higher momentum track reconstruction. Such an event is shown in Fig. 42

6. Sensitivity to Fiducial Cuts

It is important that the Michel parameter fits do not depend strongly on the limits of the fitting region near the fiducial cuts. The sensitivity to the fiducial cuts has been evaluated by a series of fits in which a single fiducial limit is slightly adjusted. It has been found that the fits are consistent within errors for each of the tested limits.

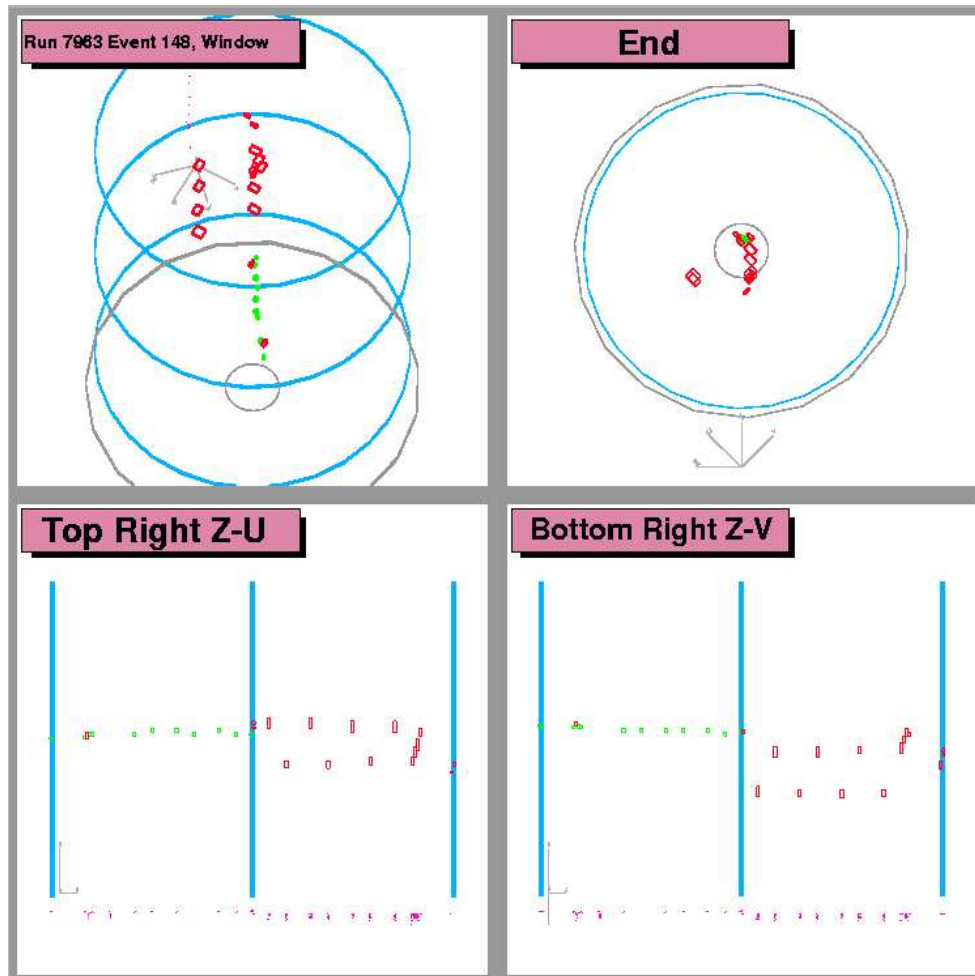


Fig. 42. Detector-track wavelength match. Various views of a downstream decay event from Nominal A in which the decay positron wavelength matches the sparse stack wavelength. The decay positron hits (red and to the right on the Z-U and Z-V projections) from the sparse stack project on to two points in the uv -plane resulting in an undetermined circle. The ambiguity is broken by hits in the dense stack.

Results of the fiducial cuts tests are shown in Fig. 43.

B. Quality of Analysis Results

1. Michel Parameter Fits

The Michel parameter fits were verified by generating a Monte Carlo set using ρ , $P_\mu\xi$ and $P_\mu\xi\delta$ as determined in the fit of the Nominal B produced spectrum. η was set to the PDG value for this verification set. A fit of the spectrum from Nominal B to the spectrum from the verification set should yield Michel parameter offsets consistent with 0 if the fits are valid. The fit verification could not be performed while blind to the Michel parameter values. However, the procedure was sufficiently detailed while blind so that no decisions were necessary during the verification procedure. The fit verification yielded offsets consistent with 0 for each Michel parameter, $\Delta\rho = 0.00025 \pm 0.00066$, $\Delta\xi = -0.00016 \pm 0.0016$ and $\Delta\delta = 0.0004 \pm 0.0013$.

2. Fit Residuals

The fit quality is further exhibited by the fit residuals. Fig. 44 shows the normalized fit residuals as a function of momentum for the data sets and the verification. The plots reveal no obvious momentum dependence across the sets. The complementary plots for normalized fit residuals vs. $\cos\theta$ are shown in Fig. 45

In addition, a study was performed comparing the reconstructed momentum spectrum to the true spectrum for two angular ranges. For the study, events within the fiducial were divided between decays with $0.7 < |\cos\theta| < 0.84$ and decays with $0.5 < |\cos\theta| < 0.7$. For each range, a probability of reconstruction was calculated by creating a bin by bin ratio within the fiducial region of a reconstructed Monte Carlo spectrum divided by the true Monte Carlo spectrum. This represents the overall

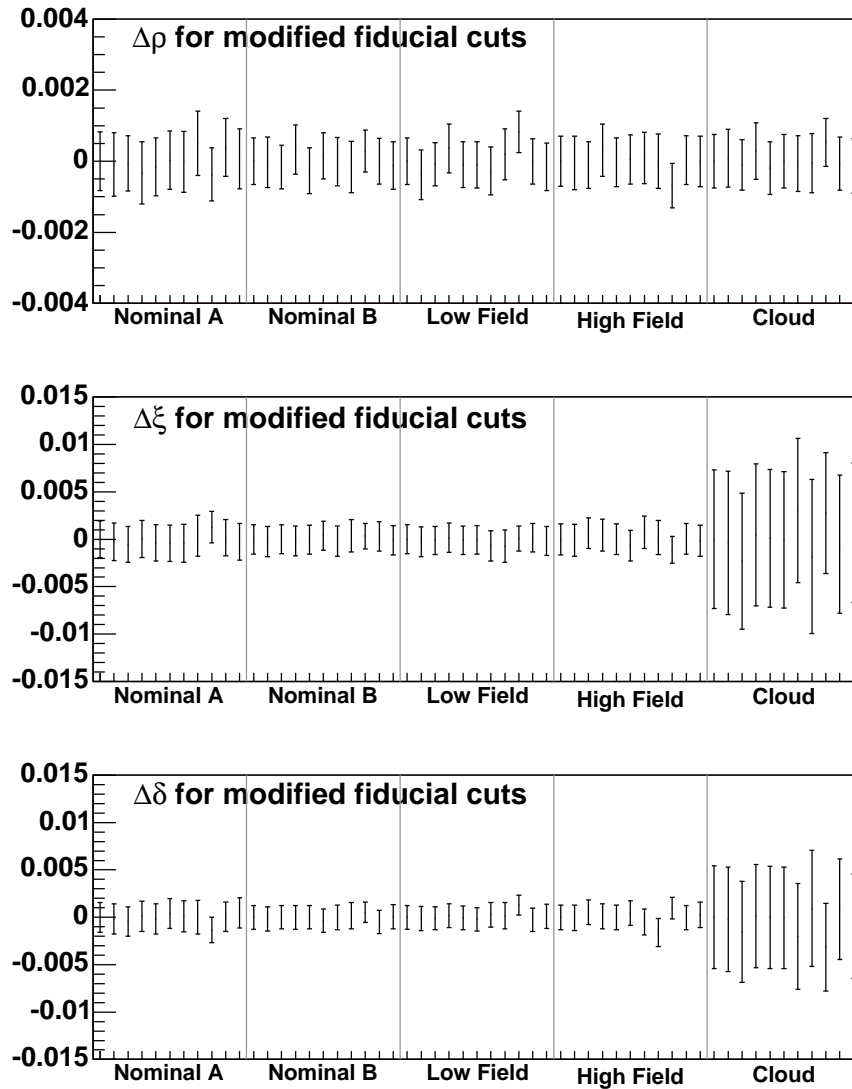


Fig. 43. Michel parameter fit sensitivity to fiducial cuts. Differences in Michel parameters for modifications to fiducial cuts, $\rho_{\text{variation}} - \rho_{\text{standard}}$. Bin ordering for each data set is: 1 - Standard fiducial cuts; 2 - $|\vec{p}| < 49$ MeV/c. 3 - $|\vec{p}| < 51$ MeV/c. 4 - $p_{\perp} < 36.9$ MeV/c. 5 - $p_{\perp} < 39.3$ MeV/c. 6 - $p_z > 13.2$ MeV/c. 7 - $p_z > 14.2$ MeV/c. 8 - $|\cos\theta| > 0.45$. 9 - $|\cos\theta| > 0.55$. 10 - $|\cos\theta| < 0.80$. 11 - $|\cos\theta| < 0.90$.

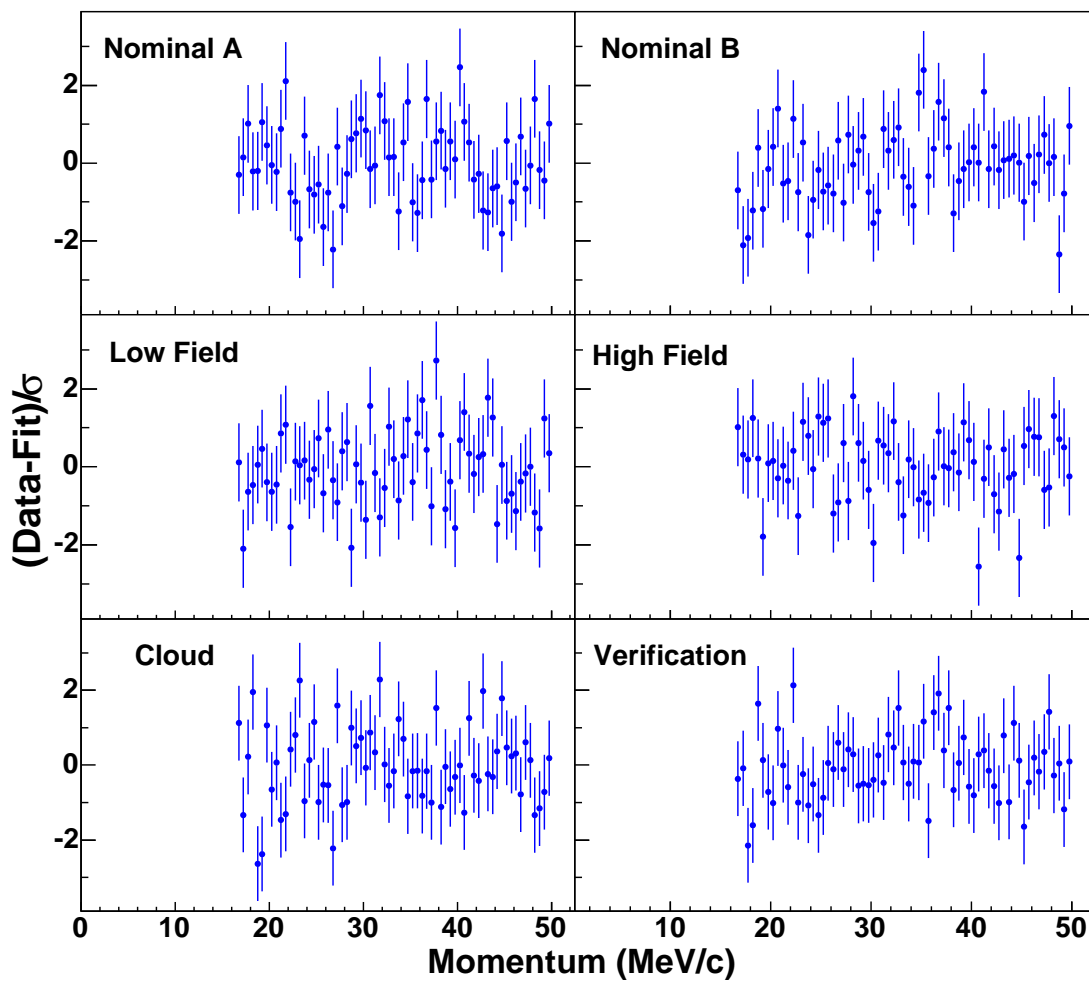


Fig. 44. Michel parameter fit residuals vs. momentum. Normalized fit residuals from the Michel parameter fits vs. momentum for each of the data sets and the verification set.

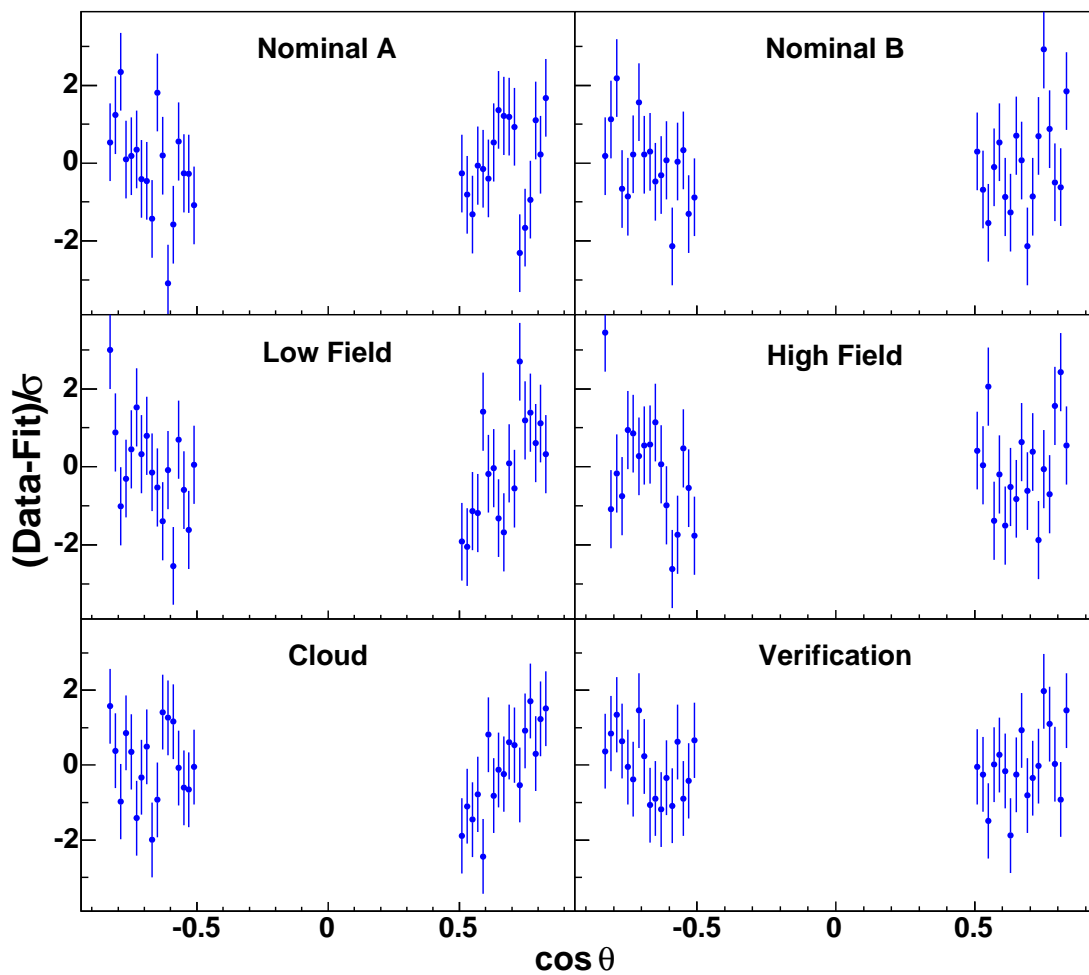


Fig. 45. Michel parameter fit residuals vs. $\cos \theta$. Normalized fit residuals from the Michel parameter fits vs. $\cos \theta$ for each of the data sets and the verification set.

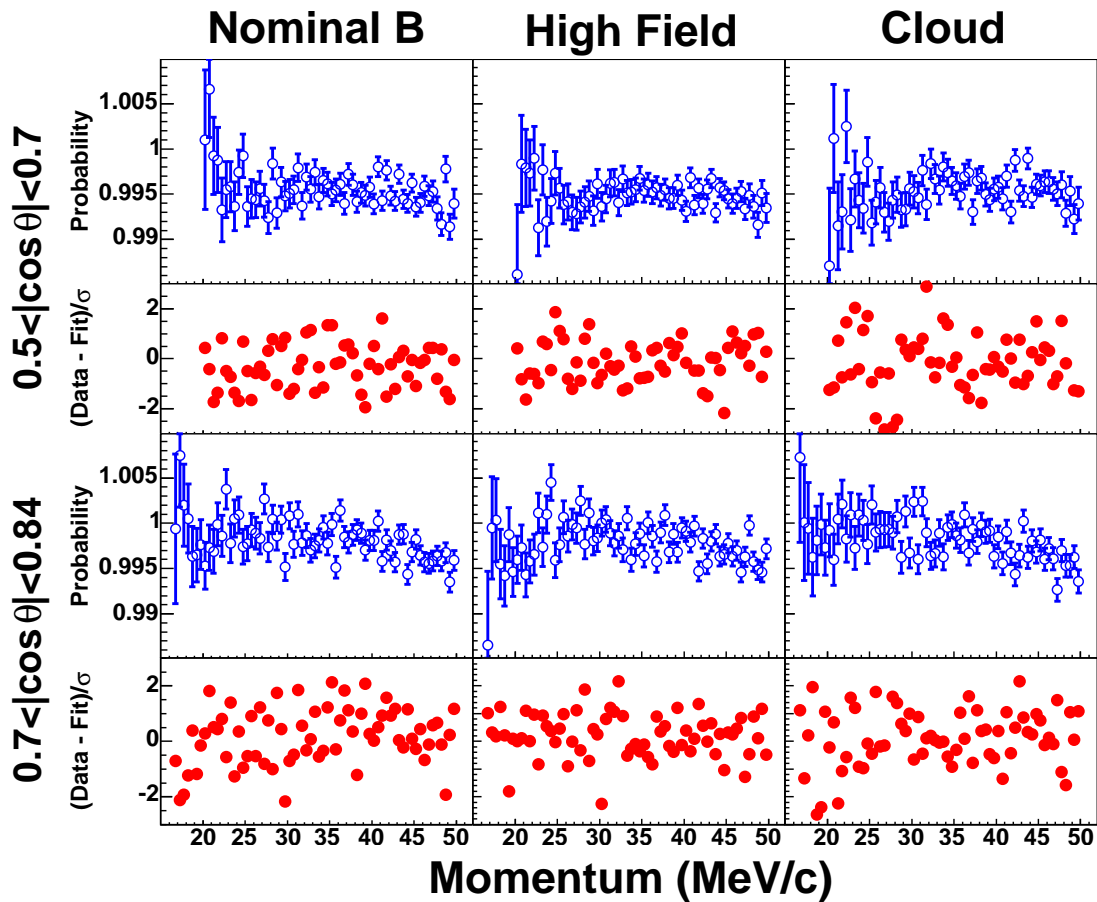


Fig. 46. Reconstruction probability and normalized residuals. Probabilities are bin by bin ratios within the fiducial region of reconstructed momentum over true momentum for the Monte Carlo set corresponding to the given data set.

response function of the TWIST spectrometer for the muon decay spectrum. Fig. 46 shows the resulting high probabilities along with the normalized residuals for each angular range for the Nominal B, High Field and Cloud sets.

C. $d\rho/d\eta$

A simultaneous fit of ρ , η , $P_\mu\xi$ and $P_\mu\xi\delta$ for each of the data sets reveals significant correlations between some of the parameters as shown in Table XVI.

Table XVI. Correlation coefficients for 3 and 4 parameter fits. Correlations are significantly reduced and precision on ρ increased when η is held fixed.

Four parameter fit (ρ , η , $P_\mu\xi$ and $P_\mu\xi\delta$)						
Data set	Correlation with ρ			$\frac{\chi^2}{ndof}$	Error on ρ	Error on η
	η	$P_\mu\xi$	$P_\mu\xi\delta$			
Nominal A	0.944	0.725	0.777	$\frac{1813}{1886}$	0.0025	0.132
Nominal B	0.945	0.726	0.782	$\frac{1959}{1886}$	0.0020	0.106
Low Field	0.945	0.729	0.781	$\frac{1949}{1886}$	0.0020	0.105
High Field	0.944	0.723	0.778	$\frac{1802}{1886}$	0.0021	0.111
Cloud	0.945	0.241	0.272	$\frac{1992}{1886}$	0.0023	0.121
Three parameter fit (ρ , $P_\mu\xi$ and $P_\mu\xi\delta$)						
Data set	Correlation with ρ			$\frac{\chi^2}{ndof}$	Error on ρ	Error on η
	η	$P_\mu\xi$	$P_\mu\xi\delta$			
Nominal A	$\equiv 0.0$	0.159	0.258	$\frac{1814}{1887}$	0.0008	η Fixed
Nominal B	$\equiv 0.0$	0.160	0.258	$\frac{1965}{1887}$	0.0007	η Fixed
Low Field	$\equiv 0.0$	0.159	0.256	$\frac{1951}{1887}$	0.0007	η Fixed
High Field	$\equiv 0.0$	0.160	0.259	$\frac{1804}{1887}$	0.0007	η Fixed
Cloud	$\equiv 0.0$	0.034	0.058	$\frac{1993}{1887}$	0.0008	η Fixed

Table XVII. Correlation coefficients for 1 and 2 parameter fits. Coefficients show improvement in precision on ρ when η is held fixed.

Two parameter fit (ρ and η)				
Data set	Correlation with ρ η	$\frac{\chi^2}{ndof}$	Error on ρ	Error on η
Nominal A	0.945	$\frac{64}{65}$	0.0026	0.134
Nominal B	0.946	$\frac{55}{65}$	0.0021	0.108
Low Field	0.946	$\frac{60}{65}$	0.0020	0.107
High Field	0.944	$\frac{53}{65}$	0.0022	0.113
Cloud	0.945	$\frac{76}{65}$	0.0023	0.121
One parameter fit (ρ)				
Data set	Correlation with ρ η	$\frac{\chi^2}{ndof}$	Error on ρ	Error on η
Nominal A	$\equiv 0.0$	$\frac{65}{66}$	0.0008	η Fixed
Nominal B	$\equiv 0.0$	$\frac{60}{66}$	0.0007	η Fixed
Low Field	$\equiv 0.0$	$\frac{62}{66}$	0.0007	η Fixed
High Field	$\equiv 0.0$	$\frac{55}{66}$	0.0007	η Fixed
Cloud	$\equiv 0.0$	$\frac{77}{66}$	0.0008	η Fixed

Note from the table that the error on η is significantly larger than 0.013, the error quoted by the PDG [2]. Furthermore, the correlations between ρ and $P_\mu\xi$ and $P_\mu\xi\delta$ decrease from 0.7 – 0.8 to < 0.3 when fixing η . One can also reduce the correlations between η and $P_\mu\xi$ and $P_\mu\xi\delta$ by fixing ρ because the correlation with $P_\mu\xi$ is with a combination of ρ and η , rather than either individually. Because of the strong correlation between ρ and η , fixing η improves the precision on ρ . Similarly, fits of the Michel angle integrated spectrum (independent of $P_\mu\xi$ and $P_\mu\xi\delta$) yield improved precision on ρ when η is fixed as shown in Table XVII. However, the fits introduce an uncertainty due to the imprecise knowledge of η that is not included in the fitter error. To calculate this error, η was fixed to a series of values spanning $\pm 5\sigma$ from the world average. The results of these fits shown in Table XVIII show that $d\rho/d\eta = 0.0180$ over this entire range. Taking this result in combination with the precision on η (± 0.013) yields a contribution to the error on ρ of ± 0.00023 .

D. Single Fit Parameter Fits of Angle Integrated Spectra

Fits of ρ using the angle integrated spectra were performed as a consistency check. The fits are consistent with the three parameter fits using the spectra in $|\vec{p}^\dagger|$ and $\cos\theta$.

E. ρ

The fits of ρ are given in Table XIX for each of the data sets for each algorithm. Combining the data yields $\rho = 0.75091 \pm 0.00032(\text{stat})$ with $\chi^2/\text{Degree of freedom} = 7.5/4$ for algorithm \mathbb{A} and $\rho = 0.75069 \pm 0.00032(\text{stat})$ with $\chi^2/\text{Degree of freedom} = 9.9/4$ for algorithm \mathbb{B} . The uncertainties are scaled to account for the χ^2 yielding an additional uncertainty of ± 0.00030 for algorithm \mathbb{A} and ± 0.00036 for algorithm \mathbb{B} . Taking the average value from algorithms \mathbb{A} and \mathbb{B} yields the TWIST value of

Table XVIII. $d\rho/d\eta$. $d\rho/d\eta = 0.0180$ across $\pm 5\sigma_\eta$ as shown from a series of fits using data set Nominal B.

Fixed η	$\Delta\rho = \rho(\eta_{\text{Fixed}}) - \rho(\eta_{\text{PDG}})$	$\frac{d\rho}{d\eta}$
$\eta_{\text{PDG}} - 5\sigma_\eta$	-0.001167	0.01795
$\eta_{\text{PDG}} - 4\sigma_\eta$	-0.000934	0.01796
$\eta_{\text{PDG}} - 3\sigma_\eta$	-0.000700	0.01795
$\eta_{\text{PDG}} - 2\sigma_\eta$	-0.000467	0.01796
$\eta_{\text{PDG}} - 1\sigma_\eta$	-0.000233	0.01792
$\eta_{\text{PDG}} + 1\sigma_\eta$	0.000233	0.01792
$\eta_{\text{PDG}} + 2\sigma_\eta$	0.000467	0.01796
$\eta_{\text{PDG}} + 3\sigma_\eta$	0.000700	0.01795
$\eta_{\text{PDG}} + 4\sigma_\eta$	0.000934	0.01796
$\eta_{\text{PDG}} + 5\sigma_\eta$	0.001167	0.01795

Table XIX. ρ by data set. Uncertainties include statistical and set dependent uncertainties. Each fit has 1887 degrees of freedom.

Data Set	Algorithm A		Algorithm B	
	ρ	χ^2	ρ	χ^2
Nominal A	0.75134 ± 0.00083	1814	0.74916 ± 0.00066	1809
Nominal B	0.74937 ± 0.00066	1965	0.75124 ± 0.00083	1973
Low Field	0.75027 ± 0.00065	1951	0.74985 ± 0.00065	1943
High Field	0.75248 ± 0.00070	1804	0.75256 ± 0.00070	1806
Cloud	0.75157 ± 0.00076	1993	0.75107 ± 0.00076	1973

$\rho = 0.75080 \pm 0.00032(\text{stat}) \pm 0.00097(\text{syst}) \pm 0.00023$ where the final uncertainty is due to the precision on η as discussed in Sec. C.

F. Other Michel Parameters

1. Distortion of the Asymmetry

While still blind to the Monte Carlo input Michel parameters an error was discovered in the production of the simulated decay spectrum. The symptom was a polarization dependency in the fit of $\Delta\delta$ and was traced to an error in the angle dependent radiative corrections. The error produced a distortion in the asymmetry of the Michel spectrum, but had no effect on angle integrated spectrum. Furthermore, the muons exhibited a time dependent depolarization in the graphite coated Mylar stopping target. The Monte Carlo simulation has not been adjusted to fully account for the depolarizing effect of the stopping target. This leads to additional significant systematic effects for $P_\mu\xi$ that are not fully known. As a consequence, the values of $P_\mu\xi$ and δ from the

Table XX. $P_\mu\xi$ by data set. Only statistical uncertainties are given. Each fit has 1887 degrees of freedom.

Data Set	Algorithm A		Algorithm B	
	$P_\mu\xi$	χ^2	$P_\mu\xi$	χ^2
Nominal A	0.9834 ± 0.0019	1814	0.9858 ± 0.0019	1809
Nominal B	0.9919 ± 0.0015	1965	0.9943 ± 0.0015	1973
Low Field	0.9801 ± 0.0015	1951	0.9824 ± 0.0015	1943
High Field	1.0001 ± 0.0016	1804	1.0025 ± 0.0016	1806
Cloud	1.0839 ± 0.0073	1993	1.0724 ± 0.0073	1973

fits reported here are not considered reliable. The results are given in Tables XX and XXI without systematic uncertainties.

2. δ

The fit of δ with the appropriate radiative corrections yields $\delta = 0.74964 \pm 0.00066(\text{stat}) \pm 0.00112(\text{syst})$ as reported in [42]. The fit for δ also found a value of ρ consistent with the value reported here.

Table XXI. δ by data set. Only statistical uncertainties are given. Each fit has 1887 degrees of freedom.

Data Set	Algorithm A		Algorithm B	
	δ	χ^2	δ	χ^2
Nominal A	0.75423 ± 0.00160	1814	0.75284 ± 0.00158	1809
Nominal B	0.75018 ± 0.00126	1965	0.74891 ± 0.00124	1973
Low Field	0.75072 ± 0.00126	1951	0.74908 ± 0.00124	1943
High Field	0.74817 ± 0.00133	1804	0.74737 ± 0.00131	1806
Cloud	0.75446 ± 0.00539	1993	0.76054 ± 0.00542	1973

CHAPTER VII

CONCLUSIONS

A. $P_\mu\xi$

The TWIST values for ρ and δ and the value for $P_\mu\xi\delta/\rho$ from [40] can be used with Eq. 1.13 to set new limits on $P_\mu\xi$. The new 90% confidence interval is $0.9960 < P_\mu\xi \leq \xi < 1.0040$ an improvement over the previous measurements, $P_\mu\xi = 1.0027 \pm 0.0079 \pm 0.0030$ from pion decay [38] and $P_\mu\xi = 1.0013 \pm 0.0030 \pm 0.0053$ from kaon decay [39]. Furthermore, these results yield $Q_R^\mu < 0.00184$, $|g_{LR}^S| < 0.086$, $|g_{LR}^V| < 0.043$ and $|g_{LR}^T| < 0.025$, all at the 90% confidence level.

B. Implications for Left-right Symmetric Models

The TWIST measurements yield improvements on the mixing angle, ζ , and the mass of the right-handed W boson, M_{W_R} , in left-right symmetric models. The TWIST value of ρ leads to a 90% confidence limit on ζ of $|\zeta| < 0.030$ improving over the previous limit of $|\zeta| < 0.047$.

The TWIST lower limit on $P_\mu\xi$ can be used with

$$\xi = 1 - 2\epsilon^2 - 2\zeta^2 \quad (7.1)$$

$$P_\mu = 1 - 2(\epsilon + \zeta)^2 \quad [V_{ud}^R \sim V_{ud}^L] \quad (7.2)$$

$$P_\mu = 1 - 2\zeta^2 \quad [V_{ud}^R \text{small}] \quad (7.3)$$

from [40] to set an improved 90% confidence limit of $M_{W_R} > 420 \text{ GeV}/c^2$ in pseudo-manifest left-right symmetric models and $M_{W_R}g_L/g_R > 380 \text{ GeV}/c^2$ in non-manifest left-right symmetric models where g_L and g_R are the coupling constants [20]. An updated exclusion plot for ζ and M_{W_R} is shown in Fig. 47.

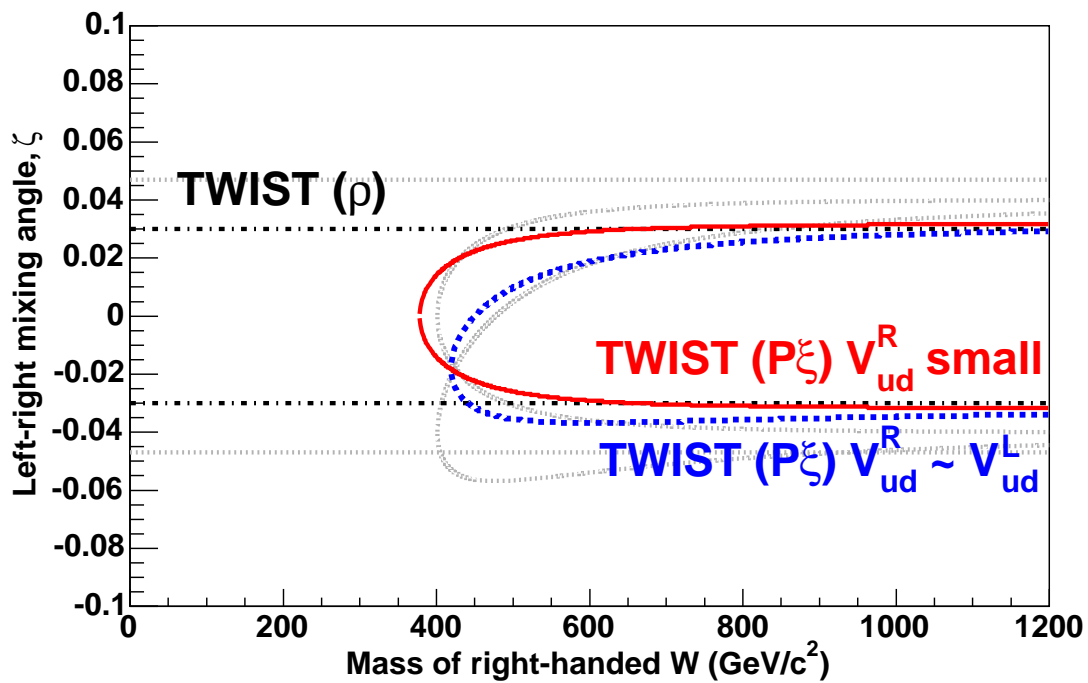


Fig. 47. Updated left-right symmetric model exclusion plot. 90% confidence level exclusion plot for left-right symmetric model parameters; mass of the right-handed W and mixing angle, ζ . Previous limits shown in gray on this figure are explicitly labeled in Fig. 5.

C. Future Measurements

Analysis is currently under way to complete a measurement of $P_\mu\xi$ with a precision of a few parts in 10^3 . A second measurement of ρ and δ with precisions of parts in 10^4 is also under way. The ultimate goal of TWIST is to measure ρ and δ with a precision of a few parts in 10^4 and $P_\mu\xi$ with a precision of parts in 10^4 .

D. Summary

The TWIST measurement of $\rho = 0.75080 \pm 0.00032(\text{stat}) \pm 0.00097(\text{syst}) \pm 0.00023$ is an improvement on the world average leading to improved limits of left-right symmetric model parameters. Future TWIST measurements should continue to improve these limits over the next few years.

REFERENCES

- [1] F. Halzen and A.D. Martin, *Quarks & Leptons: An Introductory Course in Modern Particle Physics* (John Wiley & Sons, Inc., New York ,1984).
- [2] K. Hagiwara *et al.*, Phys. Rev. **D66**, 010001 (2002).
- [3] S. Eidelman *et al.*, Phys. Lett. **B592**, 1 (2004).
- [4] W. Fetscher, H.-J. Gerber, and K.F. Johnson, Phys. Lett. **B173**, 102 (1986).
- [5] K. Mursula, M. Roos, and F. Scheck, Nucl. Phys. **B219**, 321 (1983).
- [6] L. Michel, Proc. Phys. Soc. **A63**, 514 (1950).
- [7] C. Bouchiat and L. Michel, Phys. Rev. **106**, 170 (1957).
- [8] T. Kinoshita and A. Sirlin, Phys. Rev. **107**, 593 (1957).
- [9] T. Kinoshita and A. Sirlin, Phys. Rev. **108**, 844 (1957).
- [10] T. Kinoshita and A. Sirlin, Phys. Rev. **113**, 1652 (1959).
- [11] A. Arbuzov, A. Czarnecki, and A. Gaponenko, Phys. Rev. **D65**, 113006 (2002).
- [12] A. Arbuzov and K. Melnikov, Phys. Rev. **D66**, 093003 (2002).
- [13] A. Arbuzov, JHEP **0303**, 063 (2003).
- [14] W. Fetscher and H.-J. Gerber, *Precision Measurements in Muon and Tau Decays*, in *Precision Tests of the Standard Electroweak Model* (World Scientific, Singapore, 1995).
- [15] J.C. Pati and A. Salam, Phys. Rev. Lett. **31**, 661 (1973).

- [16] R.N. Mohapatra and J.C. Pati, Phys. Rev. **D11**, 2558 (1975).
- [17] S. Abachi *et al.*, Phys. Rev. Lett. **76**, 3271 (1996).
- [18] T. Affolder *et al.*, Phys. Rev. Lett. **90**, 081802 (2003).
- [19] J.C. Hardy and I.S. Towner, Phys. Rev. Lett. **94**, 092502 (2005).
- [20] P. Herczeg, Phys. Rev. **D34**, 3449 (1986).
- [21] P. Langacker and S.U. Sandar, Phys. Rev. **D40**, 1569 (1989).
- [22] M.V. Chizhov, hep-ph/0405073.
- [23] M.V. Chizhov, hep-ph/0402105.
- [24] E. Frlež *et al.*, Phys. Rev. Lett. **93**, 181804 (2004).
- [25] Y. Fukuda *et al.*, Phys. Rev. Lett. **81**, 1562 (1998).
- [26] Q.R. Ahmad *et al.*, Phys. Rev. Lett. **87**, 071301 (2001).
- [27] Q.R. Ahmad *et al.*, Phys. Rev. Lett. **89**, 011301 (2002).
- [28] G. Prézeau *et al.*, hep-ph/0409193.
- [29] J. Peoples, Columbia University, thesis, Nevis Report No. 147 1966 (unpublished).
- [30] B.A. Sherwood, Phys. Rev. **156**, 1475 (1967).
- [31] D. Fryberger, Phys. Rev. **166**, 1379 (1968).
- [32] S.E. Derenzo, Phys. Rev. **181**, 1854 (1969).
- [33] F. Liu, Texas A&M University, thesis, 1994 (unpublished).

- [34] M.J. Yang, Nucl. Instrum. Meth. **A270**, 126 (1988).
- [35] H. Burkard *et al.*, Phys. Lett. **160B**, 343 (1985).
- [36] N. Danneburg *et al.*, Phys. Rev. Lett. **94**, 021802 (2005).
- [37] B. Balke *et al.*, Phys. Rev. **D37**, 587 (1988).
- [38] I. Beltrami *et al.*, Phys. Lett. **B194**, 326 (1987).
- [39] J. Imazato *et al.*, Phys. Rev. Lett. **69**, 877 (1992).
- [40] A. Jodidio *et al.*, Phys. Rev. **D34**, 1967 (1986); **37**, 237E (1988).
- [41] R.S. Henderson *et al.*, hep-ex/0409066.
- [42] A. Gaponenko *et al.*, Phys. Rev. **D71**, 071101 (2005).

VITA

James Raymond Musser received his Bachelor of Science degree in Mathematics from West Texas State University in 1987. He received a Texas Secondary Teaching Certification from Texas Christian University in 1992. Mr. Musser's research interests lie in experimental tests of the Standard Model of particle physics and searches for physical phenomena beyond the Standard Model.

Mr. Musser may be reached at Arkansas Tech University, Department of Physical Sciences, 1701 North Boulder Avenue, Russellville, AR 72801-2222.